
Development of Techniques for Single Dendritic Spine Analysis: Spinomics

Thorben Andreas Kurz



München 2012

Development of Techniques for Single Dendritic Spine Analysis: Spinomics

Thorben Andreas Kurz

Dissertation
an der Fakultät für Biologie
der Ludwig-Maximilians-Universität
München

vorgelegt von
Thorben Andreas Kurz
aus Bonn Bad-Godesberg

München, 31.07.12

Erstgutachter: Prof. Dr. Alexander Borst

Zweitgutachter: PD Dr. Martin Heß

Tag der mündlichen Prüfung: 26.09.2012

Table of Contents

Summary	10
Chapter 1 Introduction	12
1.1 Dendritic Spines	13
1.1.1 Historic Discovery of Dendritic Spines	13
1.1.2 Spine Morphology and its Impact on Function.....	14
1.2 Light Microscopy	17
1.2.1 Techniques and Limitations	17
1.2.2 Spine Morphology in Light Microscopy	19
1.3 Electron Microscopy	21
1.3.1 Serial Section Transmission Electron Microscopy	21
1.3.2 Spine Morphology in the Electron Microscope	22
1.3.3 Scanning Electron Microscopy	24
1.3.4 Serial Section Block-face Scanning Electron Microscopy (SBFSEM)	27
1.4 Segmentation of Large Electron Microscopic Datasets.....	30
1.5 Aim of this Thesis	32
Chapter 2 Materials and Methods.....	33
2.1 Methods.....	33
2.1.1 Tissue Preparation	33
2.1.2 Electron Microscopy	38
2.1.3 Evaluation of the Osmium Tetroxide + Lead Citrate Staining Protocol.....	41
2.1.4 NeuroStruct.....	42
2.1.5 Spine Pruning	51
2.1.6 Spine Density	52
2.2 Material.....	53
2.2.1 Buffers.....	53
2.2.2 Chemicals	53
2.2.3 Light microscopy	55
2.2.4 Electron microscopy	56
Chapter 3 Results	57
3.1 Development of a Staining Protocol for Single Biocytin-filled Neurons for SBFSEM	57
3.1.1 The Selection of usable Cells for SBFSEM in Light Microscopy	58
3.1.2 Screening for a Proper Staining in the SBFSEM	61
3.1.3 Evaluation of the Staining Protocol	74

3.2 Validation of NeuroStruct	89
3.2.1 Datasets used for the Validation	90
3.2.2 Validation Results	95
3.3 Application of the Staining Protocol and NeuroStruct	100
3.3.1 Reconstruction of an entire L5B Neuron	100
3.3.2 Spinomics	110
Chapter 4 Discussion.....	112
Summary	112
4.1 Development of a Specific Staining Protocol for Biocytin-filled Neurons.....	113
4.1.1 Imaging issues	113
4.1.2 Staining issues.....	114
4.2 Expansion and Validation of NeuroStruct.....	116
4.2.1 The RV-Connectivity-Filter	116
4.2.2 Original SBFSEM Dataset	117
4.2.3 Manual Tracings.....	117
4.2.4 True Objects: How “true“ are Computational and Manual Reconstructions?.....	118
4.2.5 Conclusions	119
4.2.6 Comparison to other Segmentation Approaches	120
4.3 Large Scale Reconstruction and Spinomics.....	122
4.3.1 Acquisition of SBFSEM Data.....	122
4.3.2 The Reconstruction of GLT-L5B Neuron: TK100909A1.....	123
4.3.3 Spine Density Analysis of TK100909A1.....	124
4.3.4 Spinomics and Outlook	126
Chapter 5 References.....	128
Acknowledgements.....	140
Curriculum vitae.....	141

List of Figures

Figure 1.1: Schematic Drawing of a Synapse	14
Figure 1.2: Fluorescence Microscopy Systems	18
Figure 1.3: Spine Classification using Confocal and STED Microscopy.....	20
Figure 1.4: ssTEM.....	21
Figure 1.5: Spines in TEM.....	24

Figure 1.6: SEM, Signal Creation and Backscattering Coefficient.....	25
Figure 1.7: ESEM	28
Figure 1.8: SBFSEM.	29
Figure 1.9: Segmentation Artifacts in Previous Studies.....	31
Figure 2.1: Patching, DAB Staining, EM Contrasting and Mounting.....	34
Figure 2.2: Trimmed Sample.....	39
Figure 2.3: Approaching the Sample.....	39
Figure 2.4: "old" NeuroStruct Pipeline	42
Figure 2.5: Preprocessing.....	43
Figure 2.6: "new" NeuroStruct Pipeline.....	44
Figure 2.7: Segmentation.....	45
Figure 2.8: The R-V Connectivity Filter	48
Figure 2.9: Validation Metrics.....	50
Figure 2.10: Spine Pruning Expansion in NeuroStruct.....	51
Figure 3.1: DAB Polymerisation and Osmium Tetroxid Binding	58
Figure 3.2: Fluorescence of Alexa 594.....	59
Figure 3.3: DAB Stained Cells	60
Figure 3.4: Staining Artifacts in the SBFSEM.....	62
Figure 3.5: Rough Smooth Surface	63
Figure 3.6: Staining Protocol using Osmium Tetroxide and Uranyl Acetate	64
Figure 3.7: Reconstruction of the Image Stack shown in Figure 3.6	65
Figure 3.8: Staining Protocol using only Osmium Tetroxide.....	67
Figure 3.9: Reconstruction of the Image Stack shown in Figure 3.8	68
Figure 3.10: Staining Protocol using Osmium Tetroxide and Lead Citrate.....	70
Figure 3.11: X-Y-Z- minimum Projection of the Image Stack from Figure 3.10.....	72
Figure 3.12: Reconstruction of the Image Stack shown in Figure 3.11.	72
Figure 3.13: Evaluation Parameters.....	74
Figure 3.14: Dataset TK020408E_st004_3.....	76
Figure 3.15: Dataset TK120509B_st004_3.....	77
Figure 3.16: Dataset TK100909A1_st011_3	78
Figure 3.17: Dataset TK190111A_st005_6	79
Figure 3.18: Dataset TK190111B_st001_6.....	80
Figure 3.19: Dataset TK120910F_st013_9	81
Figure 3.20: Dataset TK091110A_st003_10 (orange).....	82
Figure 3.21: Dataset TK091110B_st003_10 (yellow).....	83

Figure 3.22: Dataset TK091110F_st001_11 (yellow).....	84
Figure 3.23: Dataset TK091110G_st001_11 (orange).....	85
Figure 3.24: Cross Section of Non-Segmentable Dataset.....	86
Figure 3.25: Contrast Comparison in TEM, SEM, and SBFSEM.....	87
Figure 3.26: Datasets for the Evaluation of NeuroStruct.....	90
Figure 3.27: Comparison of the Manual and Reference Reconstructions.....	92
Figure 3.28: Comparison of the Computational Reconstructions.....	94
Figure 3.29: Ranking of the Manual and NeuroStruct Tracings.....	99
Figure 3.30: GLT-L5B Neuron TK100909A1.....	100
Figure 3.31: Minimum Z-Projections of TK100909A1_st001-st024.....	102
Figure 3.32: Minimum Z-Projections of TK100909A1_st025-st030.....	103
Figure 3.33: Minimum Z-Projections of TK100909A1_st031 and st037.....	104
Figure 3.34: Minimum Z-Projections of TK100909A1_st038+39 and st040+41.....	105
Figure 3.35: Missed Branches in L5B.....	107
Figure 3.36: Reconstruction of TK100909A1.....	108
Figure 3.37: Spine Distribution of the L5B (GLT) Neuron TK100909A1.....	109
Figure 3.38: Spinomics.....	110

List of Tables

Table 1.1: Spine properties from two independent studies.....	23
Table 3.1: Summary of the Protocol Evaluation.....	75
Table 3.2: Properties of the data stack TK100909A1_st011_3.....	91
Table 3.3: Robustness Results for Nst, NSt ⁻ , and NSt ⁺	93
Table 3.4: Quantitative Findings for the Reference Datasets.....	95
Table 3.5: Validation Results with respect to R1 at the Object Space.....	96
Table 3.6: Validation Results with respect to R2 at the Object Space.....	96
Table 3.7: Validation Results with respect to R1 at the Image Space.....	97
Table 3.8: Validation Results with respect to R2 at the Image Space.....	98
Table 3.9: Amount of Images and Physical Size in Z for every Stack of TK100909A1.....	106
Table 4.1: Effect of Major Scanning Parameters.....	113
Table 4.2: Comparison of Spine Distributions in Cortical Layers.....	125

Summary

Dendritic spines are very small protrusions on dendrites of excitatory neurons and function as their main input sites. They are commonly composed of a head of a few hundred nanometers in diameter and a thinner neck that can have a diameter of less than 50 nanometers. The investigation of morphologies of these small structures is performed with both light microscopy and electron microscopy. The light microscopy provides the possibility to quantitatively investigate spines but, due to the light diffraction limit, not in significant detail. Serial section electron microscopy provides high resolution but, due to laborious and error-proneness, lacks the feasibility to obtain quantitative morphologies. The Serial Block-face Scanning Electron Microscopy (SBFSEM) combines high resolution imaging with the possibility of quantitative and fully automated acquisition of electron microscopy images. Thereby it is possible to acquire large data sets at nanoscale resolution.

My thesis focuses on the acquisition, isolation, and analysis of quantitative single spine morphologies of previously identified and patch-clamped neurons. I used SBFSEM to obtain three dimensional image stacks at a voxel size of 25x25x30nm (xyz). To segment the morphological information from the acquired image stacks, I used a custom and highly parallelized software toolbox “NeuroStruct”, which is composed of several individual filters that are optimized to automatically segment and reconstruct single biocytin-filled neurons from large image stacks obtained from SBFSEM. The first reconstructions, however, showed additional structures of the surrounding neuropil due to unspecific staining. That is why I developed, established, and valued a new staining protocol that gives intense contrast to the previously filled neuron and only faint contrast to the neuropil. The staining protocol showed repeatedly good contrast for multiple individual neurons in SBFSEM image stacks. Next, I used SBFSEM to obtain image stacks of an entire Layer 5B neuron which has a bounding box of 409x230x608 μ m and a raw data size of 1.1 TB. I manually marked about 6600 dendritic spines on the neuron and computed their layer distribution.

After I obtained multiple data sets from SBFSEM, the necessity to validate and check for the NeuroStruct segmentation toolbox’s accuracy was required as I used it as a standard to

reconstruct my data sets. Hence, a 25.38 μm long dendritic stretch that contained 106 dendritic spines was used as the basis for validation. Reference tracings, derived from five independent manual tracings, were computed for the use of “ground truth”. The validation was carried out on the level of objects (spines) and pixels (volume). The results clearly demonstrate that NeuroStruct provides a reliable and high quality reconstruction, which matches and in some parameters even exceeds the quality of manual tracings.

Finally, the validated NeuroStruct pipeline was expanded with an iterative spine pruning algorithm, to allow the isolation of single spine morphologies for further analysis. Although this work is at the beginning and suffers from initial problems, the eventual aim is to be able to isolate tens of thousands of single spines and build up a dendritic spine database from which spines can be clustered and biophysically characterized according to their morphological features. This analysis will be called “Spinomics” and can bring together the quantitative light and high resolution electron microscopy approach.

Chapter 1 Introduction

The mammalian brain is the most sophisticated organ of its body. It is a complex of subdivisions from which the biggest compartment, the cerebral cortex, is composed of about 80 billion neurons interacting with each other via trillions of synapses in humans (Azevedo et al, 2009; Herculano-Houzel, 2009; Pelvig et al, 2008). These numbers make its unraveling very complex and arduous. To be able to learn about the wiring and interplay of this network, the rodent has been long since established as a model organism in science. Mouse species are frequently used as their nervous system consists of millions of neurons that do not only maintain a comparable architecture to humans but also reduce the complexity by an order of magnitude (Roth & Dicke, 2005; Schuz & Palm, 1989). The cortex itself is subdivided into smaller areas responsible for computing different emotional, cognitive, motor or sensory tasks, reflecting a functional localization (Passingham et al, 2002). As an example and field of work in this thesis, the somatosensory barrel cortex (BC) is composed of even smaller computational subunits, each responsible for computing signals received from one single whisker. These units are organized in columnar structures composed of about ten thousand neurons (Fox, 2008; Petersen, 2007; Woolsey & Van der Loos, 1970). In order to understand the underlying principles of networks like this, numerous strategies in morphology, behavior, physiology, and computational science are being performed (Celikel & Sakmann, 2007; Druckmann et al, 2011; Helmstaedter et al, 2007; Helmstaedter et al, 2009; Lang et al, 2011a; Markram, 2006; Oberlaender et al, 2009; Rushworth et al, 2011). The individual neurons within such a network receive input via synapses which are composed of a presynaptic (axon) and postsynaptic (dendrite) side. Most excitatory input to a dendrite is conducted through small protrusions called dendritic spines. These spines were discovered over 130 years ago by Santiago Ramón y Cajal and have been intensively investigated ever since.

1.1 Dendritic Spines

1.1.1 Historic Discovery of Dendritic Spines

In 1873 Camillo Golgi published the famous unspecific dendrite staining technique which is named after himself (Golgi, 1873). This staining, which is based on silver chromate precipitation in dendritic arbors, was learnt and used by Santiago Ramón y Cajal to investigate cell morphologies of the nervous system under the light microscope. Cajal observed that the surface of Purkinje cells in the cerebellum of birds "... appears bristling with points and short spines..." ("... aparece erizada de puntas o espinas cortas . . .") (Cajal, 1888). Although they had been previously observed by other scientists, Cajal was the first to describe these protrusions as neuronal structures, and this 15 years after the publication of the Golgi staining. Even Golgi himself observed structural protrusions but did not see their physiological importance. At the time, however, the consensus was that these structures were silver precipitates due to the Golgi staining. Because of this common tenor, Cajal's discovery caused a controversy in the scientific community between scientists who believed in the discovery of new neuronal elements (Berkley, 1895; Edinger, 1893; Monti, 1895a; Monti, 1895b; Retzius, 1891; Schaffer, 1892) and those who didn't (Dogiel, 1896; Meyer, 1895; Meyer, 1896; Meyer, 1897; von Kölliker, 1896). Eight years later he proved his theory right by using Methylene Blue staining to evidently demonstrate that spines are neuronal structures and not staining artifacts (Cajal, 1896a; Cajal, 1896b). Upon the identification of dendritic spines as neuronal structures, Cajal realized that some axons had free endings (Cajal, 1894). By this observation, he found the first piece of evidence for his fundamental "neuron doctrine", which describes connections between individual neurons in comparison to the diffuse nerve network syncytium that was proposed by Joseph von Gerlach in 1872 (Gerlach, 1872). Gerlach's theory was shared by many scientists, including Golgi, who even in his Nobel lecture, which he shared with Cajal in 1906 for "their work on the structure of the nervous system", contradicted the neuron doctrine (Golgi, 1906). Although Cajal's neuron doctrine became more and more accepted over the years, the theory was not proven until Sandford Palay identified the synapses by the first ultrastructural electron

microscopy investigations in 1956: "The absence of protoplasmic continuity across the contact surface between the two members of the synaptic apparatus is impressive confirmation of the neuron doctrine enunciated and defended by Ramón y Cajal during the early part of this century" (Palay, 1956).

1.1.2 Spine Morphology and its Impact on Function

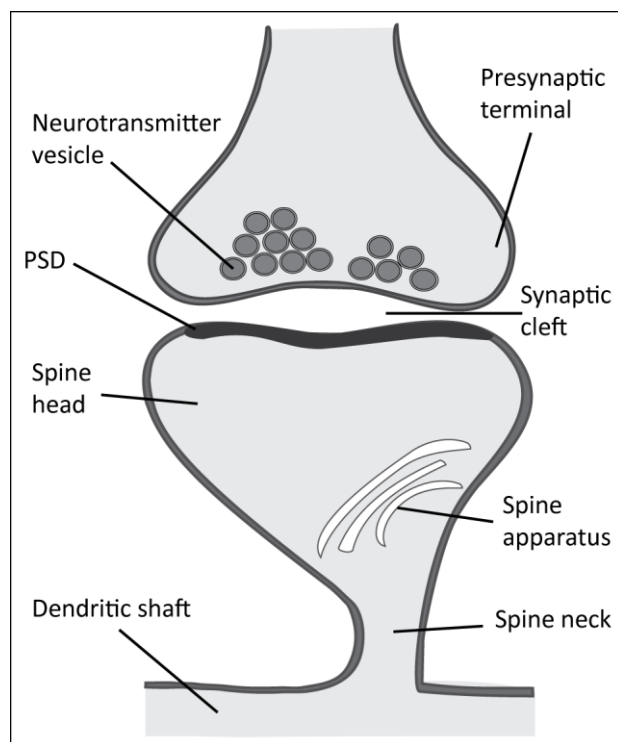


Figure 1.1: Schematic drawing of a synapse with basic nomenclature of relevant elements; PSD= post synaptic density.

With the establishment of electron microscopy on biological tissue in the 1950s, ultrastructure of spines could be investigated and synapses could be proven. Over the decades, spine morphologies were identified and many elements within the spine were discovered such as, the spine apparatus and the post-synaptic density (PSD), which were both described in E.G. Grey's landmark papers (Gray, 1959a; Gray, 1959b) (see Figure 1.1). The PSD is a complex of many proteins that organizes the neurotransmitter receptors in the synaptic cleft to conduct inner spine signal processing (Banker et al, 1974; Cohen et al, 1977). The size of the PSD was

found to reflect the strength of a synapse (Kondo & Okabe, 2011; Okabe, 2007; Sheng & Hoogenraad, 2007). Grey also divided synapses into asymmetric (type I) and symmetric (type II) synapses, according to the size of the PSD: Type I synapses have a thicker PSD and appear therefore asymmetric in EM. They can mostly be found on spines, are excitatory and use e.g. glutamate as a neurotransmitter (glutamatergic). Symmetric synapses are inhibitory and GABAergic (Neurotransmitter: g-aminobutyric acid; GABA) or glycinergic. These inhibitory synapses are usually found on dendritic trunks and somata but not on spines. The spine

apparatus is composed of smooth endoplasmic reticulum (SER) and is assumed to play a role in Ca^{2+} regulation within the spine (Majewska et al, 2000a), and, if missing, correlates with alterations in long-term plasticity (Deller et al, 2003). In addition to the PSD and the spine apparatus further elements such as mitochondria (Adams & Jones, 1982), actin (Fifkova & Delay, 1982), endosomes (Cooney et al, 2002), and proteasomes (Ehlers, 2003) were reported. In 1969, Jones & Powell and Peters & Kaiserman-Abramof continued ultrastructural EM studies and first classified dendritic spines by their morphology into mushroom, thin, and sessile (stubby) spines (Jones & Powell, 1969; Peters & Kaiserman-Abramof, 1969). This classification is still used in today's description of spines. Many publications support the close relationship of morphology and function of the spine: The volume of the head, for example, is directly proportional to the size of the PSD (Freire, 1978), to the number of postsynaptic receptors and the size of the presynaptic terminal (Peters, 1987; Spacek & Hartmann, 1983), to the number of docked synaptic vesicles and to the readily releasable pool of neurotransmitters (Harris & Stevens, 1988; Nusser et al, 1998; Schikorski & Stevens, 2001; Spacek & Hartmann, 1983). The size of the spine head was shown to directly correlate with the number of AMPA receptors in the PSD which influences the capacity of the spine to be stabilized by long-term potentiation (LTP) (Kasai et al, 2003; Matsuzaki et al, 2004). With the development of the two-photon microscopy (Denk et al, 1990), it was also possible to monitor dendritic spines *in vivo* (Svoboda et al, 1997). Numerous studies using this method have shown that large spines are more stable than small ones and thus, are able to persist over months (Grutzendler et al, 2002; Kasai et al, 2003; Matsuzaki et al, 2004; Trachtenberg et al, 2002). Data on AMPA receptor density, LTP, and spine size correlation led Kasai to hypothesize that there are spines for learning and spines for memory. Large spines are more stable and persistent and are therefore deemed (long-term) memory spines in that they form stable synaptic connections. Small or thin spines, however, are motile and instable and therefore build weak connections which might be responsible for learning (Kasai et al, 2003). This hypothesis can be strengthened by the observation that old animals bear more large (memory-) spines in comparison to young animals (Holtmaat et al, 2005).

In addition to the significant relevance of the spine head's structure to its neuronal function, a functional interplay of the spine neck has also been shown. In 1952, Chang postulated that

the spine necks offer considerable ohmic resistance due to their extreme slenderness. Thereby, the synaptic weight of a synapse could be reduced (Chang, 1952). Rall and Rinzel provided computational models, which introduced spine plasticity and the theoretical impact of spine necks on the nervous system (Rall, 1964; Rall, 1974; Rall & Rinzel, 1971a; Rall & Rinzel, 1971b). “[...] fine adjustments of the stem resistances of many spines [...] could provide an organism with a way to adjust the relative weights of the many synaptic inputs [...]; this could contribute to plasticity and learning of a nervous system” (Rall & Rinzel, 1971a). Crick supported the idea of a long and thin spine neck changing the weight of a synapse (Crick, 1982), whereas, ten years later, this theory was doubted by Koch and Zador. They assumed that the conductance of the spine neck is too large to provide effective modulation of the synaptic current, and therefore strength, that is generated by the spine head (Koch & Zador, 1993). Instead, they proposed that the spine produces a biochemically isolated compartment as a result of the thin diameter of the neck. This barrier theory is supported by other studies (Holmes, 1990; Majewska et al, 2000a; Nimchinsky et al, 2002; Segal, 2005; Svoboda et al, 1996). The biochemical diffusion barrier plays a very important role regarding Ca^{2+} regulation, which can act as a second messenger in various signaling pathways with spine plasticity like memory and learning (Alvarez & Sabatini, 2007; Ethell & Pasquale, 2005; Hayashi & Majewska, 2005; Konur & Ghosh, 2005; Korkotian & Segal, 1999; Majewska et al, 2000a; Majewska et al, 2000b; Oertner & Matus, 2005; Segal, 1995; Segal, 2005; Yuste & Bonhoeffer, 2001; Yuste & Bonhoeffer, 2004; Yuste & Denk, 1995; Yuste et al, 1999; Yuste et al, 2000). Furthermore to the morphological diffusion barrier, it was observed, that spine apparatuses are preferentially located at the base of the neck of mushroom spines, whereas it is lacking in many thin spines. This suggests that this element might regulate Ca^{2+} levels inside the spine. In electro physiological single spine stimulation, it could be observed that calcium only enters the stimulated spine head, while its shaft and neighboring spines are unaffected (Koester & Sakmann, 1998; Kovalchuk et al, 2000; Yuste & Denk, 1995).

The listed examples show the close relationship of dendritic spine morphology to its physiological function. The size and volume of the head and the length and diameter of the neck are directly comparable to the strength of a synapse and therefore to the strength of the connection between individual neurons. Investigating dendritic spines in fine detail to

describe these features, can lead to a better understanding on how the communication, learning, and memory works. In this thesis a new method on how to extract quantitative single spine morphologies will be addressed. To bring this method into context, approaches of how spines are more or less quantitatively characterized will be introduced in the following sections.

1.2 Light Microscopy

1.2.1 Techniques and Limitations

Since Cajal, there have been many scientists interested in spines and their morphologies. The most commonly used method is light microscopy. However, already in 1873 Ernst Abbe realized that the maximum achievable resolution, or light diffraction limit (d), is limited by the wavelength of the light (λ), the refraction index (n), and half the aperture angle of the objective ($\sin\alpha$) $d = \frac{\lambda}{2n\sin\alpha}$ (Abbe, 1873). With today's high-end objectives (NA=1.4), a maximum resolution of 180nm can be calculated (GFP emission = $\lambda = 509$), however, due to tissue scattering and different refraction indices of tissue, oil, and cover glass, the achievable resolution limits at 200-300nm. Thanks to the adaptation of the green fluorescent protein in the early 1990's and the possibility of genetically labeling neurons, the development and application of new microscopy methods was possible. Numerous different fluorescent microscopy techniques have been developed to date. Since common epifluorescence microscopy illuminates the whole tissue, phototoxicity, bleaching, and scattered light limit the application for the analysis of small structures. Figure 1.2 illustrates the working principle of the nowadays used fluorescence microscopy systems.

The longtime available confocal laser-scanning microscopy (CLSM) uses a laser to raster the tissue (Fine et al, 1988). Thereby only fluorophores in the laser's path are illuminated, which reduces bleaching and toxicity. Additionally, the light is collected via a pinhole, so that only photons of the focal plane are obtained. This way, the longitudinal z- resolution can be

brought to Abbe's light diffraction limit. Due to the limited penetration of short-wave photons, the 1990 developed two-photon laser-scanning microscopy (2PLSM) is commonly used *in vivo* (Denk et al, 1990; Helmchen & Denk, 2005). In addition to the advantage of deeper tissue penetration, the energy needed to obtain fluorescence is lower, which reduces phototoxicity and bleaching. The drawback of 2PLSM to CLSM, however, is that due to the longer wavelength, the theoretical resolution is worse. Both systems are frequently used to investigate spines but they cannot resolve below Abbe's limit. Recently, the stimulated-emission-depletion (STED) microscopy was developed and applied *in vitro* and *in vivo* to investigate dendritic spines. This microscopy can resolve structures down to 20nm which is at the level of EM resolution (Ding et al, 2009; Hell & Wichmann, 1994; Naegerl et al, 2008). The following section outlines how these light microscopy techniques are used to investigate spine morphologies.

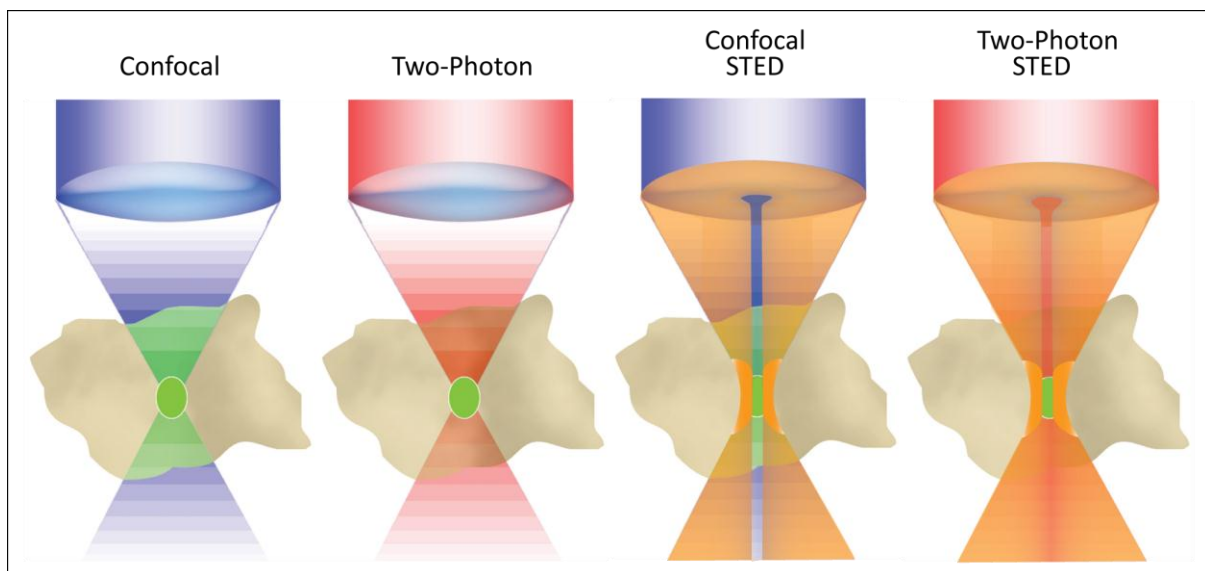


Figure 1.2: Schemata of the beam path of different fluorescence microscopy systems. For all systems the main fluorescence (green) lies in the focus point (green ball) but in confocal microscopy the tissue over and under the focus point is also excited. This is a result of the high energy blue laser beam. The two-photon microscopy, on the other hand, uses long-wave infra-red and therefore low energy multi-photon fluorescence. Only in the focus spot the photon density is high enough to enable the simultaneous absorption of the energy of two photons to trigger fluorescence. Stimulated emission depletion (STED) can increase the resolution by depleting the excited fluorophores with an interfering photon doughnut, leaving only a small hole where fluorescence can occur. As a consequence, resolutions of 20nm can be obtained. The excitation can either be single- or multiphotonic (modified from (Diaspro et al, 2006)).

1.2.2 Spine Morphology in Light Microscopy

To learn more about spine morphology, scientists use different approaches to characterize these protrusions. Since normal bright field microscopy on opaque stained neurons suffers from resolution problems due to the light diffraction limit and tissue scattering, most studies are being carried out using high resolution fluorescence microscopy techniques. However, three studies on spine densities in bright field light microscopy are worthy of being mentioned. Martin L. Feldman and Alan Peters demonstrated in 1979 that spines can be counted in light microscopy if a correction factor for the obscured spines is applied (Feldman & Peters, 1979). This principle was used by Alan Larkman in 1991, to quantify spine distributions on cortical neurons (Larkman, 1991). For an investigation of individual spine morphologies, however, this method is not suitable due to tissue scattering and resolution deficits. To realize the importance of quantitative spine morphologies, another bright field study should be mentioned. In 2003, Sila Konur presented a study where she counted and reconstructed 23000 spine morphologies in Camera Lucida to measure the diameter of the spine heads in bright field microscopy and analyzed the spine size according to their distribution without any classification of individual spines. Her measured mean values were $417\text{-}424\text{nm} \pm 122\text{nm}$ for all spines (Konur et al, 2003). At this point, it is important to bethink of Abbe's law introduced in the last section.

Apart from monitoring spines *in vivo* and *in vitro* to investigate plasticity and function as described in section 1.1.2, there are some studies that try to characterize and cluster single or multiple dendritic spines using high resolution light microscopy systems like CLSM, 2PLSM, or STED which were described in the last section (Brusco et al, 2010; De Simoni & Edwards, 2006; Hugel et al, 2009; Naegerl et al, 2008; O'Brien & Unwin, 2006; Rodriguez et al, 2008; Roelandse et al, 2003). Just recently, Janaína Brusco and colleagues used confocal microscopy to quantitatively describe and classify dendritic spines morphologically (Brusco et al, 2010). They analyzed approximately 1800 spines on dendritic segments from 16 different neurons of the amygdala and observed roughly 3% of spine morphologies that could not be classified into one of the three classic groups of thin-, mushroom-, or stubby spines found by Kaiserman- Abramof (see Figure 1.3(a.)). As previously mentioned, due to the limited resolution owing to Abbe's Law, light microscopy can only resolve structures

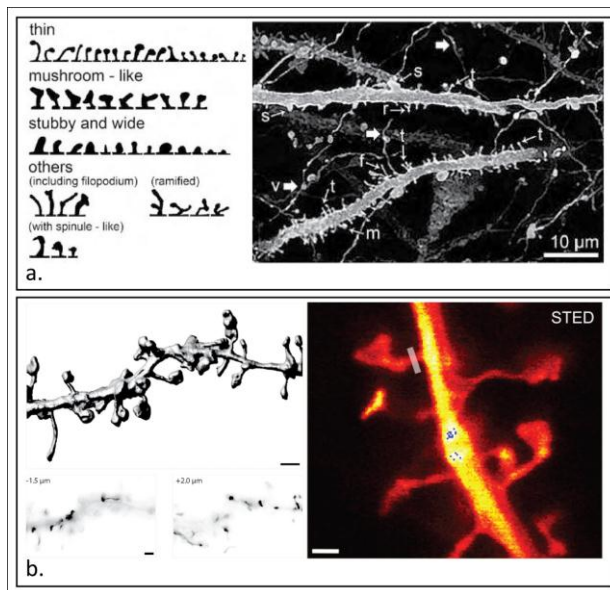


Figure 1.3: (a.): Spine classification and quantification using confocal microscopy, adapted from (Brusco et al, 2010); (b.): Volume reconstruction and original image obtained by STED microscopy, adapted from (Naegerl et al, 2008).

down to 200nm. STED microscopy is able to push the lateral resolution further by depleting fluorescence surrounding a focus point using a “light doughnut” (see Figure 1.2 and (Hell & Wichmann, 1994)). In this means, the lateral resolution is theoretically infinitesimal and in practice a lateral resolution of about 20nm has been published (Ding et al, 2009; Naegerl et al, 2008). The spines in Figure 1.3(b.) are nicely resolved, nevertheless, there are two major drawbacks to this method of investigating dendritic spine morphologies: (i) due to the high energy necessary for

STED, issues such as phototoxicity and bleaching prevail, which makes quantitative analysis, like Brusco et al. presented, unfeasible. (ii) The lateral resolution of 20nm is comparable to EM, however the longitudinal z-resolution cannot be improved by this method, thus, due to the light diffraction limit of 200-300nm (commonly a step-size of 500nm is chosen) these morphologies are basically two-dimensional projections of the perpendicular viewing angle. Since dendritic spines are very thin and their necks can be as thin as 30 nanometers (Harris et al, 1992), even this superresolution microscopy is missing a lot of information regarding structures along the longitudinal axis. In order to measure accurate volumes and sizes, it is important to gather information in an isotropic manner. The electron microscopy is the only technique that fulfills the demand of obtaining spine morphologies at high resolution in all three dimensions.

1.3 Electron Microscopy

Electron microscopy can resolve structures that are far below the light diffraction limit. Therefore, electron microscopy is used to investigate neuronal structures at a higher spatial resolution. To use EM, the tissue has to be made electron dense (contrasted) in order to resolve cellular structures. This is done by incorporating heavy metals into the tissue. In principle there are two different electron microscopy systems available: transmission electron microscope (TEM) and scanning electron microscope (SEM). Since contrast of biological samples is in principle far better in TEM than in SEM and sectioning has not been established for SEM, dendritic spine analyses in EM are performed using serial section TEM.

1.3.1 Serial Section Transmission Electron Microscopy

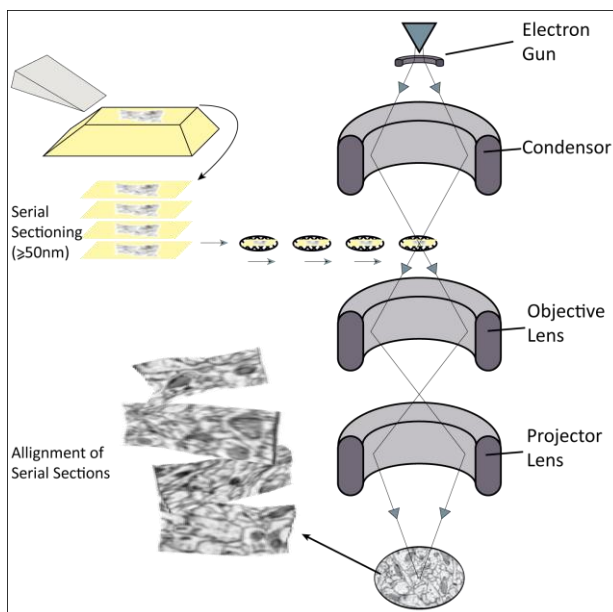


Figure 1.4: ssTEM: serial sections are cut from the embedded tissue block, mounted on imaging grids and transferred to the TEM. The beam path of the electron beam is the same as for light microscopy but the lenses are magnets. Images are taken sequentially with a CCD camera and have to be aligned and corrected for shrinkage and distortion before 3D registration.

For over 50 years serial section transmission electron microscopy (ssTEM) has been the standard to identify and study ultrastructures three dimensionally (3D) (Gay & Anderson, 1954; Knott et al, 2006). Figure 1.4 describes this method: serial sections are cut from an osmium tetroxide-fixed and thereby pre-contrasted embedded tissue block. The individual sections are collected and transferred onto imaging grids and post-contrasted with uranium acetate and lead citrate. The mounted sections are placed into a TEM and a high vacuum is applied. Images are acquired using beam energies of 60-150keV. The working principle is that the

high proton containing heavy metal atoms in the section refract the beam electrons and only the electrons that pass through are detected by a phosphorus screen, on photographic film, or nowadays via a CCD camera. ssTEM is very demanding, laborious, and time consuming as every section has to be manually managed as described above. By applying this method to large tissue blocks it is very likely that artifacts are introduced e.g. cutting artifacts (such as shrinking, stretching, and disruption), losing sections, and post-imaging alignment issues (Hoffpauir et al, 2007). This is why most spine studies only scan and reconstruct small image stacks of a maximum of some tens of μm of dendritic length. Another drawback, in comparison to the lateral resolution of down to 0.1nm, is the longitudinal z-resolution. This is limited by the coherence of the cut slices which lies at around 50 nm and can still make structures like particularly small spine necks pass undetected (Harris et al, 2006). This resolution is, however, at least 4 times higher than that which can be achieved with light microscopy.

1.3.2 Spine Morphology in the Electron Microscope

Thanks to its high resolution, fine structures such as spines and most of their necks, can be accurately analyzed and reconstructed using EM (Harris et al, 2006; Rostaing et al, 2006). Several studies have investigated spine morphologies and connected the morphology to the physiological function (see section 1.1.2). In comparison to functional research, far fewer studies have concentrated on spine morphologies and extract morphological 3D reconstructions to obtain values for volumes, head and neck diameters, or a classification (Arellano et al, 2007; Chicurel & Harris, 1992; Fiala et al, 2002; Harris et al, 1992; Harris & Stevens, 1989; Schikorski & Stevens, 1999; Spacek & Harris, 1998). Two independent studies on spine morphology, almost 20 years apart, are displayed in Table 1.1. Kristin Harris investigated spine properties on hippocampal CA1 pyramids of the rat (Harris et al, 1992) and a more recent study from Jon Arellano measured spine morphological variables on L2/3 pyramidal neurons in the visual cortex in mouse (Arellano et al, 2007). Considering the fact, that the measured values presented in Table 1.1 are highly similar although the data is derived from different parts of the brain and from different species with different input

Feature	<u>Harris et al 1989</u>			<u>Arellano et al 2007</u>		
	N	Mean±SD	Range	N	Mean±SD	Range
Synaptic PSD area (μm^2)	100	0.069±0.08	0.008-0.54	133	0.08±0.06	0.01-0.33
Spine volume (μm^3)	100	0.062±0.08	0.004-0.56	133	0.09±0.07	0.01-0.38
Head	100	0.051±0.07	0.003-0.55	110	0.07±0.06	0.01-0.30
Neck	92	0.012±0.01	0.0004-0.07			
Spine surface area (μm^2)	100	0.83±0.63	0.13-4.38			
Head	100	0.61±0.57	0.10-4.24			
Neck	92	0.24±0.17	0.02-0.89			
Axonal varicosity (μm^3)	58	0.11±0.11	0.005-0.76			
Vesicle number	58	223±245	3-1606			
Spine length (μm)	100	0.95±0.42	0.24-2.46			
To PSD	100	0.82±0.36	0.16-2.13			
Head	100	0.53±0.28	0.15-1.89			
Neck	92	0.45±0.29	0.08-1.58	110	0.66±0.37	0.1-2.21
Neck diameter (μm)	92	0.15±0.06	0.038-0.46	110	0.20±0.06	0.09-0.51

Table 1.1: Spine properties from two independent studies from different neurons, taken from (Harris & Stevens, 1989) and (Arellano et al, 2007).

patterns, these two studies illustrate three rather basic yet important issues: (i) numerous parameters can be measured from 3D EM reconstructions, (ii) the sub cellular structures can be very small (neck diameter down to 38nm) and (iii) relatively small numbers (N=100; 110-133) of spines were analyzed. Harris obtained the 100 spines from dendrite stretches of 6-12 μm in length. Arellano states that he could obtain 15 series ranging from 21 to 52 serial sections (50-70nm thick) that would correlate to a length of 1.26-3.12 μm (calculated for 60nm thickness). Due to the laborious and error-proneness of ssTEM and the subsequently registration, usually only short pieces of dendritic structure can be obtained for evaluation (see Figure 1.5). Taken together, electron microscopy is the only present imaging technique to resolve fine nanoscopic structures like spine necks in all three dimensions. However, the disadvantage in quantitatively obtaining morphologies from long stretches of several μm of dendritic structure requires an enormous effort to obtain and process post-procedures such as shrinkage- and torsion correction, alignment, and 3D registration. In addition, the representativity of small stretches of some μm is ultimately questionable, as the spine density on one particular neuron can vary; most likely the spine sizes are different for different types of dendrites or regions. One strategy in this thesis was to obtain quantitative

spine morphologies similar to the studies of Brusco et al. or Kunar et al. but at a reasonable three dimensional resolution such as that presented in this section. Another attempt was to scan an entire neuron at nanoscopic resolution to be able to investigate if there is a specific spine distribution and a change in spine morphologies within one particular cell.

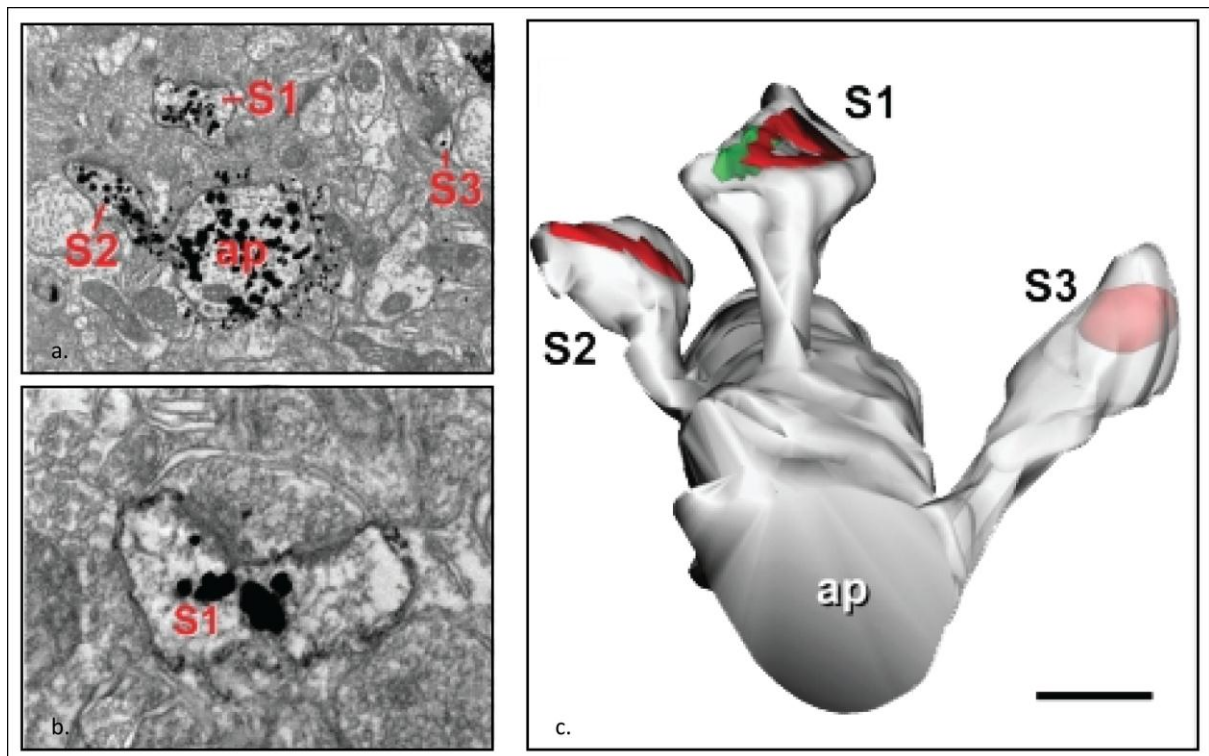


Figure 1.5: (a.) and (b.): Original cross-sections marking the apical dendrite (ap) and the three reconstructed spines (S1-3); dark black precipitates owe to Golgi Staining; (c.): 3D-reconstruction of the three spines present in (a.) and (b.); scale bar= $1\mu\text{m}$ in (a.), $0.3\mu\text{m}$ in (b.), and $0.6\mu\text{m}$ in (c.) (modified from (Arellano et al, 2007)).

1.3.3 Scanning Electron Microscopy

The other most well used electron microscopy technique is Scanning Electron Microscopy (SEM). In biological samples are two kinds of electrons of greatest interest that can be obtained from SEM: (i) the secondary electrons (SE) and (ii) the back-scattering electrons (BSE). SE are responsible for the topographic contrast of a sample, thus giving a plastic 3D surface impression of the sample, whereas the energetically higher BSE results in a more flat “photography” of the surface (Goldstein et al, 2003). Figure 1.6(a.) schematically diagrams the principle of an SEM. The emitter on top of the column emits an electron cloud which is accelerated by the anode right beneath the electron gun. In comparison to a TEM the

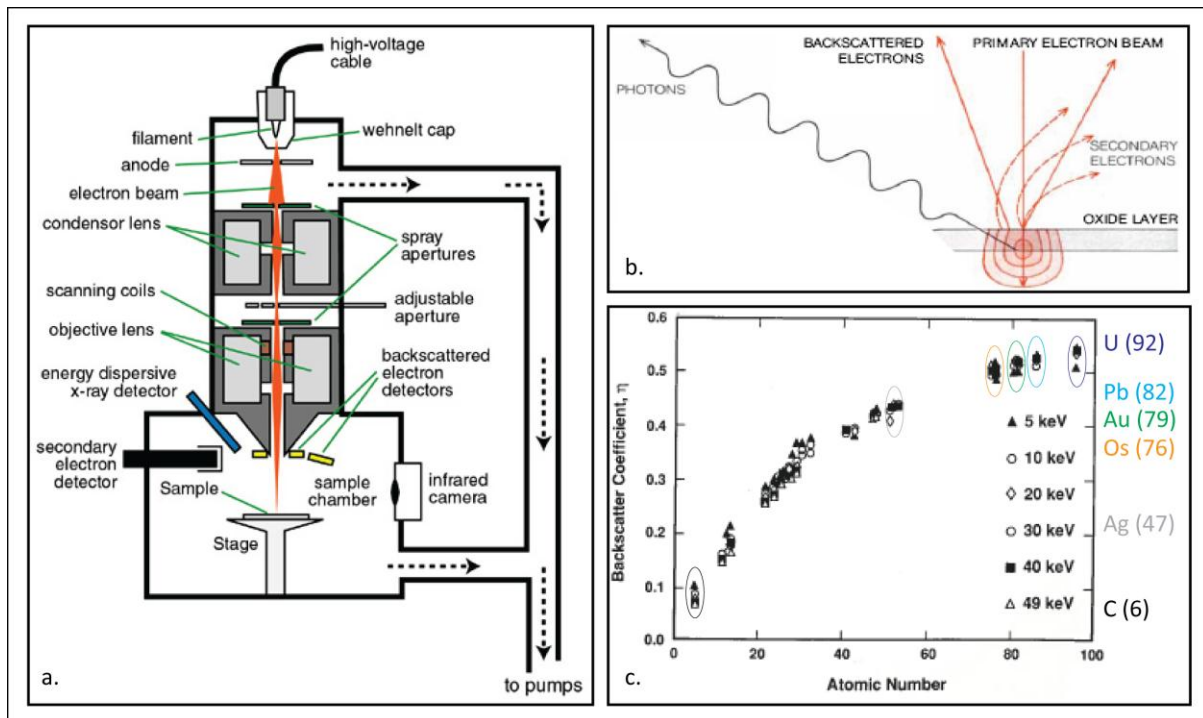


Figure 1.6: (a.): Schematic representation of an SEM (taken from (Wittke, 2008)); (b.): Origin of SE and BSE (modified from (Everhart & Hayes, 1972)); (c.): Backscattered electron coefficient as a function of atomic number plotted for a range of beam energies from 5keV to 49keV; selected elements are marked, Atomic number Z in brackets (modified from (Goldstein et al, 2003)).

acceleration energy (0.1-30keV) is rather low. The electron beam passes down condenser and focus lenses, and different apertures in the column so that the focused beam hits the target sample in the microscope chamber at the bottom. Arriving at the sample, the beam electrons have in principle two possibilities: they are either absorbed by the sample or they trigger electrons inside or on the surface of the specimen to escape and be detected as one of the signals mentioned above. Two detectors, the Everhart-Thornley SE detector (Everhart & Thornley, 1960) in the back of the chamber and the solid-state BSE directly on top of the sample, detect the electrons that are reflected by the sample. SE and BSE electrons derive from different effects (Figure 1.6(b.)). The SE are energetically low and defined as all electrons escaping the sample with an energy less than 50eV (Lee, 1992). They derive from loosely bound outer shell electrons from the specimen atoms that received enough energy from the electron beam to be ejected and brought into motion. Thereby these electrons themselves create a cascade and set other electrons in motion or escape the specimen, where they are detected by the SE detector. The lower the acceleration energy of the electron beam, the fewer electrons are evoked by deeper layers of the specimen and thus the more intense the 3D surface representation. The BSE electrons are high energy electrons

that escaped from the sample after hitting the surface and usually rebound in a straight angle from the specimen's surface. The beam electrons produce many elastic and inelastic collisions between electrons and atoms of the specimen. Elastic scattering can be thought of as a billiard model where the collision of the electron with a larger atom changes the trajectory of the electron. Therefore, larger atoms (with a greater atomic number, Z) have a higher probability of producing an elastic collision because of their greater cross-sectional area. Consequently, the number of backscattered electrons reaching a BSE detector is proportional to the mean atomic number of the sample (Goldstein et al, 2003). Thus, a stronger BSE intensity correlates with a greater average Z in the sample, and weak contrast areas have a lower average Z . This correlation is called the "Backscattering Coefficient" and is displayed for several atoms and energies in Figure 1.6(c.). This atomic number contrast can also be used to identify specimen composition, however the difference becomes rather minimal for elements above $Z=50$ (Goldstein et al, 2003). The sample preparation for SEM and TEM is quite similar, with the exception of two points: (i) SEM samples need to be completely block-stained as the block is not segmented before scanning (exception: ATLUM (see below)) and (ii) samples need to be electrically conductive and grounded. Nonconductive specimens tend to charge by the electron beam when scanned and, especially for SE imaging, this causes scanning faults and image artifacts. Therefore, SEM samples are usually coated with an ultrathin layer of conductive heavy material such as gold, palladium, platinum, chromium or a thin layer of graphite. As mentioned above, the contrast of biological samples is tremendously better in TEM than in SEM, and serial sectioning for SEM is still under development, most of the dendritic spine analyses in EM are performed in ssTEM. Recently however, serial section SEM (sSEM) is becoming popular as a method for high-throughput automatization. The "Automatic Tape-Collecting Lathe Ultramicrotome" (ATLUM) is supposed to cut thousands of serial sections (50nm thick) from an embedded block of brain tissue and collect them on a long carbon-coated tape on which they are post-stained and imaged in an SEM (Lichtman & Heyworth, 2010; Ogura et al, 2010). The advantage of sSEM systems is its possibility to completely automatize the sectioning and imaging of the sections. Since no human interaction is required, the time required for image acquisition is reduced, more regular, and can be performed 24 hours a day, 7 days a week with no artifacts due to human interaction and transport of the sections. Other methods that use a kind of sSEM are focused ion beam (FIB-SEM) and serial block-face SEM (SBFSEM)

(Denk & Horstmann, 2004; Knott et al, 2008). Both systems are completely automated and raster scan the surface before sectioning inside the SEM. This allows automatic recording of intrinsically aligned image stacks. The FIB-SEM uses an ion beam to ablate a section of the sample, while the SBFSEM uses a small microtome cutting down the surface. Imaging the surface before sectioning enables recording of sections thinner than 50nm as the coherence of the cut-off section is not an issue. In this thesis an SBFSEM was used to obtain the data presented in this study. Therefore, the method will be explained in more detail in the following section.

1.3.4 Serial Section Block-face Scanning Electron Microscopy (SBFSEM)

The concept of SBFSEM, which was applied by Winfried Denk in 2004 (Denk & Horstmann, 2004), had already been proposed in the early 1980's by Stephan B. Leighton (Leighton, 1981). The principle of SBFSEM is an automation of the scanning and sectioning process. Therefore, a custom build ultramicrotome is incorporated inside the scanning chamber. The images are acquired by a scanning microscope. The inner workings, however, are quite different to an ordinary SEM. Since for common SEM the sample has to be coated with a conductive layer, this is not possible for the surface as it is sectioned inside the chamber. Therefore a derivative of the SEM, the environmental scanning electron microscope (ESEM) (Figure 1.7(a.)), is used for imaging the surface. The ESEM can be fundamentally characterized as a leaky SEM since the different compartments of the microscopy have different vacuum zones and the specimen chamber can be set to a very low vacuum (10-70 mbar). The low vacuum is set by a needle valve that directs water vapor or gas into the specimen chamber. With this technique, it is possible to investigate wet, non-dehydrated, possibly unfixed, and non-coated structures or even whole organisms in EM (Donald, 2003). Naturally, the vapor interacts with the electron beam and the electrons to be detected. On the one hand side, the water (or gas) molecules scatter the beam electrons as well as the escaping electrons, which results in a blurring of the recorded image. On the other hand the electron beam ionizes the vapor which helps to reduce the charging of the sample. Not all beam electrons escape from the sample and charge the sample. Usually the sticking electrons are conducted by the coating of the surface. As this is not possible, the electrons

charge the surface unless the ionized water molecules take away the charge. Figure 1.7(b.) describes how the water (or gas) molecules in the chamber are ionized by the beam electrons and electrons emitted from the surface. In addition, to each positively charged ion a daughter electron is created as well. The positive ions take up the charge off the negatively charged sample surface, while the electron is accelerated towards the positively charged solid state BSE detector. On its way, the electron collides with BSE and especially with the low energetic SE, which leads to additional blurring of the detected image. Thus, the dose of vapor must be carefully adapted to ensure that no charging artifacts occur and that the image is still sharp. To further optimize the signal to noise ratio for ESEM, the distance of the sample to the BSE detector is minimized to only a few millimeters. The SBFSEM uses such an ESEM. Therefore, the imaging and microtome built inside the chamber need to be compatible with low vacuum conditions. In Figure 1.8(a.) the scanning chamber of the microscope is displayed. The working principle is to scan the surface of the sample, then cut down the surface, take another image and so on and so forth. This is conducted by three computers: (i) The microtome computer driving the cutting and moving the sample, (ii) The FEI (microscope's) support computer taking images and operating the EM, and (iii) one master computer telling the other two when to cut, move or take an image. In this way, a 3D image stack can be acquired.

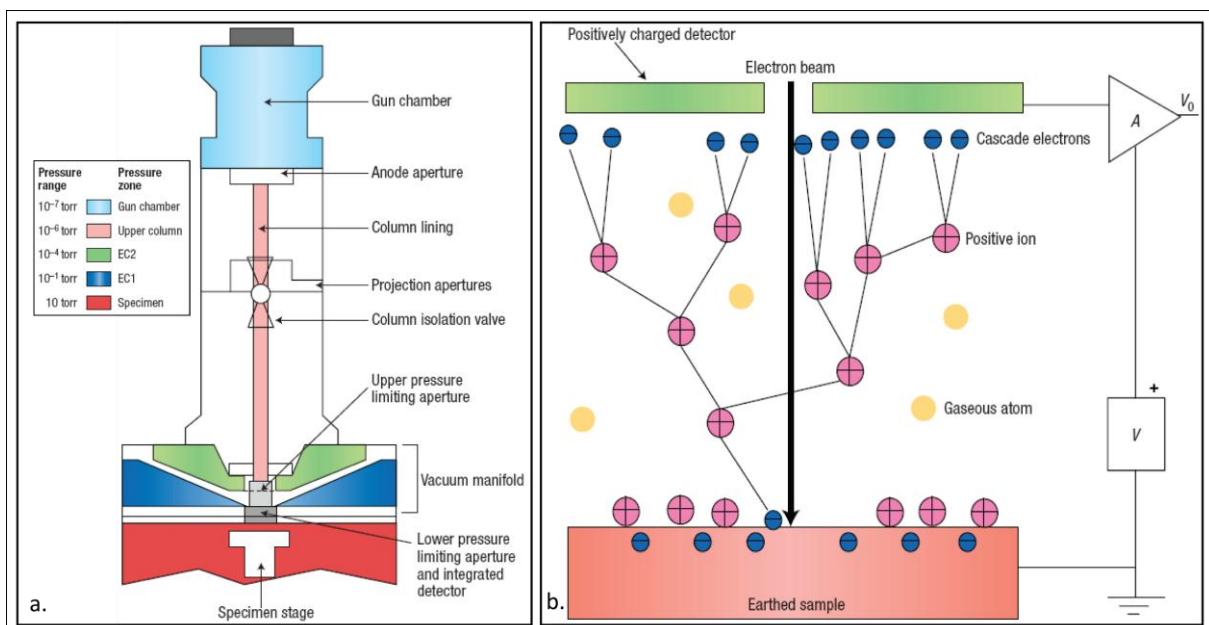


Figure 1.7: (a.): Schematic view of an ESEM; (b.): influx of gas or water vapor is compensating for the deposited charge on the sample's surface but also interacts with the beam electrons, BSE, and SE (modified from (Donald, 2003)).

Figure 1.8(b.) shows photographs of a sample in the sample holder (1) and the diamond knife (2) in the knife holder. Assuring that the sample stays in the focus plane, the knife is not moving towards the sample in z (as in common microtomes) but a piezo z -motor is moving the sample up and down, so that the surface always remains in the correct focal plane. To make a cut, the knife cuts forward and then retracts. A precision x - y stage moves the sample over a user defined scanning grid, so that mosaic images can be acquired and an area larger than the field of view can be covered. The x - y position jitter lies below 10nm. The solid-state BSE detector is localized to about 6mm over the sample. There are several advantages of SBFSEM in comparison to ssTEM but also two disadvantages. The disadvantages are that due to the x - y jitter the lateral resolution cannot be as high as in TEM and, as already mentioned, the contrast in SEM is principally inferior. The advantages on the other hand are numerous. Since the surface is imaged before cutting, sections can be much smaller than 50nm. In the first generation of SBFSEM the cutting size was also limited to 50nm, however, the second generation of SBFSEM can achieve cutting steps of 23nm and lateral resolution of 12nm (Briggman et al, 2011; Denk & Horstmann, 2004), while the SBFSEM used in this thesis scanned with a voxel size of 24x24x30nm. Apart from the benefit of the increased longitudinal resolution benefit, the SBFSEM is highly automated and scans around the clock without any user interaction. Since the sample block is intrinsically aligned,

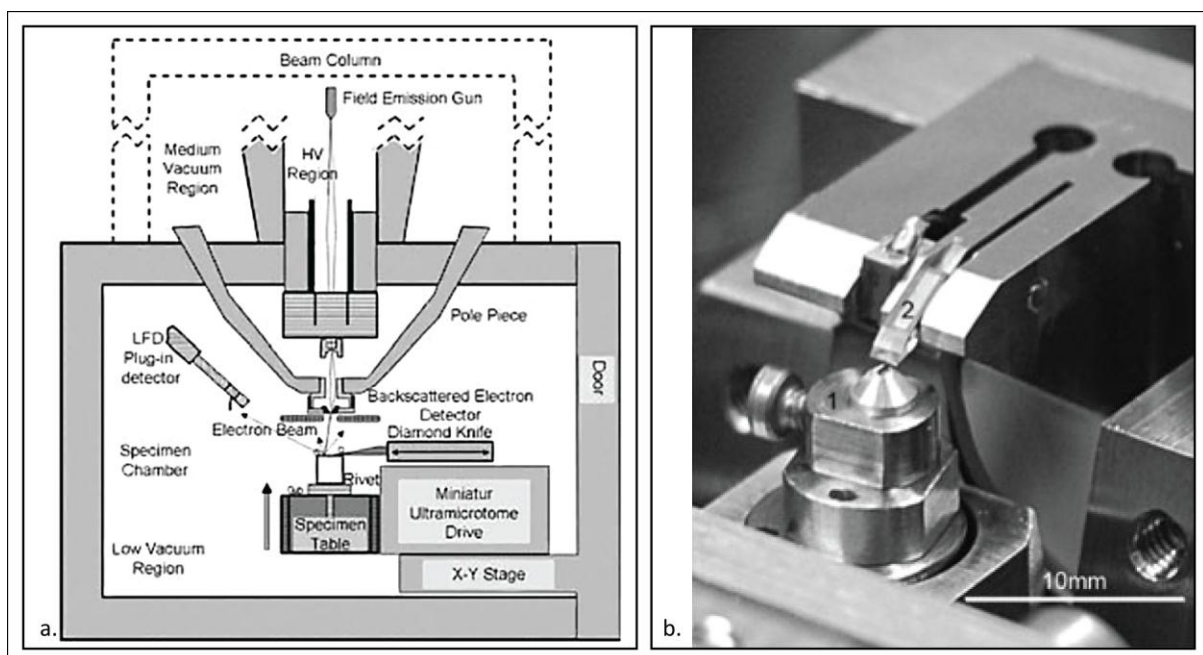


Figure 1.8: The SBFSEM; (a.): schematic drawing of the scanning chamber; (b.): Photography of the actual sample holder with sample (1) and the diamond knife in the microtome (2) (modified from(Zankel et al, 2009).

all post-scan corrections for distortion, corruption or loss are avoided, and post-alignments are not necessary. The speed of an SBFSEM is limited by the pixel dwell time (pdt), which is the length of time that the electron beam remains on one single pixel. This time is basically depending on the contrast of the sample, the detector sensitivity, and what signal to noise ratio has to be achieved. The longer the pdt, the more BSE are triggered from the pixel and therefore the more contrasted the image, but the stronger the charging of the insulating sample will be. Moreover, the acquisition time will increase. As an example, the pdt used to gather images in this thesis was $8\mu\text{s}/\text{pixel}$ which results in an acquisition time of about 30s per image. To summarize, the SBFSEM technique allows one to obtain large quantitative data at (almost) isotropic nanoscale resolution fully automatically without the drawbacks of section distortion or alignment errors. For this thesis an SBFSEM was used to scan single neurons that were previously identified in a light microscope and filled with a tracer. A specific staining protocol for these cells was developed, which is part of this thesis. In parallel, to extract the information from the recorded data stacks, a computational approach was developed in cooperation with the Stefan Lang and Panos Drouvelis at the “Interdisciplinary Center for Scientific Computing” in Heidelberg.

1.4 Segmentation of Large Electron Microscopic Datasets

Most of the data acquired by EM is segmented by manual tracing to obtain the morphological information in the images and the most widely used tracing tool is the freeware program “Reconstruct” (Fiala, 2005; Fiala & Harris, 2001). It has a simple 2Dslice viewer and allows the user to manually draw boundaries of neuronal cells in EM images. Ju Lu and colleagues extended the toolbox with a region-growing method for semiautomatic segmentation (Lu et al, 2009). Some other open source and commercial software packages, such as the NeuronJ plug-in for ImageJ (<http://rsbweb.nih.gov/ij/>), Bitplane’s Imaris (www.bitplane.com), and Amira (Visage Imaging), provide automatic segmentation and tracking. Although such tools make routine reconstructions of single neurons and sets of neuronal processes possible, it also became evident that for large-scale 3D datasets a capacity for computerized processing of images is necessary (Bertalmio et al, 1998;

Briggman & Denk, 2006; Carlbom et al, 1994; Vazquez et al, 1998). Consequently, techniques for automated or semi-automated neuron reconstruction of images obtained by SBFSEM were developed (Helmstaedter et al, 2011; Jain et al, 2007; Jurrus et al, 2009; Macke et al, 2008). These studies focused on automation of tracing of neuronal processes in SBFSEM image stacks, that were stained using a cell membrane targeted HRP-DAB reaction. Macke used an edge detection algorithm paired with contour-propagation whereas Jurrus and Helmstaedter used Kalman Snakes “winding” through the tissue stack (Peterfreund, 1998; Peterfreund, 1999). Our aim is the complete computational tracing of thousands of single spine morphologies in a volume of the order of $\sim\text{mm}^3$ at nanoscale detail from defined single biocytin-filled neurons. Previous to this work, Stefan Lang and Enke Tafaj developed a custom segmentation algorithm that is able to extract morphological information from single biocytin-filled neuron (Lang et al, 2011b). However, neither segmentation nor staining of the single neuron was sufficiently developed. Thus, reconstructions resulted in

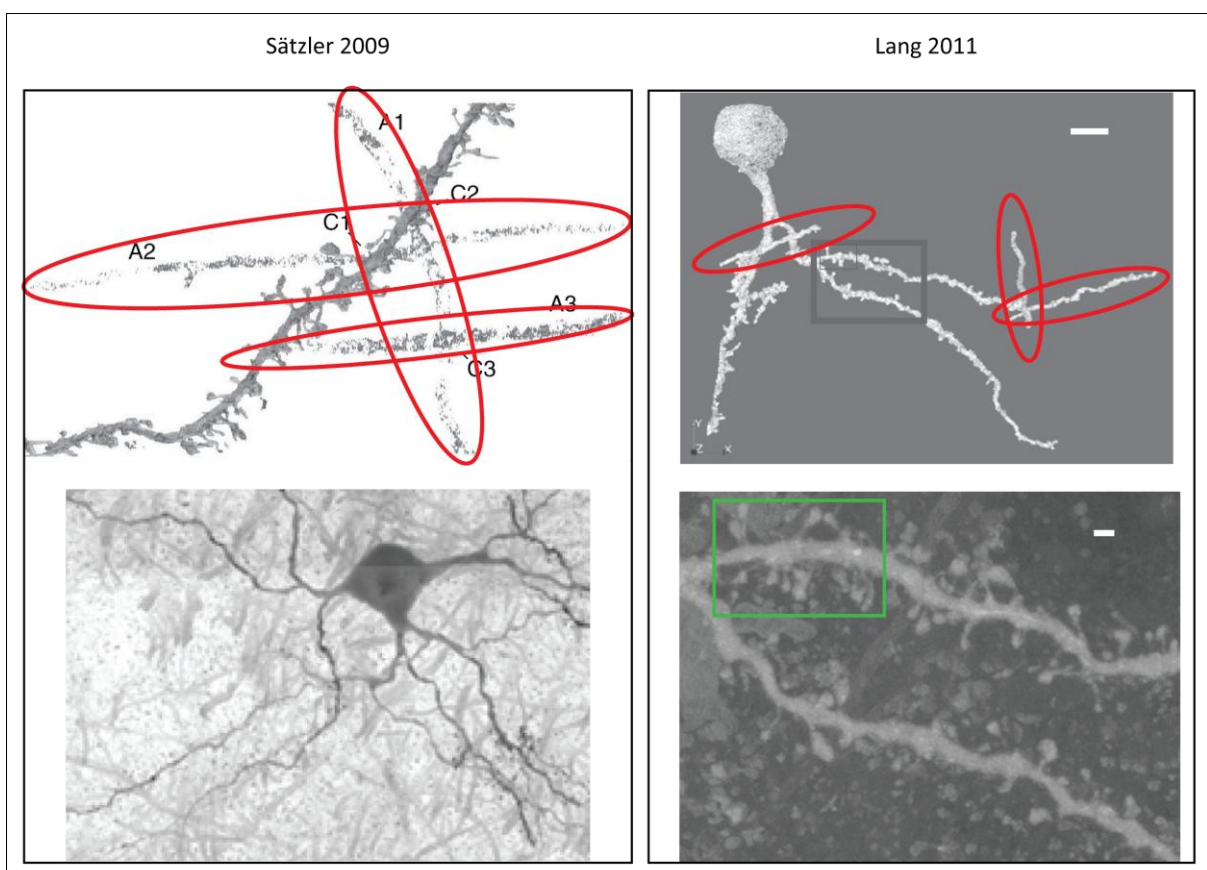


Figure 1.9: Segmentations on single biocytin-filled cells by Saetzler and Lang using two independent segmentation algorithms. Upper panels show reconstructions with artifact in red circles; lower panels show minimum and maximum (inverted) z-projections of the scanned neuron, many additional structures can be observed. scale bar in Lang et al: $10\mu\text{m}$ and $1\mu\text{m}$ (modified from (Saetzler et al, 2009) and (Lang et al, 2011b)).

segmentation artifacts, due to staining deficits (Figure 1.9). This was also true for a different approach by Kurt Saetzler who developed an alternative computational approach in parallel based on the same source data (Saetzler et al, 2009). Both reconstructions co-segment large structures that do not belong to the single neuron (Figure 1.9 red circles). In the minimum projection from Saetzler as well as the maximum projections (inverted) from Lang of the source data, a variety of different structures in the background can be observed. Thus, the first task in this thesis was optimizing the staining of single biocytin-filled neurons for SBFSEM.

1.5 Aim of this Thesis

Several studies have put spine morphology in context with their function. New methods like SBFSEM allow one to obtain nanoscopic information from large tissue volume. This thesis addresses the extraction of single spine morphologies from single pre-identified neurons in the mouse's somatosensory cortex. The results are presented in three sections:

- (i) An appropriate staining protocol for SBFSEM was found, optimized and quantified.
- (ii) In parallel, the segmentation algorithms of the neuronal structure from Lang et al. (NeuroStruct) were optimized, expanded, and validated in cooperation with Dr. Panos Drouvelis who also programmed the respective filters described in this thesis.
- (iii) Finally, both, staining protocol and improved toolbox, could be utilized to obtain quantitative nanoscopic data from nine individual neurons and from a single layer 5B neuron scanned in entirety. Preliminary evaluation of the obtained data is shown as are the first initial single spine morphologies that could be extracted.

Chapter 2 Materials and Methods

2.1 Methods

2.1.1 Tissue Preparation

2.1.1.1 Mice

In addition to wild type C57Bl/6 mice, the transgenic mouse line *GLT25d2 BAC-GFP* (GLT) from GENSAT was used (www.gensat.org). The line expresses GFP under the control of the promoter for “*glycosyltransferase 25 domain containing 2*” that is specifically transcribed in a small subset of thick tufted L5B neurons. Additional information can be found in (Groh et al, 2010).

2.1.1.2 Slice Preparation:

A mouse of 28 (+-1) days age was anesthetized using Isoflurane (cp-pharma). When agonal respiration could be observed, the mouse was quickly decapitated and the brain was prepared in ice cold slicing solution (in mM: 125 NaCl, 25 NaHCO₃, 2.5 KCl, 1.25 NaH₂PO₄, 1 MgCl₂, 3 myo-inositol, 2 Na-pyruvat, 0.4 ascorbic acid, 1 CaCl₂, 5 MgCl₂, 4.5g glucose) being oxygenated with Carbogen (95%O₂, 5%CO₂). The brain was transferred to a microtome (HM650V, Microm) and sectioned thalamocortically into 300µm thick slices according to (Agmon & Connors, 1991). Cut off slices were kept in an oxygenated storage buffer (in mM: 125 NaCl, 25 NaHCO₃, 2.5 KCl, 1.25 NaH₂PO₄, 1 MgCl₂, 2 CaCl₂, 25 glucose) at 37°C for 1h and then put at room temperature (RT) until use.

2.1.1.3 Filling of Single Neurons

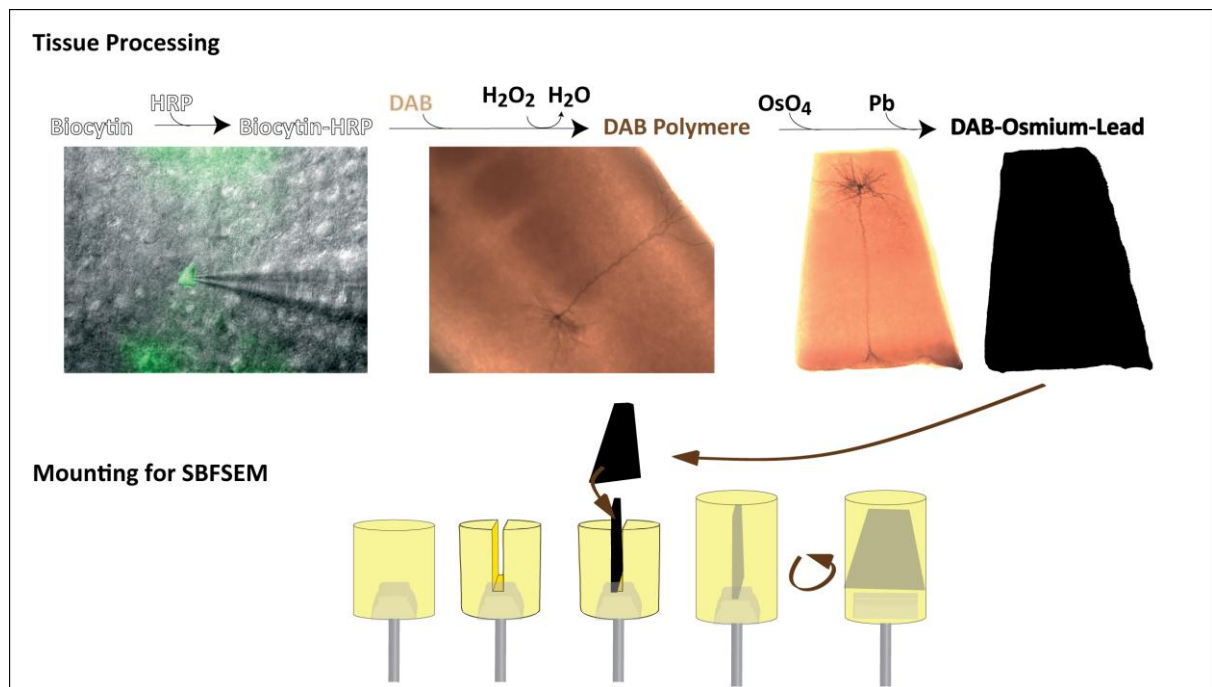


Figure 2.1: Workflow from patching a single neuron over DAB staining, EM contrasting, and mounting the sample.

The acute slice was put on a poly-lysine coated coverslip and transferred into a perfused slice chamber in the patch setup. The microscope was equipped with an LED excitation for the detection of GLT positive cells (GFP) and the fluorophore Alexa 594 (Red) present in the intracellular solution. The targeted neuron was patched with a freshly pulled patch-pipette with a $\sim 5\text{M}\Omega$ resistance and filled with an intracellular solution (in mM: 135 K-Gluconate, 10 HEPES, 10 Phospho-creatine-Na, 4 KCl, 4 ATP-Mg, 0.3 GTP) containing 0.2% Biocytin (Fluka) and 100 μm Alexa 594 (Sigma) by whole-cell filling. After 15 minutes of passive diffusion of the pipette-loaded solution, the pipette was removed and the cell was left in the setup for an additional 15 minutes to wash out extracellular biocytin. The slice was then immersion-fixed in CB containing 4% PFA overnight (O/N) at 4°C in a flat glass vial. It was taken care, that the slice was flat and covered with fixative. Although samples were eventually used for EM, no glutaraldehyd (GA) was used in the initial fixation, since after GA fixation the follow-up DAB staining did not work properly. For the EM staining described in this thesis not being a membrane staining but a cytosol staining, the membrane integrity was negligible.

Nevertheless, the tissue was GA fixed after the DAB staining to prevent micro-fractures due to osmolar tensions during contrasting and dehydration.

2.1.1.4 Staining Protocols

2.1.1.4.1 DAB Staining

The filled cells were stained for light microscopy with 3,3-diaminobenzidine tetrahydrochloride (DAB) using the avidin–biotin–peroxidase method (Horikawa & Armstrong, 1988) as follows: Tissue slices were fixed after filling in CB (0.1M Na-Cacodylate, pH7.3) containing 4% PFA O/N at 4°C in glass vials. The following day, slices were transferred to 24-well plates and washed in CB 3 times 10 min each. To block endogenous peroxidases, 3% H_2O_2 was applied for 15 min. followed by 6-8 times washing step in CB. After all bubbles had vanished, every single slice was incubated in 1 ml AS (Antibody Solution; CB containing 0.5% Triton-X100, 50 μ l A and 50 μ l B/5ml of Vectastain kit) O/N at 4°C. The next day, slices were washed 6 times in CB to wash out the AS and bring the slides to room temperature. After washing, every single slice was incubated in 1ml DAB Solution (CB containing 0.7mg DAB per ml) for 25 min. in the dark. The reaction was started by adding 1ml of DAB solution containing H_2O_2 (6.6 μ l/ml from 0.3% H_2O_2 solution) to one slice. The staining was controlled in a light microscope. The reaction was stopped by transferring the slide into a fresh well containing CB. Thereafter, the next slice was developed. After washing 4 times with CB, slices were transferred into CB containing 2.5% GA until contrasting for EM.

2.1.1.4.2 EM Staining Protocols

Before the tissue was contrasted in EM, the single neuron was cut out of the slice in a trapezoid shape under a stereomicroscope using a scalpel. The trapezoid shape was necessary for stability and orientation on the steel pin. A schematic flow from filling over staining to mounting is presented in Figure 2.1.

2.1.1.4.2.1 Osmium Tetroxide + Uranyl Acetate Staining:

Filling of this neuron was different, as it was performed *in vivo*: The neuron was filled with biocytin using current pulses (de Kock et al, 2007; Joshi & Hawken, 2006; Pinault, 1996). Pipettes were filled with (in mM): 135 NaCl, 5.4 KCl, 1.8 CaCl₂, 1 MgCl₂, 5 Hepes, pH 7.2 with NaOH, and 20 mg/ml biocytin. Bath solution contained 0.9% NaCl. Recordings were made using an Axoclamp 2B amplifier (Axon Instruments, Union City, CA, USA) in combination with a Lynx 8 amplifier, band filter settings 300 and 9000 Hz. Data were acquired using the Ntode Virtual Instrument (custom written software, R. Bruno, Columbia University, New York, USA) for Labview (National Instruments, Austin, TX, USA). The animal was then transcardially perfused with 0.9% Saline until the animal bleed out, then the solution was changed to 0.9% Saline containing 4% PFA until the neck was stiff. Hence, the brain was removed and fixed O/N in PB containing 4%PFA. The next day, the brain was sectioned tangentially to the barrel cortex in 100µm thick slices. Slices were DAB stained as described above except using PB.

EM contrasting was performed as follows:

The cut-out tissue block was washed 3x10min PB, and hence post-fixed with 2% OsO₄ (EMS) + 1.5% K-ferricyanide + 6.46% Succrose O/N. The next day the sample was dehydrated using ethanol (EtOH 30%/50%/70%/UAC/80%/90%/100% 20min each) followed by 10min of propylenoxid (PO). In between the dehydration 70%→80%, the sample was incubated for 1h in 1% Uranylacetate/1%Phoshowolfram in 70% EtOH. Thereafter, the sample was infiltrated by Epon through incubation in PO:Epon 3:1 (3h), 1:1 (3h), 1:3 (O/N) and 100% Epon (3h). Afterwards the probe was mounted and oriented on a steel pin cured at 60°C for 48h.

2.1.1.4.2.2 Osmium Tetroxide Only Staining:

Filling the neuron was performed as described in 4.1.2, except that no Alexa 594 was present in the intracellular solution and PB was used to fix the slide. DAB staining was the same as described above except that PB was used instead of CB.

After washing 3x10min PB, the tissue block was hence post-fixed with 2% OsO₄ (EMS) + 1.5% K-ferricyanide for 2h and washed in H₂O 3x10min. Dehydration was performed in methanol (MeOH 25%/70%/90%/100% 2x30min each). Epon infiltration was performed through MeOH:Epon incubation in 1:1 (O/N), 1:3 (3h) and 100% Epon (3h). Afterwards the probe was mounted and oriented on a steel pin and cured at 60°C for 48h.

2.1.1.4.2.3 Osmium Tetroxide + Lead Citrate Staining:

This staining protocol became the new standard, so most of the neurons presented in this study were stained as follows: Neurons were filled in the slice as described in section 2.1.1.3. GLT positive cells were identified by fluorescence (GFP). DAB Staining was performed as described above.

The cut-out neuron was washed 3x10min CB, the tissue block was hence post-fixed with 2% OsO₄ (EMS) + 1.5% K-ferricyanide for 1h and washed in de-gassed (boiled for >30min, cooled and stored in airtight tubes (Falcon)) H₂O at least three times for 10 min. Reynold's Lead was applied O/N (Reynolds, 1963). The next morning samples were washed 5 times in de-gassed H₂O, followed by dehydration using EtOH (30/40/50/60/70/80/90/96/2x100% 10min each) and 2x2min propylenoxid (PO). Subsequently, the samples were incubated infiltrated with Epon using PO:Epon 3:1 (3h), 1:1 (3h), 1:3 (O/N) and 100% Epon (3h). Hence, the sample was mounted on a steel pin and cured at 60°C for at least 48h.

Preparation of Reynold's Lead after (Lewis & Knight, 1992):

30ml de-gassed ddH₂O was filled in a 50ml tube (Falcon). 1.33g of Pb-Nitrate and 1.76g of Na-Citrate was added and mixed for 30 min on a shaker. Subsequently, 8ml of 1N NaOH was added drop wise to the solution and shaking was continued for another 15 min. Thereafter, the tube was filled up to 50 ml with de-gassed H₂O and pH was measured to be 12. Solution was always prepared freshly before use.

2.1.2 Electron Microscopy

2.1.2.1 Mounting

Since the sample was pitch-black after contrasting for EM it was important to keep the orientation of the embedded neuron. Therefore, the neuron was cut out in a trapezoid shape, so that the apical tuft was always on the long side and the basal dendrites on the short one (see Figure 2.1). A steel pin was surrounded by a rubber tube precisely fitting the pin head, resulting in a closed compartment on top of the steel pin. This compartment was filled with Epon and cured for 48h at 60°C. When the Epon was cured, the rubber tube was removed leaving a cylindrical Epon barrel. A gap was sawed into the barrel, leaving a pocket for the trapezoid shaped sample. A fresh rubber tube was put around the barrel and the gap was filled up with fresh Epon. The trapezoid sample was placed in the pocket and the pin was placed back into the oven where the Epon was cured for 48h at 60°C. This way, the sample was placed in the middle of the steel pin, stabilized, and oriented from basal (top) to tuft (bottom).

2.1.2.2 Trimming

After the Epon of the mounted sample was completely cured (>48h), the sample was taken out of the oven and shaped to a rough pyramid by a trimmer (EM Trim2, Leica) and subsequently with a diamond knife on a microtome (Ultracut S, Reichert-Jung) for the final trapezoid shape (see Figure 2.2).

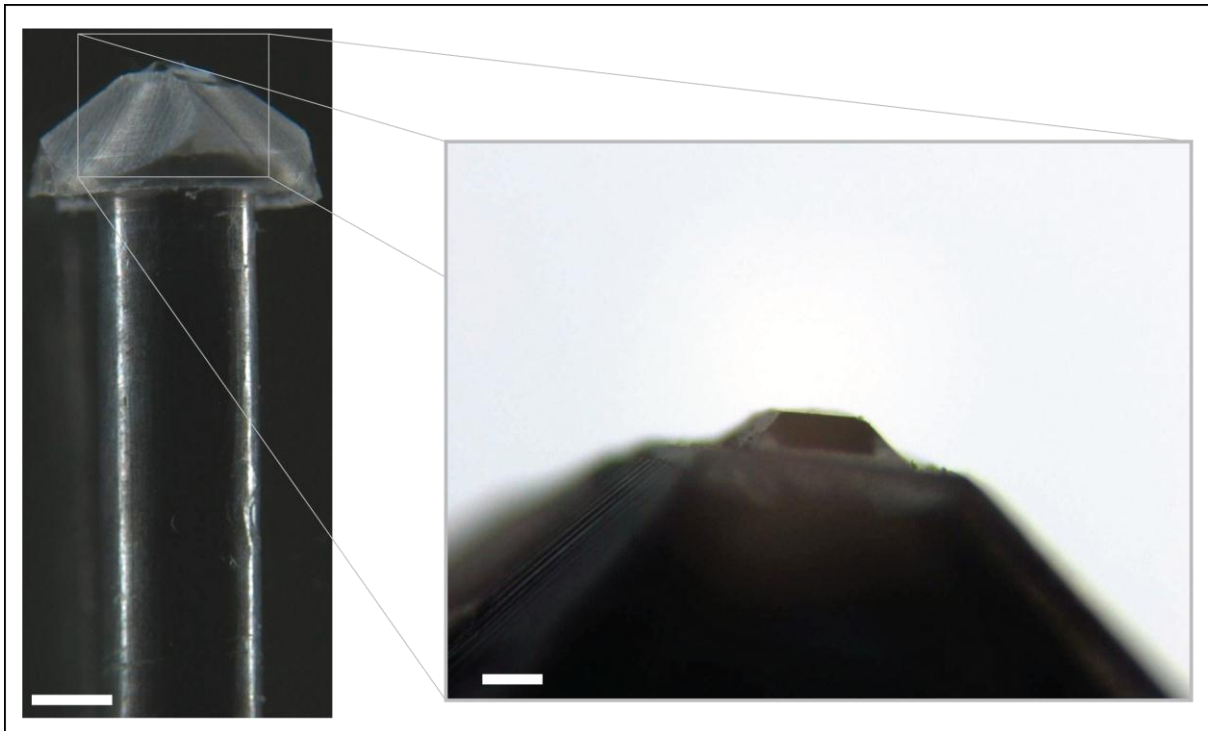


Figure 2.2: Trimmed Sample, ready to be set into the SBFSEM, Left Panel shows the steel pin with the mounted sample in the “Epon Cap”, right panel focusses the trimmed trapezoid-shaped sample containing the tissue probe (black); scale bar=1mm and 250 μ m.

2.1.2.3 Mounting the Sample in the Microscope

The trimmed probe was placed into the sample holder and the trapezoid-shaped sample was oriented concentrically in a custom monocular using two positioning screws. Following this, the sample holder was placed into the microtome of the SBFSEM and adjusted to a low

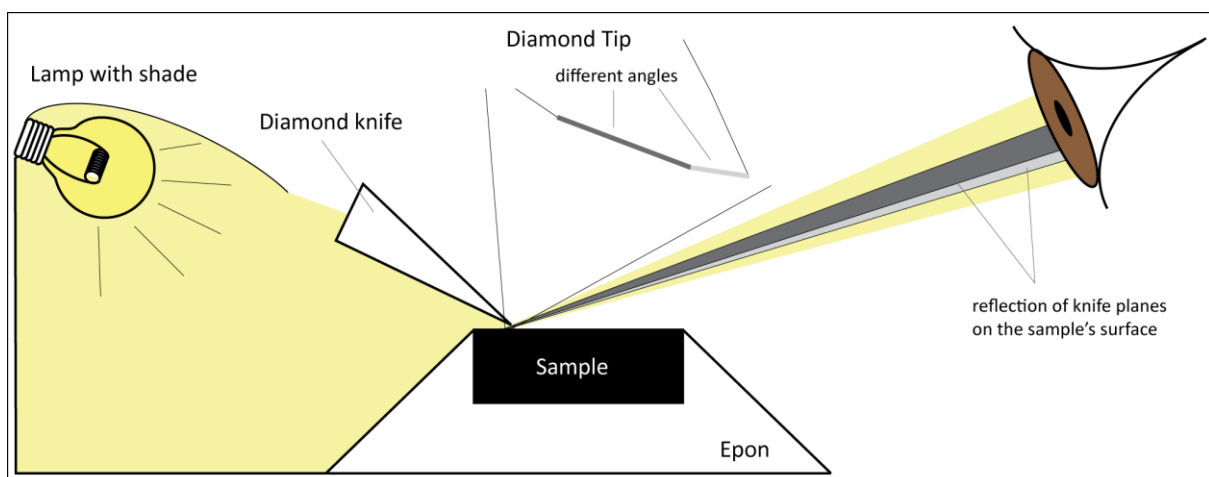


Figure 2.3: Approaching the sample towards the knife: The reflection of the diamond knife's tip is watched while approaching the sample to get as close as 1 μ m.

z-position. The knife was attached to the knife holder and the sample holder was brought closer to the diamond by a screw, watching closely through a stereo microscope (Figure 2.3). By keeping a close watch on the reflections of the knife it is possible to approach the sample down to $1\mu\text{m}$. When the knife is in close proximity, a continuous cutting cycle is started approaching the knife in 300nm steps. Continuous cutting is monitored through the stereo microscope and stopped as the whole surface gets cut. Two additional 50nm cycles are performed to polish the surface and check for cutting again. Subsequently, the chamber is closed and vacuum is applied. The needle valve for the water vapor was found to be in the right position at 2.5 turns to end up with a vacuum of 28-30mbar after ~24h.

2.1.2.4 Image Acquisition

Images from all samples were recorded at a pixel dwell time of $8\mu\text{s}$. One image had a resolution of 2048x1768 pixels. For all stacks the magnification was 6000x which resulted in a physical pixel size of $24.4\times 24.4\text{nm}$ and a field of view of $50\times 43.2\mu\text{m}$. Image spacing (cutting step) was 30nm. As an overview, after every cut, before mosaic acquisition of the high resolution images, a low magnification image was taken at a magnification of 800x or 1000x. These images were used for orientation on where in the tissue structure could be found. All images obtained by the SBFSEM were saved locally and subsequently on a network drive where they got securely saved.

2.1.3 Evaluation of the Osmium Tetroxide + Lead Citrate Staining Protocol

Evaluation of the staining protocol was performed as follows: 8 images stacks containing 10 independent neurons, all stained with the protocol described in section 2.1.1.4.2.3, were analyzed. For every neuron an image stack was chosen which contained stained dendritic structure and at least 333 images (10 μ m).

Grey values were extracted using ImageJ (National Institutes of Health, USA, <http://imagej.nih.gov/ij>): From that stack every 50th image was opened and a straight 500pixel line was manually drawn overlaying background and structure for every image in the stack. Grey values (gv) along this line were extracted and saved as text files. Thereafter, the line was imprinted on the image for visualization.

The collected gv files (holding 500 values for each image) were sequentially imported into Matlab (The Mathwork's inc.). For every measurement an auto threshold (T) was calculated: The midline of the five darkest and the five brightest values was found to be sufficient except for sample 120910F. In this sample a threshold was achieved by taking the midline of the darkest and the mean of the 200 brightest values. Values above (brighter than) T were declared background values and their mean "B". Values below T were declared signal and their mean "S". From these values the difference (|S-B|) and standard deviations of S (std(S)) and B (std(B)) were calculated. After all gv measurements of one cell were calculated for the individual slides, the average |S-B|, and standard deviations were calculated. All calculated values were exported in an Excel sheet (Microsoft Office).

Subsequently, a t-distribution was performed on the collected data using this formula:

$$t = \frac{|S - B|}{\sqrt{\sigma_S^2 + \sigma_B^2}}$$

The individual results for every slide and sample are presented in the tables present in Figures 3.12-21. A p-value was calculated for the average sample t-values using the "p-Value Calculator for a Student t-Test" from Daniel Soper (Soper, 2012). The overall averages (|S-B|, σ_S , and σ_B) were calculated taking the means of the individual samples and are summarized in Table 3.1.

2.1.4 NeuroStruct

All reconstructions were performed with the computational toolbox NeuroStruct as illustrated in Figure 2.4. The basic toolbox was published in (Lang et al, 2011b), however, some filters were adapted and the pipeline was expanded by the RV-Connectivity Filter which is described in Section 2.1.4.3. Briefly, the image stack is inverted and preprocessed by a tophat-filter to smoothen the background pixels. Thereafter the images are segmented according to a manually set parameter η , followed by a hole-filling/padding filter that fills up segmentation holes if the hole is completely surrounded by segmented foreground pixel. As a final step, the RV-Connectivity filter only accepts voxel, which are within a certain radius (R) and consist of a minimum volume (V). For every segmentation η was adapted individually, while R and V were found give good results with R=60 and V=600 for all segmentations. All filters are loaded sequentially over a shell script. Variations for the preprocessing (tophat-filter) and segmentation filter are described below. Filter programming was performed by Dr. Panos Drouvelis, while I conducted the segmentations and wrote the shell scripts. All surface reconstructions are isosurfaces created in Amira from

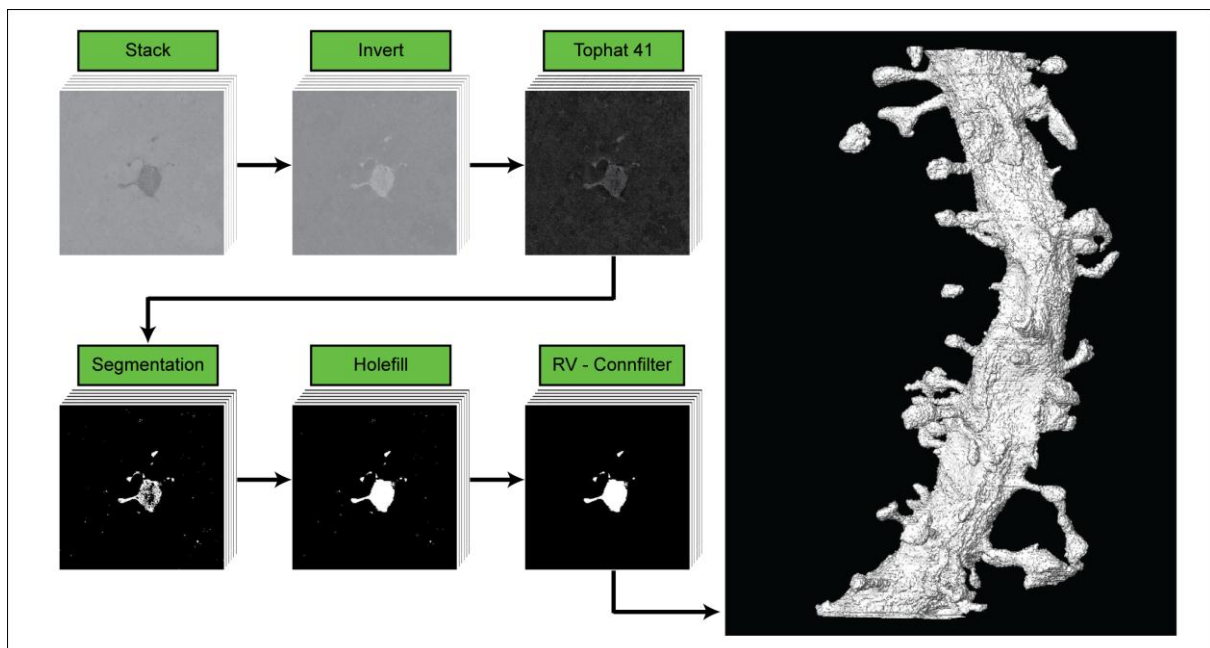


Figure 2.4: NeuroStruct: Image stacks as results for the individual filters within the pipeline are shown: Stacks (raw image stack), Invert (inverted image stack), Tophat 41 (preprocessed image stack), Segmentation, Holefill (2D holes filled), RV-Connfilter (Radius- and Volume-depending filtered image stack), Isosurface created with Amira.

the binary image stack resulting from the RV-Connectivity Filter.

2.1.4.1 Preprocessing

After inverting the image stack, a preprocessing filter was used to prepare the images for segmentation by extracting the signal plateaus of the neuronal structures in an independent fashion from their gray-value intensity level and by taking advantage of the available knowledge of their size and shape characteristics.

For this purpose a morphological “tophat by opening”-operator (Soille, 1999) was used:

$$h_B = f - \gamma_B(f)$$

where f is the inverted original image, $\gamma_B(f)$ is the morphological opening operator of the image f by a square structuring element (SE) $B = b \times b$ pixels and h_B is the resulting output image. The size of the SE depends on the size of the underlying structure to be resolved and

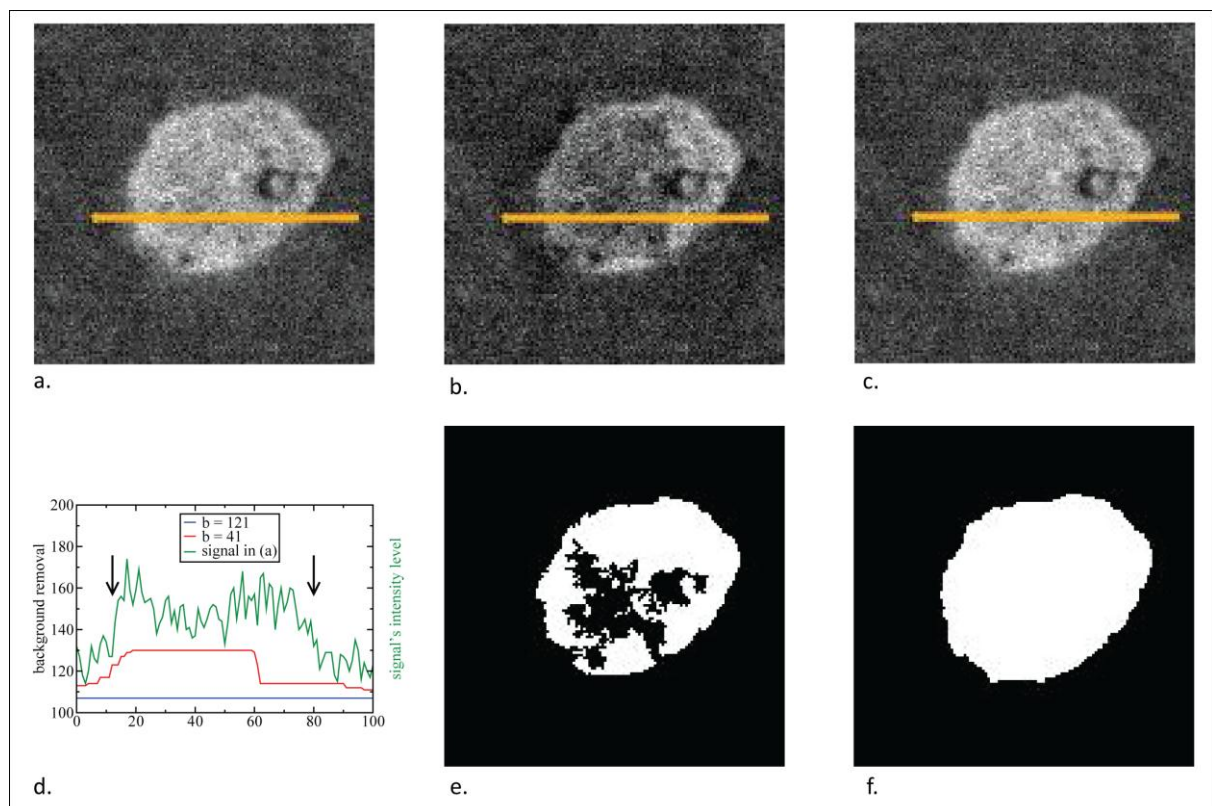


Figure 2.5: Impact of the SE on the dendritic backbone. (a.): Inverted image with dendrite cross-section, the orange line; (b.): Tophat filtered image for $b = 41$ pixels; (c.): Tophat filtered image for $b = 121$ pixels; (d.): green: original signal profile (orange line in (a.)), black arrows: dendritic signal borders, red: subtracted background for $b=41$, blue: subtracted background for $b=121$; (e.): reconstruction of (b.); (f.): reconstruction of (c.).

must be slightly larger than the size of the features that are extracted. Since dendritic backbone and fine architectures like spines differ in size, two independent tophat filterings were performed. The SE size $1 \times 1 \mu\text{m}^2$ ($b = 41$ pixels) used in (Lang et al, 2011b) was sufficiently large to extract the spine features. However, this size was not sufficient to extract the edges from the signal in the dendritic cross-section which resulted in a sometimes not properly filled dendritic backbone. Figure 2.5 shows the segmentation difference for the dendritic backbone using the SE size of $b = 41$ (b.,e.) and a larger SE of $b=121$ pixel in (c.,f.). In (d.) the signal's gray-scale value variation along the orange line in the

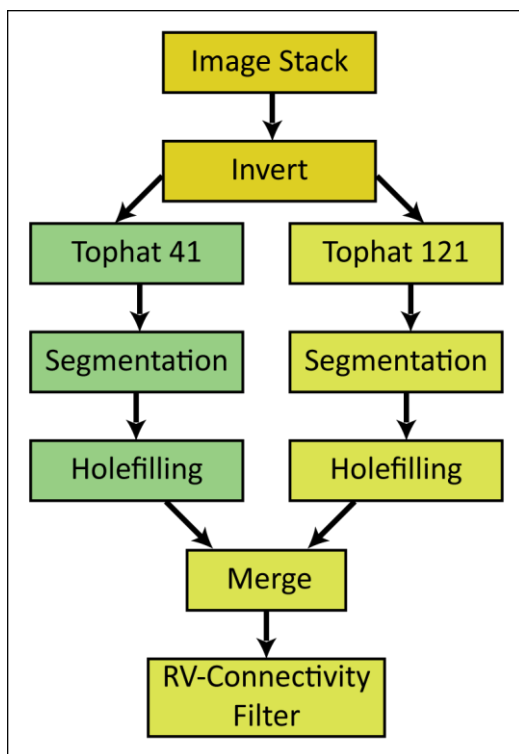


Figure 2.6: Schematic overview on the segmentation flow (shell script) of NeuroStruct used in this thesis.

original image (a.) is plotted in green. Preprocessing the dendritic backbone with a small SE ($b = 41$) led to an unevenly subtracted background varies (d., red curve) and the signal edges (black arrows) were not clearly distinguishable. This results in an incomplete segmentation of the dendritic stem (e.). By applying a tophat filter with a SE size $b = 121$ pixels ($3 \times 3 \mu\text{m}^2$) (c.), which is slightly larger than the dendritic cross-section size, the signal edges are preserved. For this SE the removed background ((d); blue curve) is constant and the dendritic stem is correctly segmented (f). To achieve the best reconstruction of all spines and the dendritic arbor, it was found to expand NeuroStruct to two reconstructions and merge them after

segmentation. The improved NeuroStruct pipeline which was used in this thesis is shown in Figure 2.6.

2.1.4.2 Segmentation

The used 3D non-linear operator for the extraction of the foreground neuronal structure is a reduced version of the operator described in (Lang et al, 2011b). It is based on a global user-defined gray-level threshold value η and an *ad hoc* local threshold criterion tailored on the voxel's neighborhood. The foreground voxels obey the relationship:

$$f_{foreground}(v) = (f(v) \geq \eta) \wedge (\exists v' \in N_{18}(v) | f(v') > M(v))$$

where $f(v)$ is the gray-level value of the voxel $v(i,j,k)$ with coordinates i,j on image k , $M(v)$ is the mean value of the gray-level values of the voxels defined in a neighborhood of the addressed voxel v with dimensions $15 \times 15 \times 3$ (width \times height \times axial direction). The neighborhood extends in three images; this neighborhood is shown in Figure 2.7(a.) for a single image. Voxels are categorized as foreground candidates by satisfying two criteria: firstly, if their gray-level value is larger than or equal to η and, secondly, based on the local threshold criterion, that at least one of their $N_{18}(v)$ neighbors (b.) has a gray-level value larger than the mean gray-level value $M(v)$. If both conditions are fulfilled, the voxel is foreground, otherwise it is background. In order to obtain a proper reconstruction of the neuronal structure, the global parameter η was chosen individually for each segmentation.

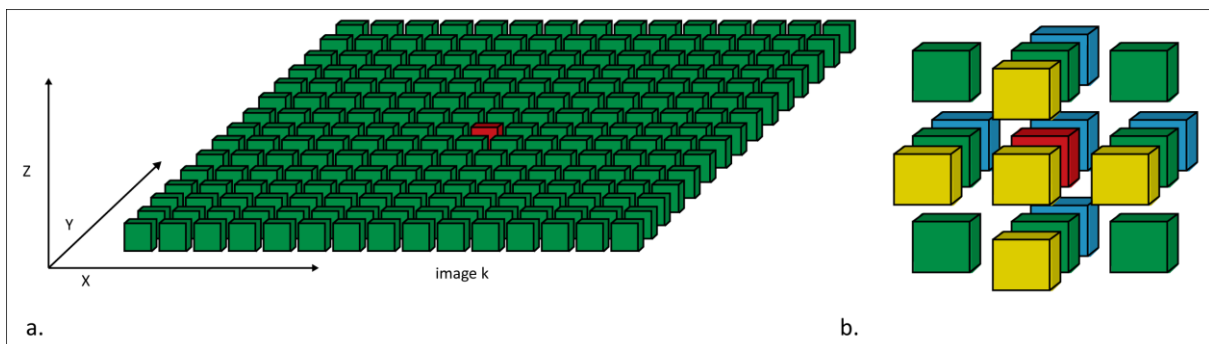


Figure 2.7: Neighborhoods used in the segmentation algorithm; (a.): Neighborhood 15×15 defined on an arbitrary image k . The neighborhood $15 \times 15 \times 3$ involving the images $k-1$, k and $k+1$ is used for the calculation of the mean gray-level value of the foreground candidate voxel located at the center of the neighborhood (red color); (b.): Neighborhood N_{18} used to examine if any of these voxels has a greater value than the mean gray-level value calculated on the $15 \times 15 \times 3$ neighborhood.

2.1.4.3 Expansion of NeuroStruct: the RV-Connectivity-Filter

In some cases, spine necks cannot be segmented. This might be due to an incomplete staining of the thin connection or result from the neck being so thin, that its diameter cannot be resolved by the 25x25x30nm voxel resolution. For this reason, a filter had to be implemented that discriminates artifacts within close proximity of the dendrite and spine heads that are not connected, but which belong to the neuronal structure. The filter is set after the holes in the segmentations are padded. In this step the segmented voxels are classified into three categories based on their three-dimensional (3D) connectivity properties: (i) largest 3D connected components, (ii) 3D connected components residing within a two-dimensional (2D) radius 'R' from the largest components and possessing a voxel size greater than 'V' and, (iii) the rest of the 3D connected objects. This algorithm is based on a transitive vertex graph of a $N_6(v)$ -neighborhood of voxel v .

(i) Filtering of the largest 3D connected components

The images of the data stack are processed image-wise and the connectivity properties are initially defined at the image level k . For every foreground voxel, an image-local ID is assigned based on whether the previously visited voxel-neighbors (Figure 2.8(a.)) are present in the background or foreground. If one neighbor is in the foreground, the current visited voxel receives the ID of that neighbor. If both neighbors have a previously assigned ID, then a "local image container" (1D temporary vector, keeping track of the connected IDs) is updated. After the connections are identified, the voxels are updated with a uniquely assigned ID based on the "local image connectivity container". For every processed image k (Figure 2.8(a.)), (except for the first one which is the image with the initial IDs) the algorithm checks if every currently visited foreground voxel is neighboring a foreground voxel from the previous image $k-1$ (Figure 2.8(a.)). If so, a "global connectivity container" for the 3D image space is updated, that keeps track of which foreground voxels are connected. In the end, the image-local assigned IDs are updated with the ones from the global 3D image-space container. For every step, a single binary image is processed at a time, which makes the filter independent of the size of the data. The *largest 3D components* (in terms of voxel count) are defined on the basis of how many voxels are assigned to every ID. These IDs are earmarked in a separate container. This step can be summarized into the pseudocode below:

- 1 assign unique IDs to the connected voxels (N_4 -Neighborhood) in the first image h_0
- 2 initialize global connectivity container
- 3 **for** every image h_k
- 4 {
- 5 Assign IDs to the image h_k
- 6 **for** every pixel of the image h_k
- 7 {
- 8 **if** the visited voxel is neighboring the one from the previous image h_{k-1}
- 9 update the global connectivity container
- 10 }
- 11 }
- 12 go through the image stack again and assign unique IDs from the global connectivity container (connected voxels on a N_6 -Neighborhood)
- 13 count the voxels of every ID and store the IDs of the largest connected components

(ii) Filtering of the components in the proximity of the largest 3D connected components

During this step, the whole image stack is processed again image-wise and the remaining (unmarked) voxels (v_x) are tested under two conditions. The first condition is $\|v_x - v_{\text{marked}}\|_k \leq R$, where $\|\cdot\|_k$ is the Euclidean distance on a fixed image k , rounded to the nearest integer of larger or equal value (Soille, 1999) and R is a given integer input parameter. In Figure 2.8(b.) the criterion used to declare objects in the vicinity of the marked structures in the image-local space is illustrated. In this figure it is also shown how this criterion can be extended to include a Euclidean distance R_{3D} defined in the 3D image space, by exploiting the vector representation of the voxel-IDs. The second condition is fulfilled if the 3D object corresponding to this ID takes up a volume larger than $V(v_x) > V$ (input parameter). The volume in the binary image space is defined as the number of the foreground connected voxels. If both conditions are met, these IDs are marked. The final step processes the whole stack for a second time image-wise and all voxels of which IDs were marked - largest 3D connected components and 3D connected components in their vicinity depending on R and V – are declared as foreground voxels. The number of largest components (category (i)), R and V are variables set by the user.

After the connectivity analysis, the segmented objects are categorized into the three categories (Figure 2.8(c.)). The first category corresponds to the identified dendritic branches and the attached spines. Voxels of the second category belong to possible spines which are not attached but in local proximity of the dendritic backbone. The third category represents false, unwanted objects from staining and segmentation artifacts that are excluded after the application of the filter. The accepted voxels are subsequently written into .tif images.

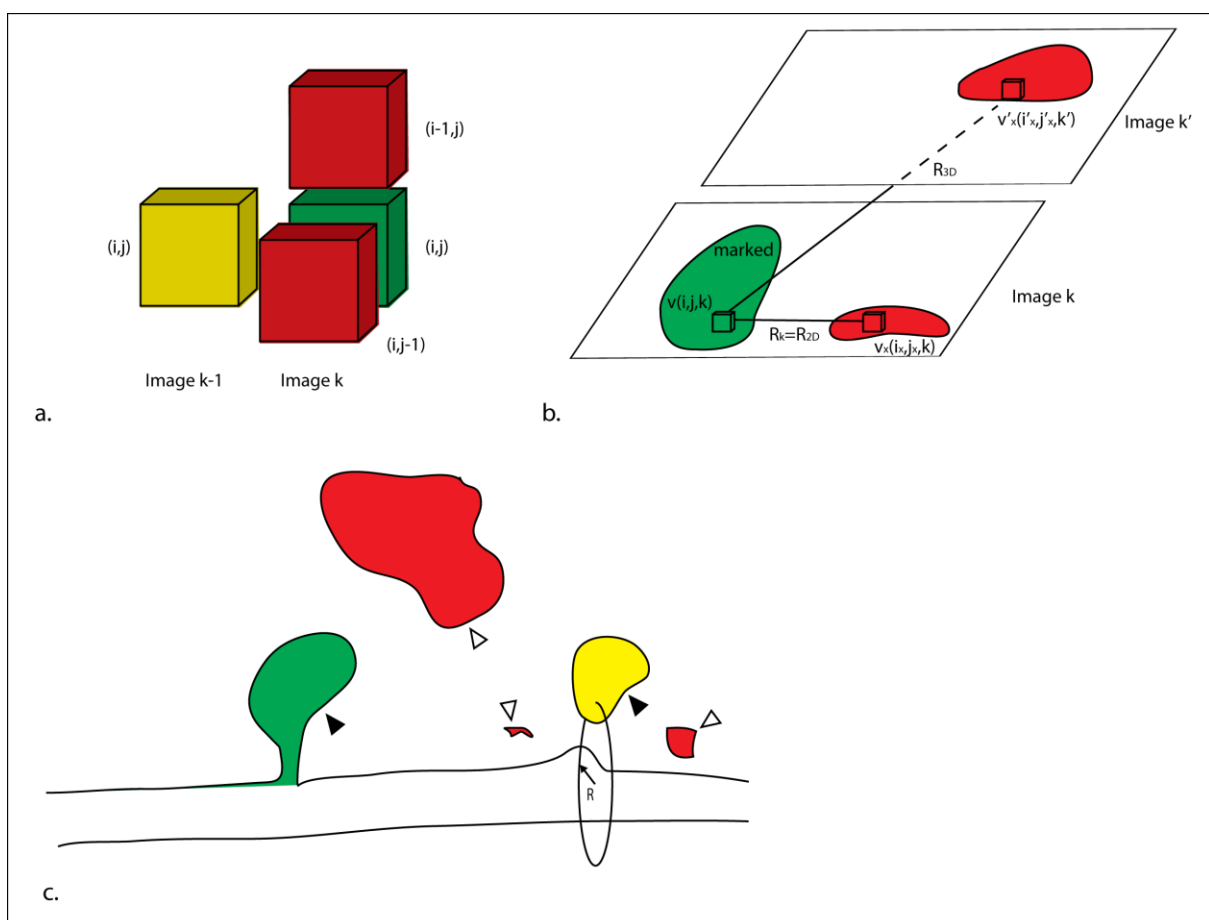


Figure 2.8: Neighborhoods used in the connectivity filter; (a.): Neighborhood N3 used by the connectivity filter. The neighbors within the same image k (red color) define the connectivity locally at the binary image, the neighbor of the previous image k-1 is used for the 3D connectivity of the binary image stack; (b.): Illustration of the radius criterion used to declare 3D-connected objects in the vicinity of the marked structures. In this work the radius criterion R is based on a 2D Euclidean norm defined on the image-local space k. An extension of this criterion in the 3D image space is shown. Individual voxels are magnified for visualization purposes; (c.): Schemes of the three designated object categories: identified dendritic branches and attached spines (green); objects within a distance of maximal R and a voxel volume of at least V (yellow); objects with a distance larger than R or a voxel volume smaller than V (red). Accepted objects and rejected objects are marked with filled and hollow arrowheads, respectively.

2.1.4.4 NeuroStruct Validation Metrics

2.1.4.4.1 Object Space

For definition purposes we generally describe the validation by using the initial letter X for the tracing that was validated against the reference tracing (RT). The validation metrics are defined in two spaces: 3D object space by visual investigation of the 3D reconstructions and 3D image space by using the binary images of the tracings. In the 3D object space we distinguished three types of foreground objects:

I. True objects: useful information, i.e. dendrites and spines (see Figure 2.9(a.), filled arrowheads).

II. False objects: unintentionally identified objects, usually stained artifacts (see Figure 2.9(a.), hollow arrowheads)

III. Loops: toroidal shapes formed in the 3D space

False objects and loops were both defined as artifact-objects. Objects in general were distinguished into: Positive (objects of X coinciding with RT) and Negative (objects of X not coincide with RT). Thus, positive and negative objects of X were always defined by RT. Tracings X and RT were allowed to have both true and artifact-objects. As true objects of X (RT “Positive“ and RT “Negative“ true objects) form a homeomorphic set distinguishing between the two was not necessary. This, however, was not the case for artifact-objects as illustrated in Figure 2.9(a.). Two arbitrary tracings $X_{(1)}$ and $X_{(2)}$ could not have more true objects than RT as the number of true objects was defined there. However, the corresponding false objects of tracings $X_{(1)}$ and $X_{(2)}$ could arbitrarily vary. Because artifacts were present in all tracings, two different tracings ($X_{(1)}$, $X_{(2)}$) obey the following relationship:

$$\{X_{true}^{(1)}(RT_{positive})\} \cup \{X_{true}^{(1)}(RT_{negative})\} = \{X_{true}^{(2)}(RT_{positive})\} \cup \{X_{true}^{(2)}(RT_{negative})\} = \{RT_{true}\}.$$

The following relationship holds for the artifacts:

$$\begin{aligned} & \{X_{\text{artifact}}^{(1)}(RT_{\text{positive}})\} \cup \{X_{\text{artifact}}^{(1)}(RT_{\text{negative}})\} \neq \\ & \{X_{\text{artifact}}^{(2)}(RT_{\text{positive}})\} \cup \{X_{\text{artifact}}^{(2)}(RT_{\text{negative}})\} \neq \{RT_{\text{artifact}}\}, \end{aligned}$$

where $\{X_{\text{true}}^{(1)}(RT_{\text{positive}})\}$ is the set of the true RT positive objects of dataset $X^{(1)}$, and $\{RT_{\text{true}}\}$ is the set of the true objects defined by default for RT.

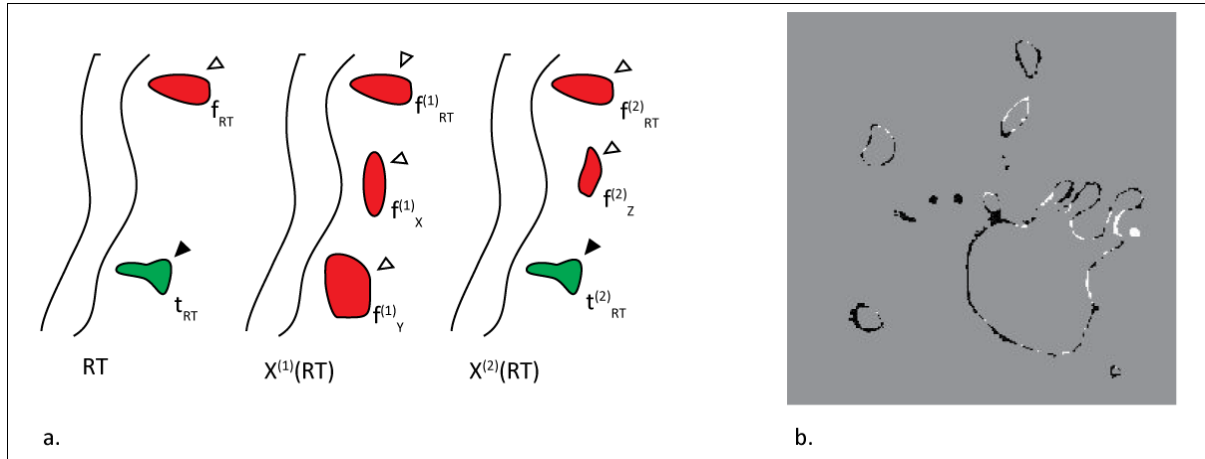


Figure 2.9: (a.): Exemplary object space of reconstructions R , $X(1)$ and $X(2)$. True objects (green color) of $X(1)$ and $X(2)$ exist either in the R space or not, whereas their number of false objects (red color) may vary, though. (b.): Part of a slide ($z = 400$) showing the R2 positive (white color) and R2 negative (black color) pixels of the automated tracing NST. The background has a neutral gray-scale value 128.

2.1.4.4.2 Image Space

The 3D image space was defined as the number of 3D connected foreground voxels of identified structures. We defined the excess voxel operator of two binary images A with respect to B , by applying an image subtraction operation defined as:

$$A - B \begin{cases} 255, & \text{if } A[i] > B[i] \\ 0, & \text{else} \end{cases}$$

at which $A[i]$ is the pixel i of the image A . This operation shows the excess of the voxels in A with respect to B without considering any excess voxels of B in terms of A . The subtraction operator $(RT - X)$ defines the $X(RT)$ Positive voxels, whereas $(X - RT)$ outputs the $X(RT)$ Negative voxels. In Figure 2.9(b.) the R2 positive and R2 negative voxels of one section of the

dataset NSt are presented in white and black color, respectively. The voxel volume of the false objects was estimated by measuring the voxel difference between the manually or computationally traced data and the data acquired after the application of the RV-Connectivity Filter for $R = 60$ and $V = 600$ voxels (these are the parameters used for the computation of the NSt dataset).

2.1.5 Spine Pruning

The RV-Connectivity Filter was modified as a structure separator to save the largest components in separate .Tiff stacks. The spine pruning was performed by an algorithm that identifies spines and cuts them off at their root at the dendritic backbone. At a first run through the algorithm scans separates between spines and dendrites based on a 2D criterion, defined on the processed image. This criterion defines 2D connectivity based on a

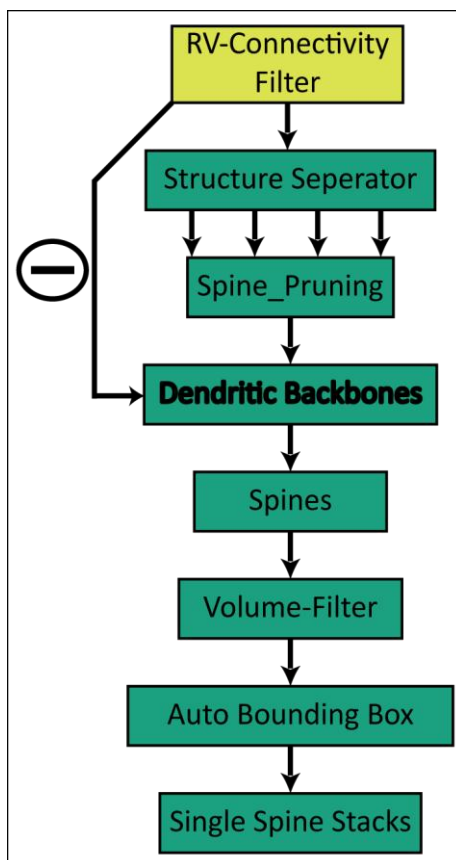


Figure 2.10: Flowchart of the spine pruning expansion in NeuroStruct.

$N4(v)$ neighborhood and marks the largest connected component as dendritic backbone. Subsequently, the algorithm scans iteratively through the image stack in order to connect pieces of foreground voxels that are either direct neighbors (this means top- or bottom-) or within the dendritic border of the previous dendritic image. The working method used is that at the first iteration defines the dendritic border of the previous dendritic image, whereas all the rest of the iterations scan for direct spine-neighbors. 10 iterations were sufficient to export the pruned backbone and the cut-off spines as .Tiff stacks in different folders. However, the exported cut-off spines were found to be incomplete as non-connected spine heads were left out of the segmented spines. Therefore, the pipeline was adjusted so that the pruned dendritic backbone was subtracted on a pixel level from the whole RV-

Connectivity-Filer output files. This way, the spines end up separated from each other. To clear the images from by the subtraction created binary noise, the stacks were volume filtered to only remain volumes larger than 1500 voxels. Subsequently, the individual volume clusters were cropped and saved separately in .Tiff stacks according to their bounding box. This way every assumed spine structure is saved in an individual .Tiff stack for further analysis.

2.1.6 Spine Density

When the Neuron TK100909A1 was readily segmented, the RV-Connectivity Filter output .Tiff stacks were opened individually in Amira. An isosurface was created. Onto the isosurface, the individual spines were marked by a landmark, on the spine neck's origin. After every spine was clicked, overlapping reconstructions were loaded and checked for overlaying landmarks; doubles were deleted and the landmark file was saved as an .ascii file holding the local coordinates of every spine within a stack. Subsequently, all 184 landmark files were loaded in Amira and each one was aligned with the corresponding pre-aligned voxelcloud file of the stack reconstructions. The shifted coordinates were applied to the landmarks and the aligned landmarks were saved as an .ascii file holding the global coordinates of every spine within a stack. Subsequently, All 184 global landmarks files were merged into one .ascii file holding the global coordinates for all 6672 spine landmarks. This file was imported into Matlab. The landmarks were binned, according to their z-coordinate, in 5 μ m bins and in the manually determined layers: 0-85 μ m (L1), 86-185 μ m (L2), 186-345 μ m (L3), 346-465 μ m (L4), 466-520 μ m (L5A), and 521- 615 μ m (L5B), respectively.

2.2 Material

2.2.1 Buffers

Standard Buffers for fixation, DAB staining and EM contrasting were based on 0.1mM Na-Cacodylate and 0.1 mM Phosphatebuffer.

For all buffers and solutions the pH was adjusted to 7.3 (HCl/NaOH) and the osmolarity to 320mOsm (sucrose).

Slice Solution		Storage/ Perfusion Solution		Intracellular Solution [mM]	
NaCl	125	NaCl	125	K-Gluconate	135
NaHCO ₃	25	NaHCO ₃	25	Hepes	10
KCL	2,5	KCL	2,5	Phosphocreatine-Na ₂	10
NaH ₂ PO ₄ *1H ₂ O	1,25	NaH ₂ PO ₄ *1H ₂ O	1,25	KCl	4
MgCl ₂ *6H ₂ O	5	MgCl ₂ *6H ₂ O	1	ATP-Mg-salt	4
Myo-Inositol	3	Glucose	25	Guanosintriphosphate	0,3
Na-Pyruvat	2	CaCl ₂	2	add Biocytin 2-3 mg/ml	
Ascorbic acid	0,4			abb 100µM Alexa594 (optional)	
CaCl ₂	1				
add 4.5g Glucose/l					

Epon	
	[ml]
Glycid Ether 100	10
2-Dodecenylsuccinic acid anhydride	4.5
Methylnadic anhydrite	6
Benzyl dimethylamine	0.6

2.2.2 Chemicals

Name	Company
NaCl	AnalaR NORMAPUR
NaHCO ₃	Merck
KCL	Merck

NaH₂PO₄	Merck
MgCl₂	Invitrogen
Myo-Inositol	Fluka
Na-Pyruvat	Sigma
Ascorbic acid	Caelo
CaCl₂	Merck
Glucose	Merck
K-Gluconate	Sigma
Hepes	Biomol
Phosphocreatine-Na₂	Sigma
ATP-Mg	Sigma
GTP	Sigma
Biocytin	Sigma
Alexa Fluor[®] 594 hydrazide, Na-salt for microinjection	Invitrogen
Na₂HPO₄	Merck
Na-Cacodylate	Serva
DAB	Serva
Poly-D-lysine hydrobromide	Sigma
round coverglasses 15mm	Menzel
Sucrose	Roth
p-Formaldehyd	Merck
Glutaraldehyde, 25% EM grade	Polyscience
TritonX-100	Merck
Isofluran	cp-pharma
NaOH (for Reynold's Lead)	Sigma
Osmium Tetroxide 4% Aqueous Solution	EMS
Lead(III) citrate Trihydrate	Fluka
Uranyl Acetate	EMS
Glycid Ether 100	Serva
2-Dodecenylsuccinic acid anhydride	Serva
Methylnadic anhydrite	Serva
Benzyl dimethylamine	Serva
Vectastain ABC Kit „Elite“, PK-6100	Vectastain
Ethanol absolut (for dehydration)	Riedel-DeHaen
H₂O₂	Merck
3ml glass vials	VWR
1.5ml and 2 ml	Eppendorf
15ml and 50 ml	Falcon
25-well plate	Costar

2.2.3 Light microscopy

2.2.3.1 Patch Setup

Type	Comment	Name	Company
Imaging			
Microscope		BX51WI	Olympus
Objective		LUMPlanFI 40x/NA=0.8	Olympus
Objective		PlanC N 4x/NA=0.1	Olympus
Camera	IR-DIC	IR-CCD Imaging	PCO
Camera	Fluorescence	CoolSNAP HQ2	Photometrics
Light source	Fluorescence	precisExite (490nm/595nm)	CoolLed
Filter	Green	U-N421020 HQ:GFP NB	Chroma
Filter	Green + DIC	U-MGFP/XL	Olympus
Filter	Red	U-N41027 CAL CRIM	Chroma
Filter	DIC	U-MDICT3	Olympus
Motor Controls			
X/Y Table		SM-II	Luigs&Neumann
Pipette motors		SM-II	Luigs&Neumann
Periphery			
Oscilloscope		HM303-6	Hameg
Amplifier		Axopatch 200B	Axon Instruments
Computer		Optiplex 780	Dell
Software	For Images	VisiView	Visitron
Miscellaneous			
Puller	For Pipettes	Model P-97	Sutter Instruments Co.
Slicer	For acute slices	HM250V	Microm
Bo-glasscapillaries with filament (Hilgenberg)			
length [mm]	Outside \varnothing [mm]	Wall thickness [mm]	
75	2	0.5	

2.2.3.2 Neuromorph Setup

Type	Comment	Name	Company
Imaging			
Microscope		BX51	Olympus
Objective		UPlanFL N 40x/NA:1.3 Oil	Olympus
Camera		QICAM	Qimaging
Motor Controls			
X/Y Table			Märzhäuser
Z-stepper			Märzhäuser
Miscellaneous			
Computer		Optiplex 780	Dell
Software	For Images	Surveyer	OASIS

2.2.4 Electron microscopy

2.2.4.1 SBFSEM

The SBFSEM used in this thesis was an FEI Quanta FEG200 with a custom door (Microtome) and solid state BSE detector. The system was published in (Denk & Horstmann, 2004).

2.2.4.2 SEM

The additional SEM images used for contrast screening in chapter 2.1.3.1 were acquired by a Hitachi S-3400N.

2.2.4.3 TEM

The TEM images used for contrast screening in chapter 2.1.3.1 were acquired by a JEOL JEM-1230. Thickness of thin sections was approximately 70nm.

Chapter 3 Results

The aim of this study was to use SBFSEM technique to reliably obtain quantitative morphological information of one specific, and previously identified, neuron with nanoscale resolution. Labeling single neurons with biocytin through passive diffusion of intracellular solution from a patch pipette, is a long established method and was therefore used to also label the cells for EM. As mentioned in section 1.4, the staining protocol present at the beginning of this thesis was unacceptable for scanning very large datasets of mm^3 , as many artifacts interfere with the reconstruction of the filled neuron in relatively small μm^3 volumes. In addition to the development and validation of an adequate staining protocol, the reconstruction software had to be adjusted, extended and validated to guarantee for a reliable output of data. In the end, data from ten individual neurons could be obtained and even one entire L5B neuron was reconstructed at a voxelsize of $25 \times 25 \times 30 \text{nm}$ from a one teravoxel dataset.

3.1 Development of a Staining Protocol for Single Biocytin-filled Neurons for SBFSEM

The first part of this thesis describes how a staining protocol, primarily for the Serial Block Face-Scanning Electron Microscopy (SBFSEM), was developed, established, quantified, and optimized though large and reliable data could be produced. For the approach to visualize spines of one specific neuron on an ultra-structural level, the single neuron of interest had to be labeled first. As a reliable and commonly used method, whole-cell filling of a neuron via a patch pipette was chosen. The neuron is patched and filled in an acute slice with a tracer (biocytin) and the fixed slice is then stained with di-aminobenzidine (DAB). The DAB polymer is a brown and opaque precipitate, which makes it suitable for light microscopy (LM), however it provides only poor contrast in electron microscopy (EM), due to its lack of electron density. EM contrast is achieved by labeling structures with electron dense heavy metals such as gold, silver, osmium, uranium or lead. Whilst some metals are usually applied

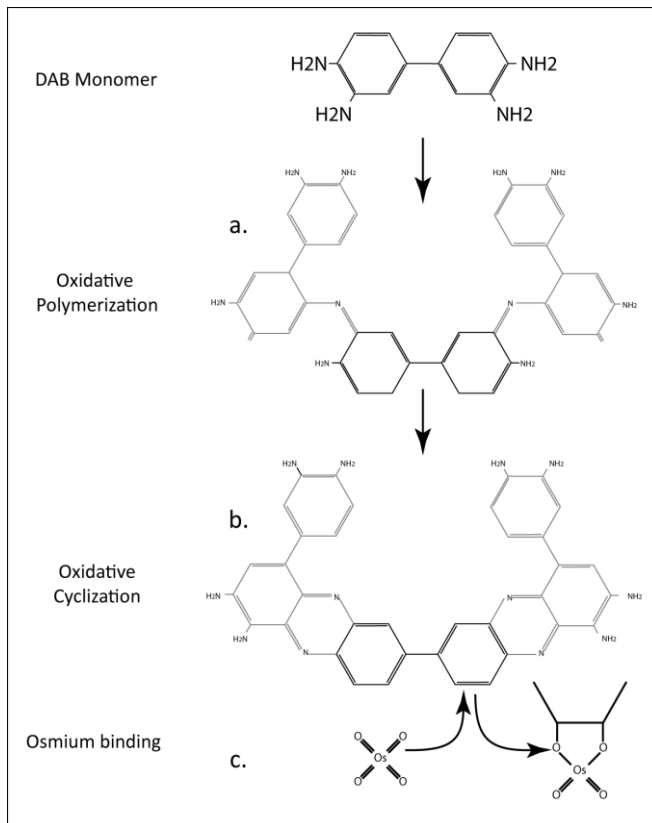


Figure 3.1: Sketch of the oxidative polymerization to indamines; (a.): and cyclization to phenazines; (b.): of DAB. Both reactions are driven by O^- which is facilitated by the addition of H_2O_2 . The reactions are accelerated by the horseradish peroxidase (HRP) which was bound to the intracellular tracer biotin via conjugation (see Materials and Methods); (c.): describes the OsO_4 fixation of double bindings (modified from (Seligman et al, 1968; Seligman et al, 1966)).

after sectioning of the embedded tissue block, this is not possible for SBFSEM since the surface of the block is imaged before discarding the “slice”. Thus, all contrasting methods need to be carried out *en bloc*. The DAB polymer bears many C=C double bonds in its indamine and phenazine ring system which are preferable targets for the heavy metal osmium tetroxide (OsO_4) (Figure 3.1 and (Seligman et al, 1968)). As OsO_4 targets all double bonds in the tissue, it concurrently binds to double bonds in proteins within the neuropil. The aim was to optimize the EM staining protocol so that (i) the filled neuron shows a significantly higher contrast than the surrounding neuropil (increasing the signal to noise) and (ii) the number of interfering artifacts (e.g. charging, metal precipitates) and

unwanted structures (e.g. myelin or capillaries) are reduced to a minimum to make the subsequent automated segmentation easier.

3.1.1 The Selection of usable Cells for SBFSEM in Light Microscopy

Developing and establishing a specific staining protocol for single filled cells for electron microscopy (EM) is tricky and laborious as every condition that is changed in the protocol, requires at least one filled neuron. To compare the results of different EM stainings and to rule out differences due to earlier staining steps, it is essential to start off with a comparable

sample quality. The decision as to whether or not a cell was taken for EM contrasting was made based on the quality of the DAB staining. However, a neuron could already be excluded if the filling itself had failed.

3.1.1.1 Monitoring the Filling of the Neuron

The diffusion speed of biocytin is rapid (2mm in about 10 minutes (Conn et al, 1999)). Thus, 15 minutes were more than sufficient to fill the entire dendritic tree of a L5B neuron. For monitoring the diffusion of the intracellular solution within the neuron while the slice was in the patch setup, a small amount of fluorophore Alexa594 was added to the intracellular solution. In this way it was possible to check for a proper filling whilst the pipette is still attached (Figure 3.2). The soma was visible after 2-3 minutes and the apical dendrite, if visible through the tissue, became visible after roughly 5-10 minutes. Although, due to the cutting angle, the apical tuft (a.) was not visible in all cells, however, the cell body and basal dendrites gave a good indication as to whether the intracellular solution was diffusing well (b.). Cells that did not show a satisfying fill (c.) resulted in an equally unsatisfying staining result for the intracellular tracer biocytin and were discarded. Note that due to the slicing angle the axon was usually cut off and will not be regarded in this study.

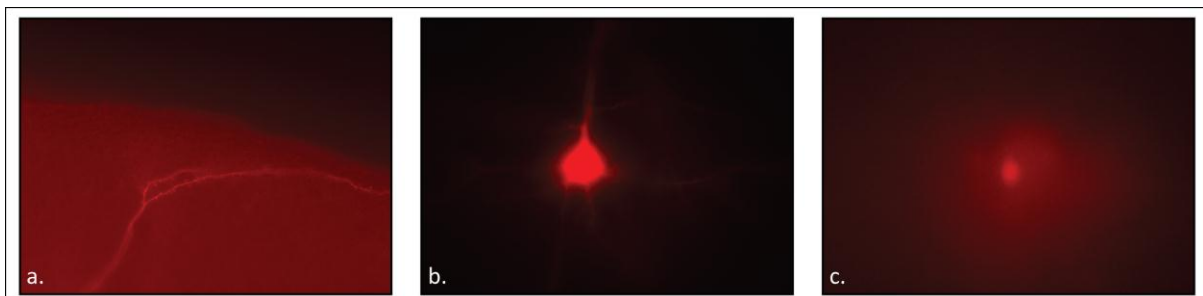


Figure 3.2: Fluorescence of Alexa 594 to monitor the diffusion of the intracellular solution in the patched neurons; (a.): apical dendrite, spines are well visible; (b.): soma and basal dendrites. The basal dendrites appear dimmer because the very bright soma outshines the rest of the frame; (c.): dim soma and residual pipette solution is visible in the extracellular space; this might result in a dark background smear after the DAB staining.

3.1.1.2 DAB Staining

The DAB staining is the final quality check of the stained neuron before contrasting for EM. Comparable qualities are crucial before continuing with the EM staining for several reasons. Firstly, neurons that are diversely stained might result in irregular EM contrast and secondly, artifacts due to extracellular DAB or ghost-cells (cells that unintentionally took up biocytin) could interfere with the eventual segmentation of the structure. Every slice was analyzed under a brightfield microscope to verify slice continuation or elimination. Figure 3.3 compares minimum z-projections of DAB stained neurons that were either discarded (a.-d.) or retained (e.) for EM contrasting. The reasons for excluding neurons are numerous: no intense filling (a.), extracellular DAB which is visible as a dark smear background surrounding the soma (marked with a small star in b.-d.), ghost-cells visible as apical dendrites (b.) or cell bodies (c.), or a cut-off apical dendrite (scissor in d.). A clean DAB staining without the aforementioned flaws is shown in (e.). This quality reflects the standard for use of EM contrasting. If only one neuron is scanned at any one time in the SBFSEM, a lot of additional unstained volume is scanned. Therefore, in later attempts, up to three cells were filled in

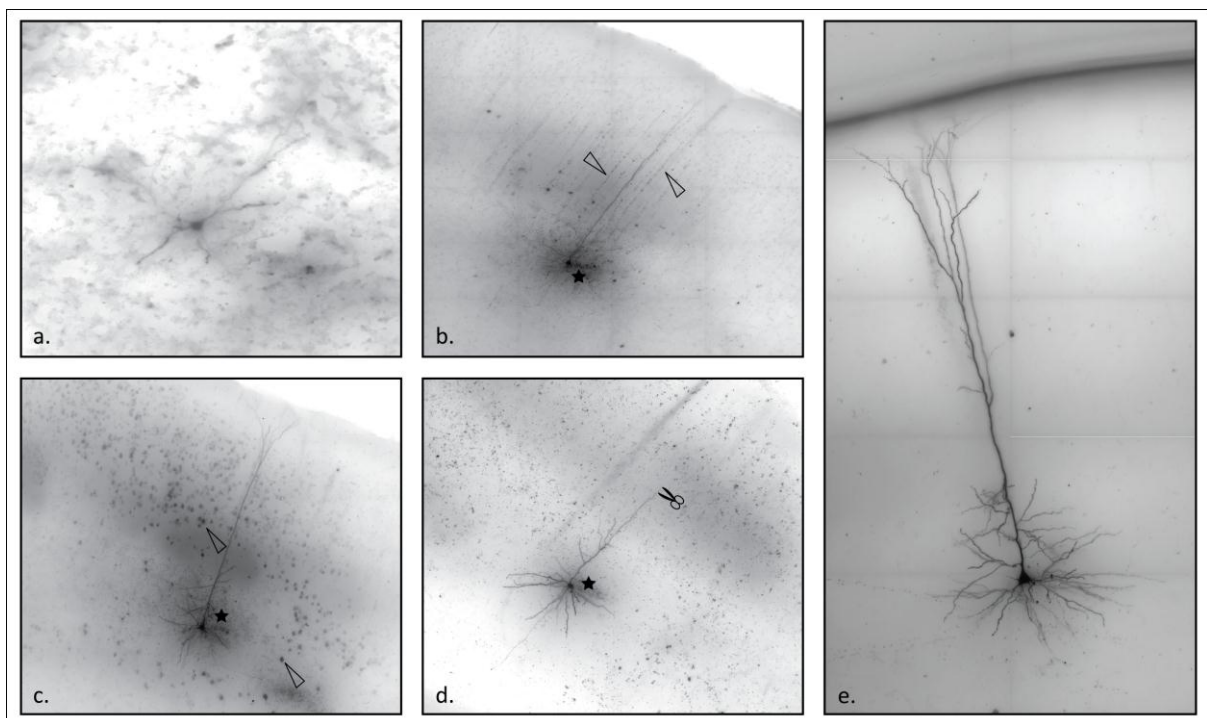


Figure 3.3: Examples for characteristics which led to elimination of DAB stained cells (a.-d.) and a cell that qualified for EM contrasting (e.); small star=background, arrowhead=ghost cells; scissor=cut apical dendrite.

close proximity of each other. To avoid increasing the scanning area the cells must be very close to or on the same longitudinal axis as the apical dendrite. Filling multiple adjacent neurons increases the risk of introducing artifacts. Only if all cells were suitably filled with no background smear present, was the sample used for further contrasting.

3.1.2 Screening for a Proper Staining in the SBFSEM

After the selection of appropriate samples for the subsequently continued heavy metal staining was made, cells were cut out, block-stained and mounted on a steel pin as described in Section 2 (Materials & Methods). The mounted sample was placed into the SBFSEM and image stacks were recorded. Further quality characteristics such as contrast, slice ability, staining of unwanted structures and charging of the sample were analyzed. The protocol is designed to specifically increase the contrast of the previous filled and stained neuronal structure. Therefore, the term artifact is used for any undesired structure (e.g. myelin, astrocytes or other large endogenous structures). Figure 3.4 illustrates examples of poor quality images, such as weak contrast (a.), artifacts (b.), charging (c.), and one cross section with a desirable staining quality (d.). A sample can have decent contrast but too strong of a charge. This might be due to a shortage of overall metals or an excess of energy of the electron beam. Therefore, the electrons cannot be discharged from the sample which consequently results in black areas on the image (a.) and (c.). If the contrast quality of a staining was sufficient to segment the structure from the dataset, a reconstruction using NeuroStruct was computed (Lang et al, 2011b). This reconstruction was further analyzed visually in 3D using Amira and the quality of neuronal structures like dendritic backbone and dendritic spines were judged subjectively (Figure 3.5). The reconstruction analysis is pivotal since the visual assessment is the primary validation of the stained structure. The main criteria were the ease of the segmentation (choosing adequate parameters, number of re-dos, etc.) and the consistency of the surface or how many structures like spine necks were missing. Because only one distinct whole single neuron is filled with biocytin and stained, a spine head that has no connection must belong to that particular neuron. Dendritic spine necks can be absent from segmentation due to two reasons: (i) lack of resolution (voxelsize:

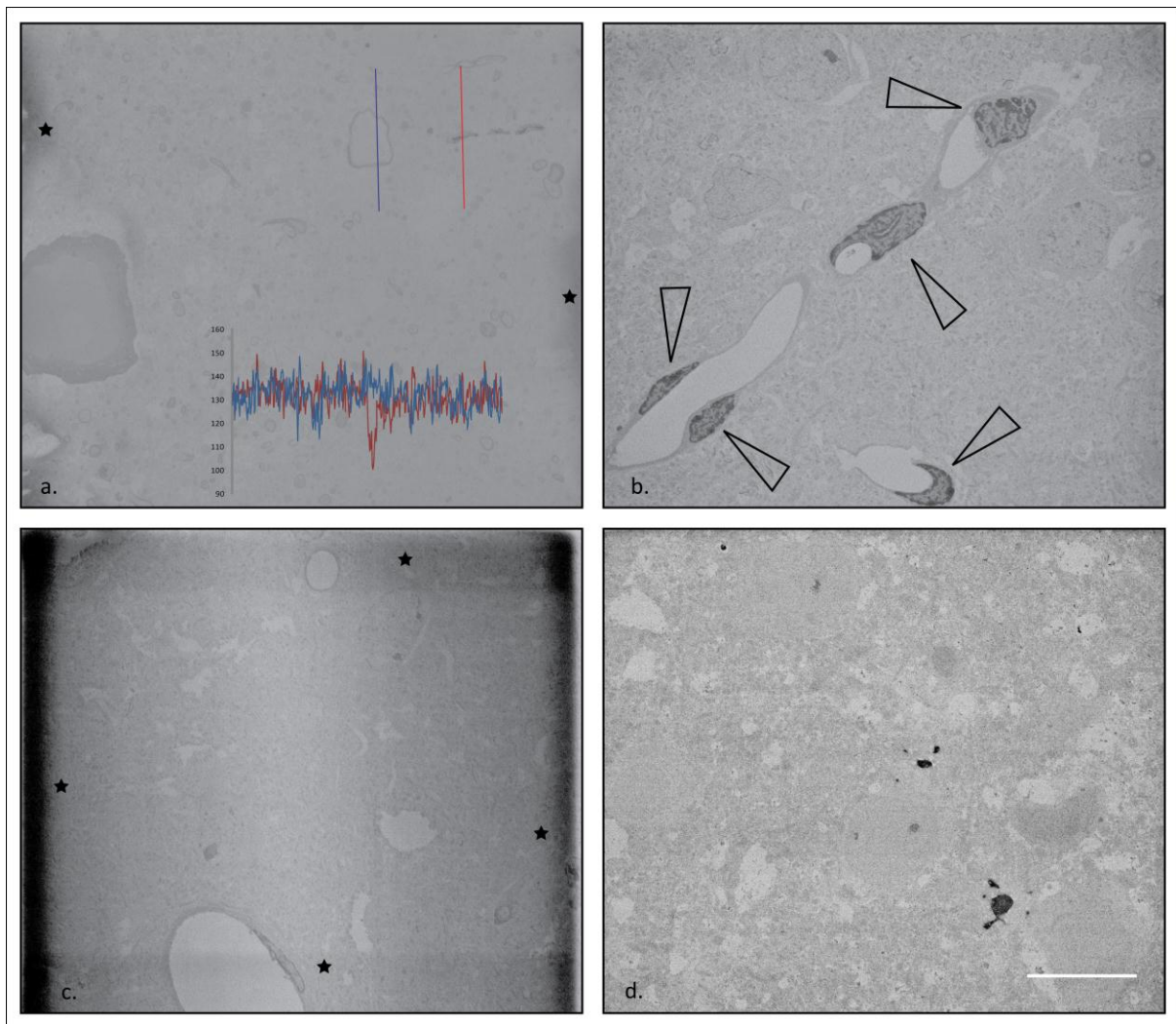


Figure 3.4: Artifacts in stained samples in the EM; (a.): The image shows an example for a weak contrasted neuron: red and blue histogram resembles the grey value distribution indicated by the red and blue bar, respectively. The tissue is moderately charged (stars); (b.): Sample of large unintentionally stained structures (arrowheads); (c.): if mosaics are scanned, highly charged areas (stars), in particular at the borders and corners, are visible as these are scanned two or four times, respectively; (d.): cross section of desired quality: only the filled neuron shows distinct contrast, no charging and no additional structures are visible; scale bar = $10\mu\text{m}$

25x25x30nm) or (ii) insufficient staining which can be deduced from the quality of the reconstruction.

Several buffer and metal concentrations were tested out for the principle protocols described in the following sections. As the characteristic results of the individual staining were comparable, only the relevant conclusions that contributed to a working protocol are emphasized.

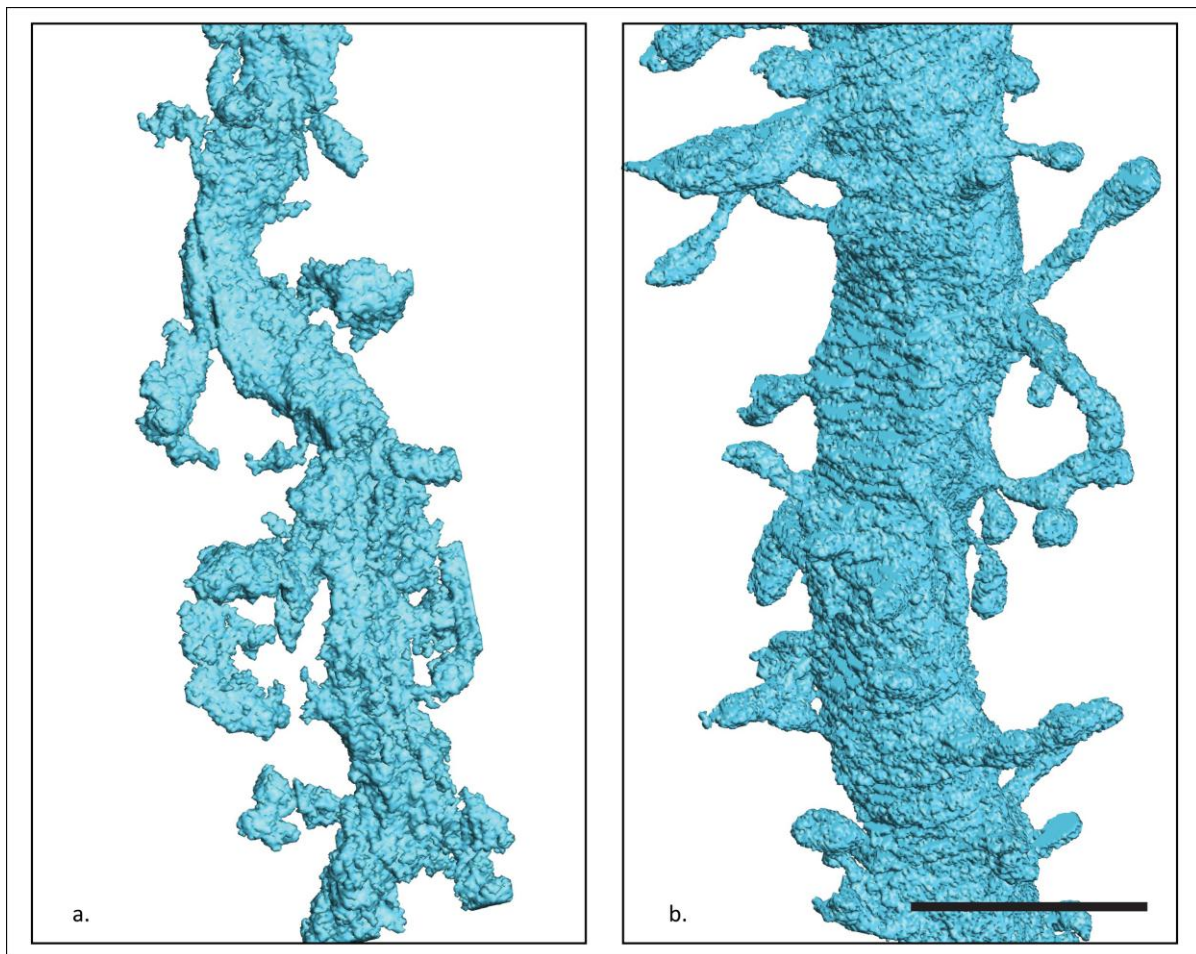


Figure 3.5: Examples to judge segmentation qualities; (a.): represents a very rough and jagged surface, many spine connections are missing and the overall impression resembles poor quality (See section 3.1.2.1); (b.): in comparison illustrates a smooth surface, connected spines and an appropriate overall qualitative segmentation, (see section 3.1.2.3); scale bar =2.5 μ m

3.1.2.1 Staining Protocol using Osmium Tetroxide and Uranium Acetate

The first attempt to obtain a tissue stain in which only the previously filled neuron shows a specifically high contrast, was to apply a standardized block-stain protocol (Hayat, 2000). The staining is based on introducing OsO_4 and uranium ions into the tissue. Uranium is commonly used as uranium acetate (UAc) in EM staining. The uranium cation UO_2^{2+} shows a high affinity for anionic groups such as phosphoryl and carboxyl and thus reacts with molecules such as lipids, nucleic acids, proteins and therefore also all kinds of membranes (Hayat, 2000). For this reason, UAc is widely used as a universal stain and present in almost all published staining methods.

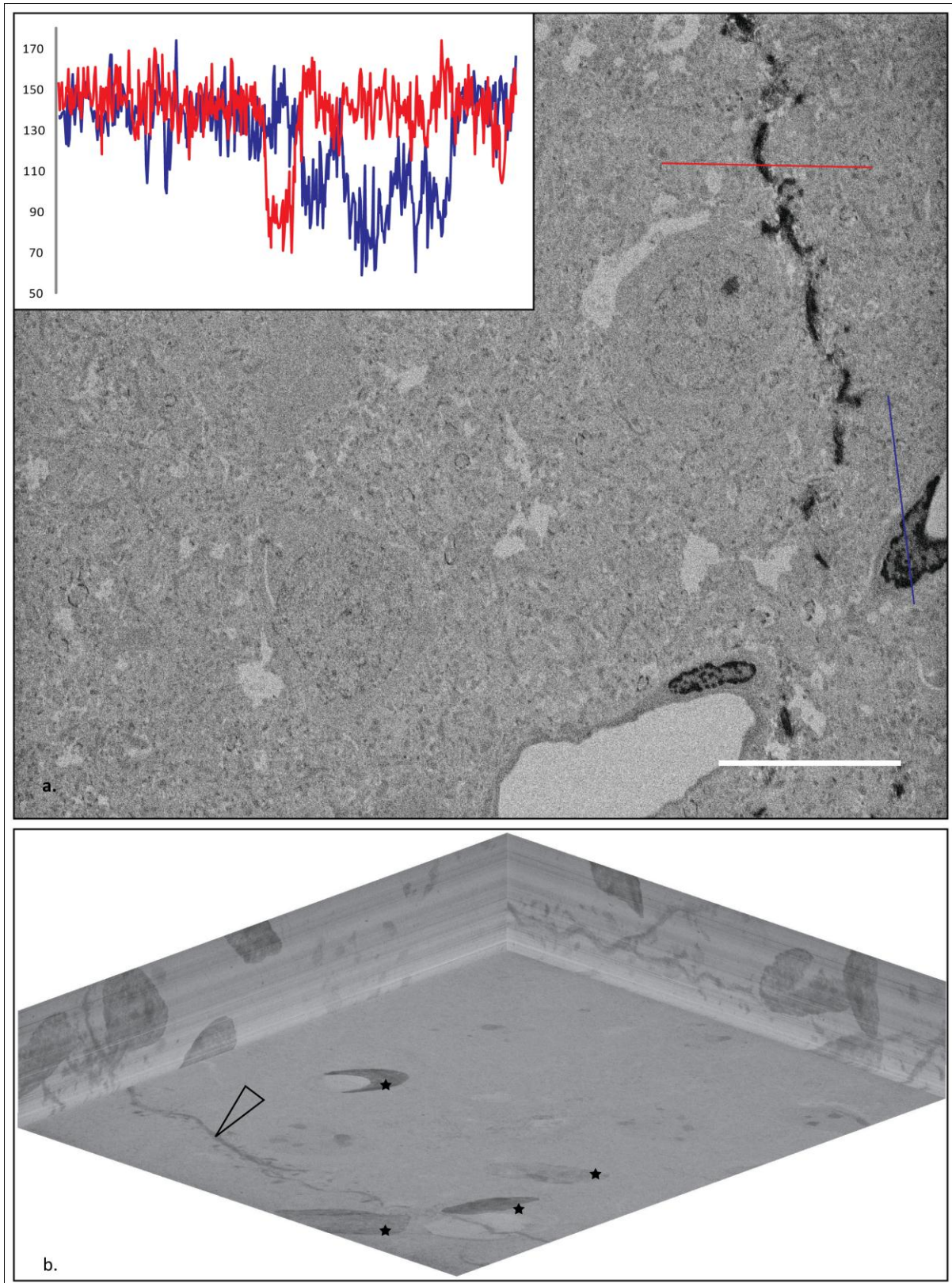


Figure 3.6: Staining protocol using osmium tetroxide and uranyl acetate. The neuronal structure is explicitly enhanced but so are other structures in the surrounding tissue; (a.): Image of an image stack recorded by SBFSEM. Graphs show the grey value distribution of the red and blue bars transecting the structure and an artifact, respectively. Both structures resemble the same amount of contrast; (b.): X-Y-Z- minimum projection of the image stack. Next to the dendrite (arrowhead), intense structures are pronounced (stars); scale bar =10 μ m.

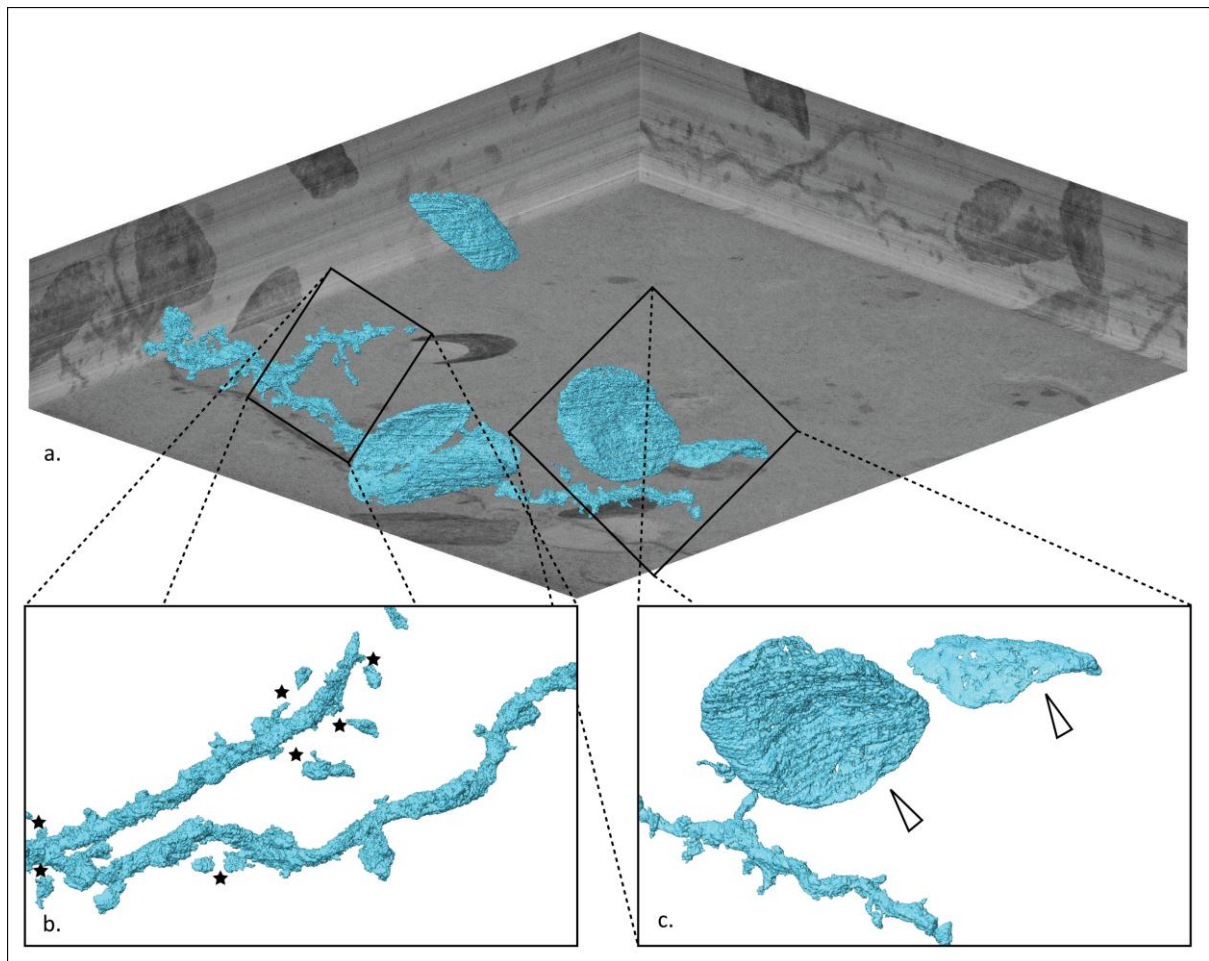


Figure 3.7: Reconstruction of the image stack shown in Figure 3.6: large artifacts and lack of contrast prevent the accurate reconstruction of the dendritic structure; (a.): X-Y-Z-minimum projection with reconstruction; (b.): magnification of dendritic structure. Many connections of spine heads are missing (stars) and the reconstruction seems imperfect due to the limited possibility to set the segmentation parameters; (c.): magnification of unintended stained structures in the tissue (arrowheads).

The staining shows a distinct contrast enhancement of the filled dendrite (Figure 3.6, red bar and graph), however, other structures, were also heavily stained and resulted in the same contrast intensity (blue bar and graph). These undesired stains were most likely introduced or enhanced by the UAc for its quality of being a universal stain for tissue. As a consequence, the automated segmentation of this image stack led to large disturbing artifacts in the reconstruction (Figure 3.7(a.) and (c.)). As they appear to embrace the capillaries, it can be assumed that they are stained endothelial cells or pericytes (Weaker & Herbert, 2009). Due to a similar contrast distribution of the filled neuron and these co-stained artifacts, the parameter setting of the segmentation algorithm could not be adjusted to remove these unwanted structures. In addition, the neuronal structure could not be segmented with enhanced quality due to the close proximity of the artifacts and the therefore limited choice

of the parameter settings. As mentioned in section 1.4, similar artifacts also appeared in earlier studies by Saetzler et al. (Saetzler et al, 2009) and Lang et al. (Lang et al, 2011b) who used a similar, comparable kind of staining. This study additionally exhibited how background structures interfere with computerized segmentations (compare Figure 1.9). Therefore, this type of block-stain was deemed unsuitable for the specific and artifact-free staining of a single biocytin-filled neuron.

3.1.2.2 Staining Protocol using only Osmium Tetroxide

Using UAc for contrasting tissue is an absolute standard and usually satisfies the experimenter's goal of obtaining an intense overall negative stain. However, for the presented work, the standardized staining protocols did not bring the desired result of having a strong contrast for only the dedicated neuron of interest and not the neuropil or other prominent structures. For this reason an approach of block-staining was attempted without UAc. This technique, however, resulted in an insufficient staining of both tissue and neuronal structure. Figure 3.8 demonstrates that the OsO_4 alone did not result in a good constant contrast of the neuron nor did it result in a high difference between structure and background. Moreover, due to the lack of metal ions in the tissue, the electrons from the microscope's scanning beam could not be discharged, which led to a significant charging of the sample (borders in (a.); stars in (b.)). A positive effect from omitting the UAc was the absence of bigger artifacts within the tissue as observed in the section above. This supported the theory that UAc was responsible for the unspecific contrast increase of unwanted structures. Small punctual precipitates could be found (filled arrowheads in (a.)), but as this "osmium-pepper" did not interfere with the automated segmentation of the dendritic structure, it could be disregarded (Figure 3.9). These small punctual artifacts might occur if OsO_4 reacts with glutaraldehyde to form an OsO_4 polymer. Pepper artifacts can also occur from other heavy metal stains such as uranium acetate or lead citrate (Crang & Klomprens, 1988).

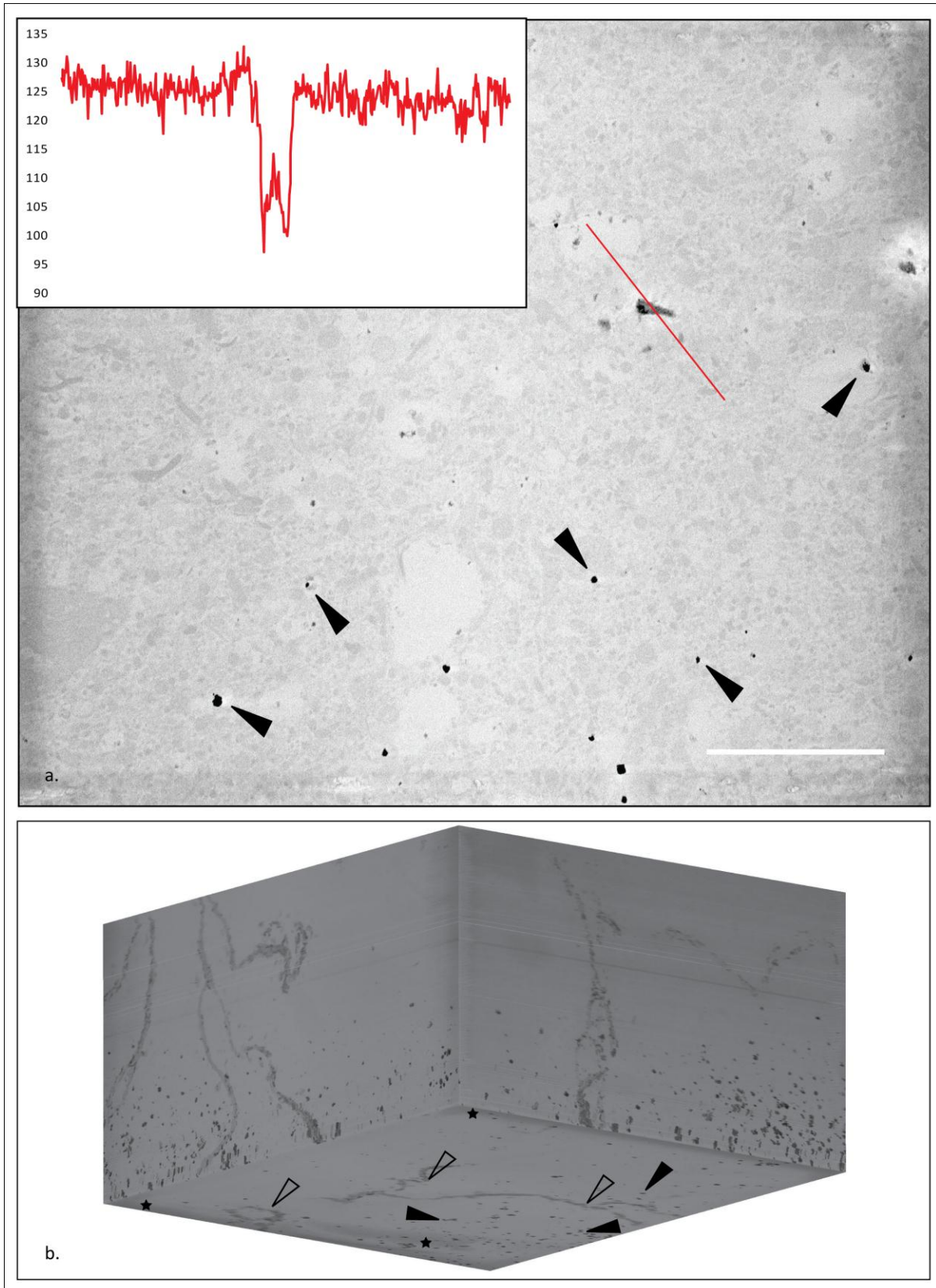


Figure 3.8: Staining Protocol using only osmium tetroxide: The neuronal structure is enhanced relative to the background; no visible unwanted structures were observed; (a.): Image of an image stack recorded by SBFSEM. Graph shows the grey value distribution of the red bars cutting the structure; filled arrowheads mark punctual osmium-pepper, the image is charged at the borders; (b.): X-Y-Z- minimum projection of the image stack; dendrites are marked with hollow arrowheads, charging of the sample is indicated by stars; scale bar =10 μ m.

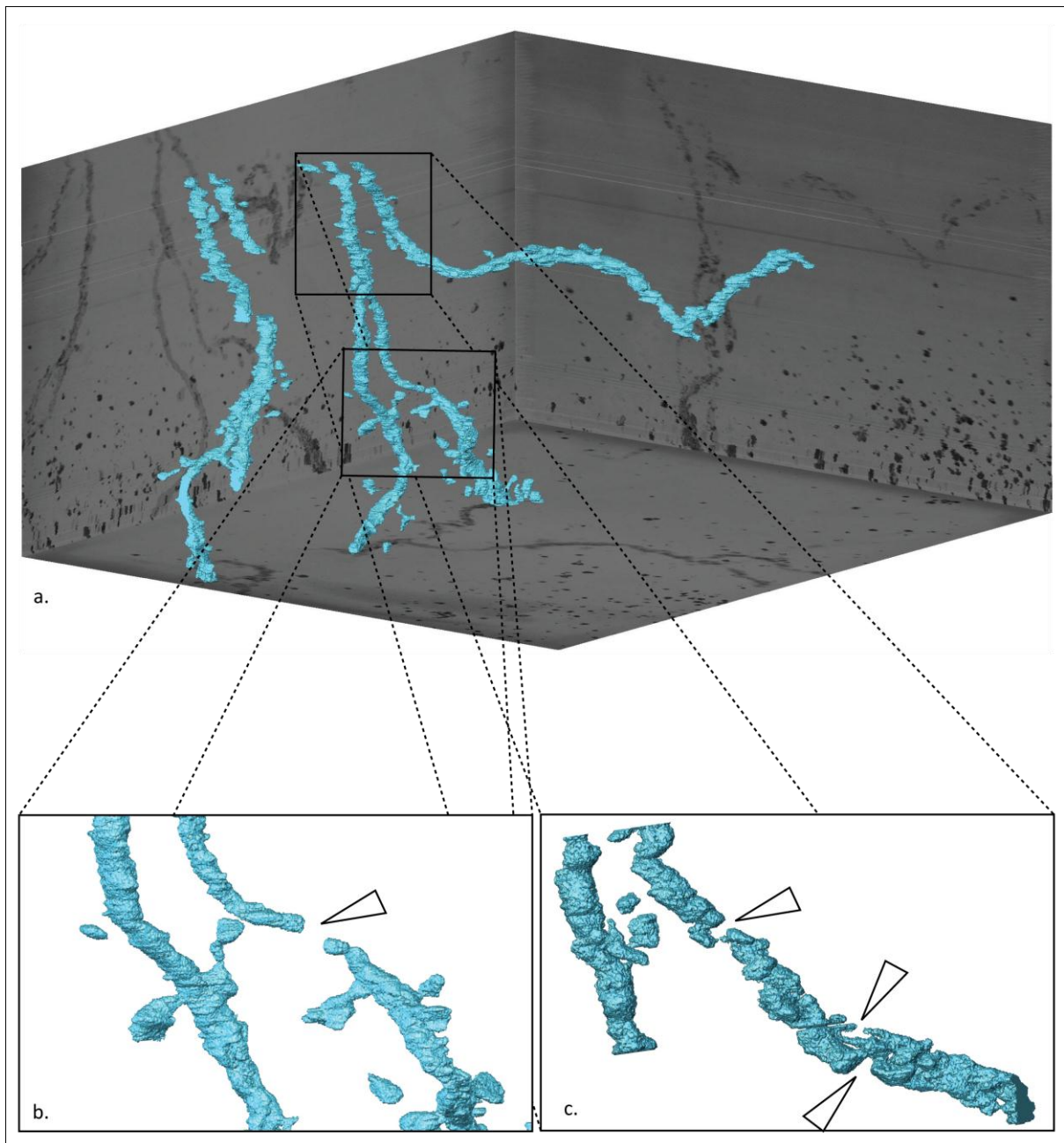


Figure 3.9: Reconstruction of the image stack shown in Figure 3.8; (a.): X-Y-Z- minimum projection with reconstruction; (b.): enhancement of earlier dendritic structure. The dendrite's surface looks relatively smooth, however, the segmentation is incomplete due to insufficient contrast; a large piece of the dendrite is missing entirely (arrowhead); (c.): enhancement of subsequently scanned dendritic structure. The surface of the dendrite looks very rough and jagged, and reveals gaps (arrowheads).

The segmentation of this dataset showed a rather jagged reconstruction (Figure 3.9). Choosing adequate parameters for the segmentation was limited by the contrast difference of the dendrites in comparison to the surrounding neuropil. Figure 3.9 depicts the initially satisfactory result of the dendritic structure and connected spines. However, the lack of overall contrast in the sample had two crucial consequences: (i) the sample was charged and (ii) the autofocus routine of the scanning script was not applicable. Therefore, the sample

lost focus over time (c.) and subsequently acquired images were blurry. The reconstruction of the later dendritic backbone shows many gaps (arrowheads) and appears rough compared to the earlier backbone in (b.). Moreover, no proper spine or spine-like structures could be further resolved.

3.1.1.3 Staining Protocol using Osmium Tetroxide and Lead Citrate

By the first efforts to develop a specific staining for single biocytin-filled neurons, the principle of only fixing and staining the tissue with OsO_4 and omitting the UAc proved to be the most promising. To compensate for the lack of uranium and the consequential scarcity of conductive metals in the sample, lead citrate was used as an additional *en-bloc* stain. Like uranyl acetate, lead citrate has become a common stain for EM sections, however, in the presence of reduced OsO_4 , the contrast is more enhanced by lead citrate than by uranyl acetate (Hayat, 2000). Lead citrate prefers binding to membranes if they are fixed with OsO_4 rather than to native membranes, which indicates the specific binding to reduced OsO_4 . The theory behind this is that reduced OsO_4 , which presumably binds to unsaturated lipids in membranes, is thus acidic and therefore exhibits high affinity for cations like Pb^+ (Hayat, 2000). This enhancement of membrane contrast can only be observed when the treatments occur before dehydration of the sample, which can be done *en bloc* but not after cutting slices from the embedded block, as it is done for conventional electron microscopy.

In the case of this study the reduced OsO_4 is highly concentrated at the DAB polymer, hence it should show a similar affinity to lead citrate, which leads to an enhanced specific contrast for the filled neuron. Since OsO_4 is also present on every membrane, lead citrate is additionally bound and the overall amount of conductive metal is increased, which prevents charging of the sample. A common lead citrate used for staining was developed in the 1960s by Edward Reynolds; therefore this stain is called Reynold's Lead (Reynolds, 1963). The application of Reynold's Lead is not trivial, as lead salts tend to build insoluble lead carbonate crystals when exposed to CO_2 in the air.

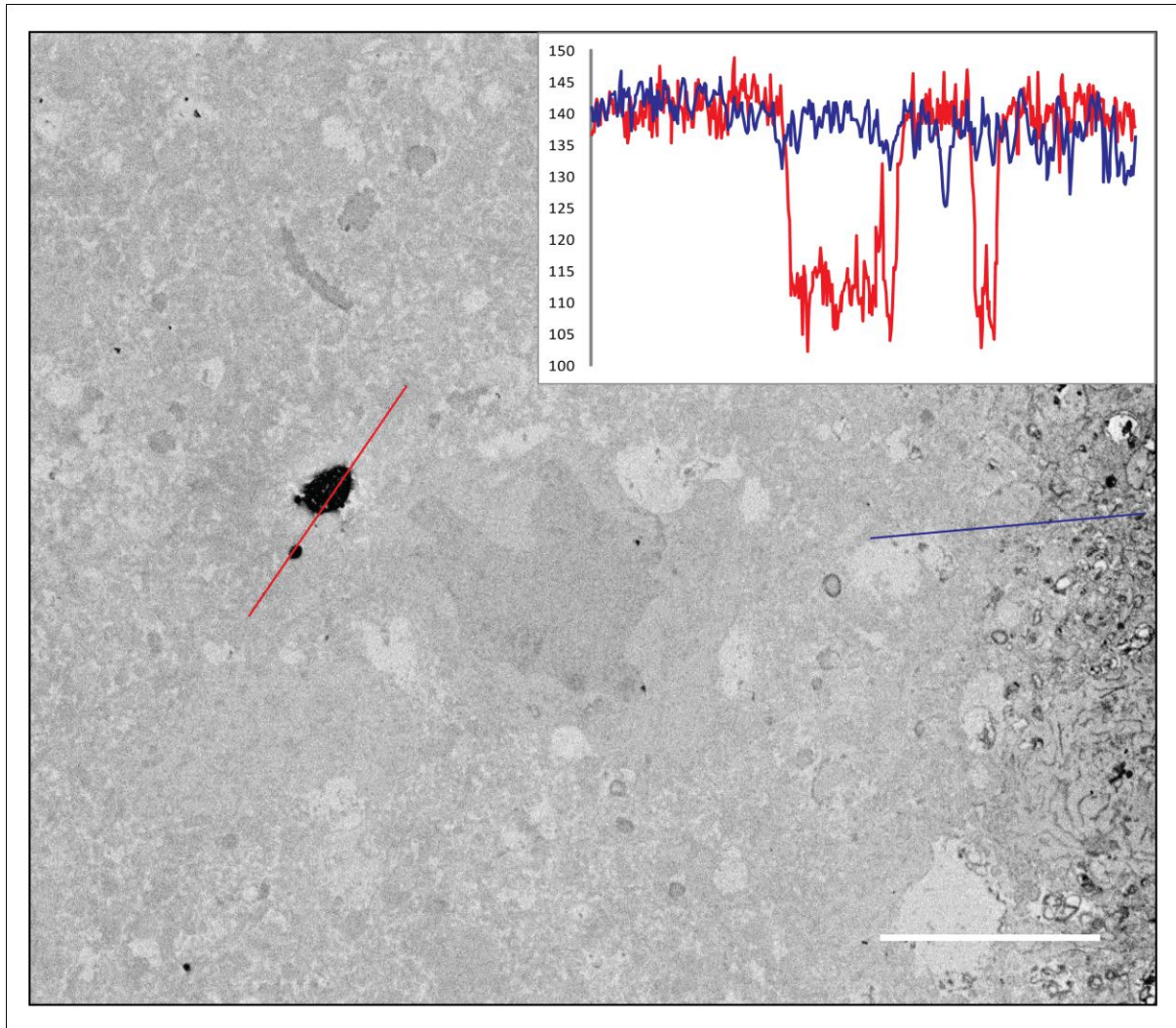


Figure 3.10: Staining Protocol using osmium tetroxide and lead citrate; cross section of an image stack recorded by SBFSEM. Red graph shows the grey value distribution of the red bars transecting a dendrite and a nearby spine head; the neuronal structure is clearly discriminated from the surrounding neuropil; no visible unwanted structures are observed, however the neuropil at the border of the sample (right) assimilated more metals than the inside of the tissue block and therefore shows increased contrast. Blue graph shows the grey value distribution of this area. The marginally increased contrast did not influence the reconstruction; scale bar = 10 μ m.

Therefore, only degassed water must be used before and after application to the tissue to avoid precipitation and the incubation must be hermetically sealed. The evolved staining result shows an explicit increase in the contrast of the stained neuron where the structure is clearly distinguishable from the surrounding neuropil (Figure 3.10). The contrast difference in the slice was about 30 grey values (gv), which is enough difference to clearly differentiate signal from background.

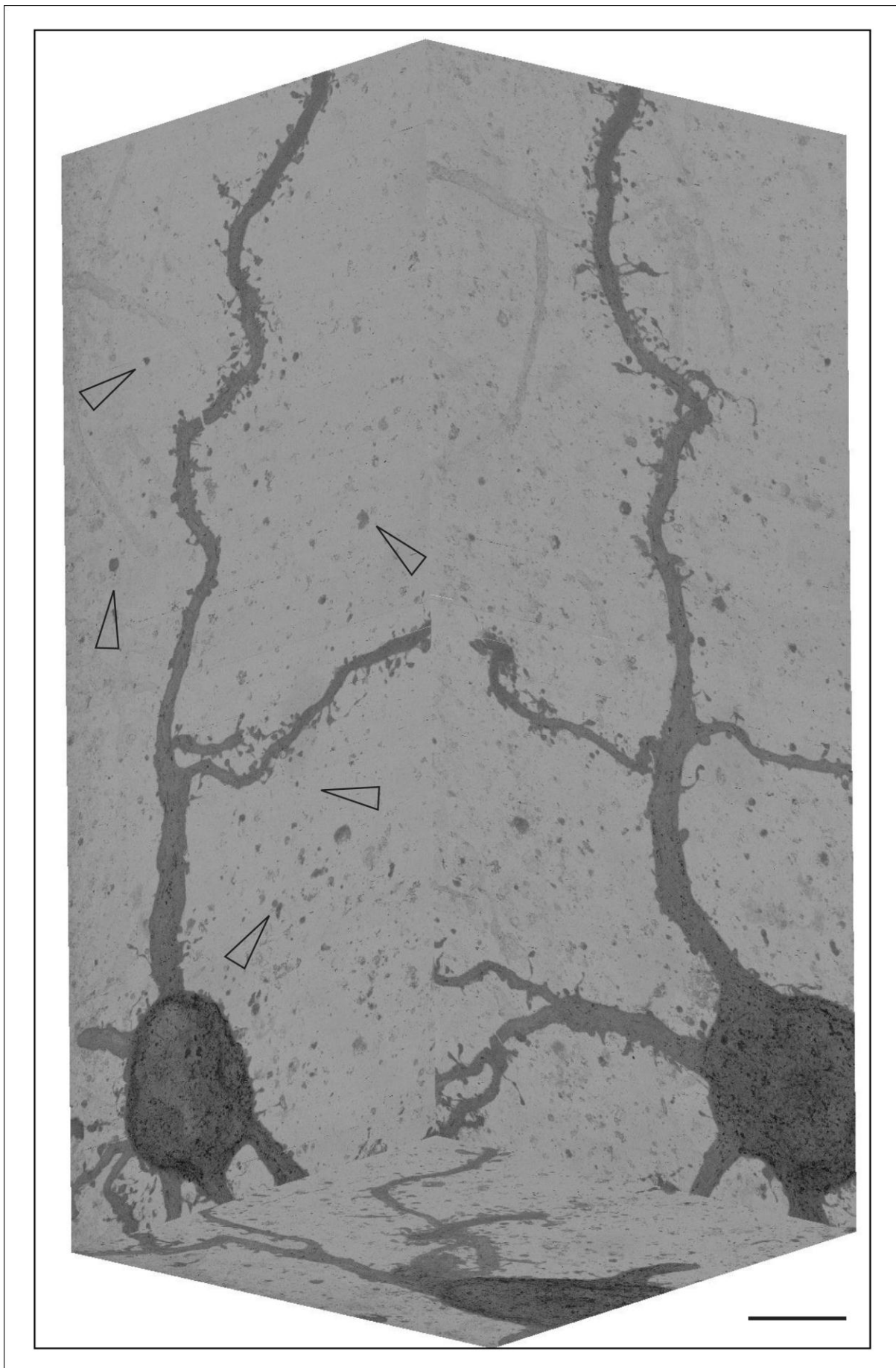
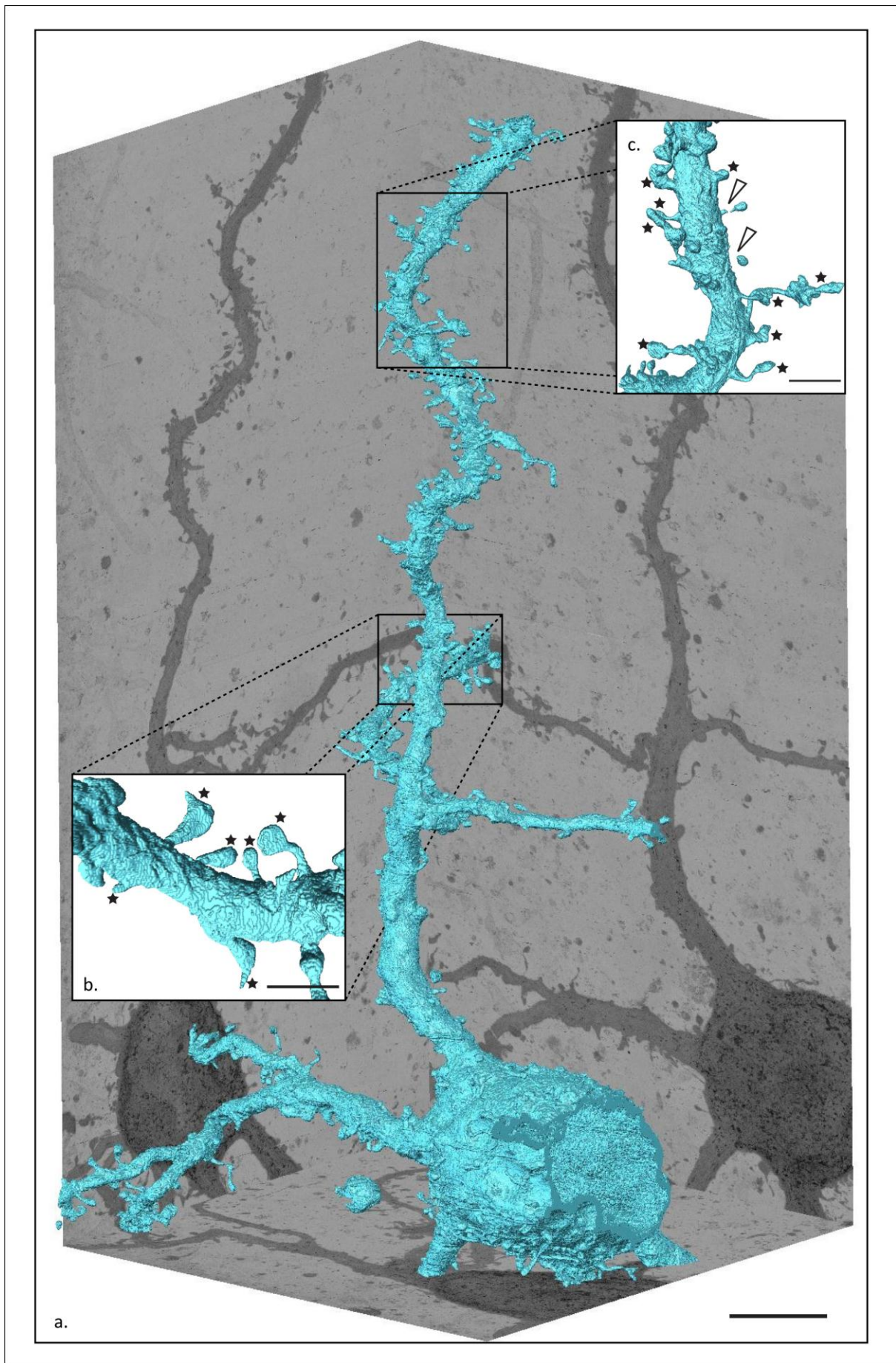


Figure 3.11: (above): X-Y-Z- minimum projection of the stack from which image in Figure 3.10 is derived: The projections show the increased contrast of the neuronal structure over the background. No significant structural artifacts are visible, small local round artifacts (osmium-or lead-pepper), however, can be observed throughout the projections (arrowheads), but did not interfere with the subsequent segmentation; scale bar= 10 μ m.

In comparison to the previously described stainings, finding the appropriate segmentation parameters for this staining was rather simple. The neuronal structures were more complete and had more integrity than staining the neuron with OsO₄ only (Figure 3.9). The incorporated lead citrate seemed to increase the specific as well as the overall contrast. Thus the sample did not charge and the whole stack remained in focus during the scan. Although lead citrate was incorporated throughout the tissue no distinct undesirable structures were stained in contrast to the UAc staining. In Figure 3.12 the reconstruction of the neuron from the image stack of Figure 3.11 is shown. As could be seen for the OsO₄-only staining, an incomplete segmentation (due to insufficient staining) resulted in a rough surface and incomplete dendrites. Staining with the addition of lead citrate resulted in a smooth surface and a dendritic backbone that is adequately filled. The enlargements (b.) and (c.) show that the structure is consistent in its quality for the whole data stack. Many dendritic spines can be detected (stars), although some lack their connecting necks (arrowheads). The surfaces of the spines also appear smooth and complete. Like the OsO₄-only protocol, the visible small osmium- or lead-pepper artifacts (arrowheads in Figure 3.11) did not interfere with the reconstruction.

Since the staining and segmentation using OsO₄ and lead citrate proved satisfactory, the protocol was introduced as the standard methodology used in subsequent experiments. All cells stained with this protocol showed the same specific contrast enhancement of the desired structures, thus highlighting the high reproducibility of the protocol. The staining protocol will be evaluated and validated in the following chapter.

Figure 3.12: (below): Reconstruction of the image stack shown in Figure 3.11; (a.): X-Y-Z- minimum projection with reconstruction; (b.) and (c.): enlargements of dendritic structure, the dendrite's surface looks smooth and complete, dendritic spines are mostly connected (stars) and their structure also appears physiological. No artifacts are segmented and although a lot of small pepper-like artifacts are visible in the projections, they did not interfere with the segmentation. Missing spine necks are marked with arrowheads; scale bars= 10 μ m for a., 2.5 μ m for b. and c.



3.1.3 Evaluation of the Staining Protocol

3.1.3.1 Contrast Evaluation in the SBFSEM

Using osmium tetroxide and lead citrate as contrast metals for single biocytin-filled neurons, gave excellent results: (i) specific and continuous contrast difference of the stained neuron and the neuropil, (ii) no intensely stained artifacts, that interfere with the segmentation of the neuronal structure, (iii) sufficient metal concentration in the surrounding tissue to provide a background contrast that allows the auto-focus routine to function and (iv) to avoid excessive charging of the sample.

To test the reproducibility of the staining, ten single filled neurons were stained and scanned in the SBFSEM. The image stacks for evaluation consisted of 375 to 1175 images which correspond to a physical size of 11 to 35 μm in Z. Reconstructions from all image stacks could be obtained and the individual staining qualities were quantified as follows. From every 50th image (total of 168 images) of an individual image stack, the grey values along a 500 pixel

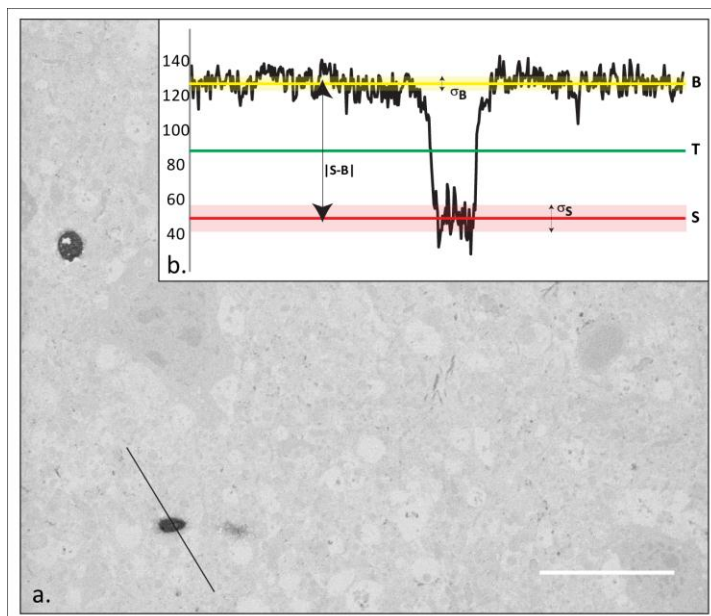


Figure 3.13: (a.): cross section; (b.): plotted grey value profile of black line in a., graphical display of evaluation parameters: threshold (T, green), mean background (B, yellow), mean signal (S, red), standard deviations for S and B (red and yellow shaded, respectively). Measurements for this section: $|S-B|=76$, $\sigma_S=11$, $\sigma_B=6$, $t=5.78$; scale bar= 10 μm .

line transecting through the stained neuron, were extracted (Figure 3.13). These values were thresholded into signal and background values. For most data it was possible to determine the threshold (T) by the median of the means of the five brightest and the five darkest values. All values lighter than T were declared background pixel, whilst darker pixels were declared signal pixel. The mean values of all background and signal pixels were declared B and S, respectively. These

calculations can be visualized in Figure 3.13(b.). An average contrast difference between S and B ($|S-B|$) gave an indication of how successful and specific the staining worked for the sample. To properly evaluate the quality of the staining and ease of segmentation, this difference alone was not decisive. The average $|S-B|$ ranged from 23 up to 70 gv for the different datasets, but the performance of the segmentation (finding the adequate parameters, reconstructed surface quality) was successful regardless of the value of $|S-B|$. The ease, quality and robustness of the segmentation could be determined by a t-distribution of the grey values of S and B. The higher the t-value, the easier and more robust the segmentation, and thus, the better the quality of the stained neuron. The standard deviations (σ) of S and B were different and were therefore taken into account separately. T-values of all ten datasets lied between 3.18 and 4.69 (Table 3.1).

Summary of the Protocol Evaluation				
	$ S-B $ [gv]	σ_B [gv]	σ_S [gv]	t =
TK020408E	23.26	3.37	5.39	3.76
TK120509B	64.36	7.39	11.83	4.69
TK100909A1	29.18	4.54	6.91	3.52
TK190111A	69.87	10.40	17.00	3.53
TK190111B	55.38	8.11	12.50	3.76
TK120910F	46.31	8.53	8.72	3.77
TK091110A	61.87	10.09	13.95	3.60
TK091110B	67.76	8.91	13.32	4.23
TK091110F	62.75	9.62	14.03	3.67
TK091110G	52.73	9.32	14.03	3.18
Average	53.35	8.03	11.77	3.77
Non-Segmented Dataset				
	$ S-B $ [gv]	σ_B [gv]	σ_S [gv]	t =
TK280211F	15.56	5.20	6.16	1.93

Table 3.1: Summary of the results for the evaluation of the staining protocol: Averaged values for every dataset and overall average. For comparison, values for one non-segmentable dataset are shown.

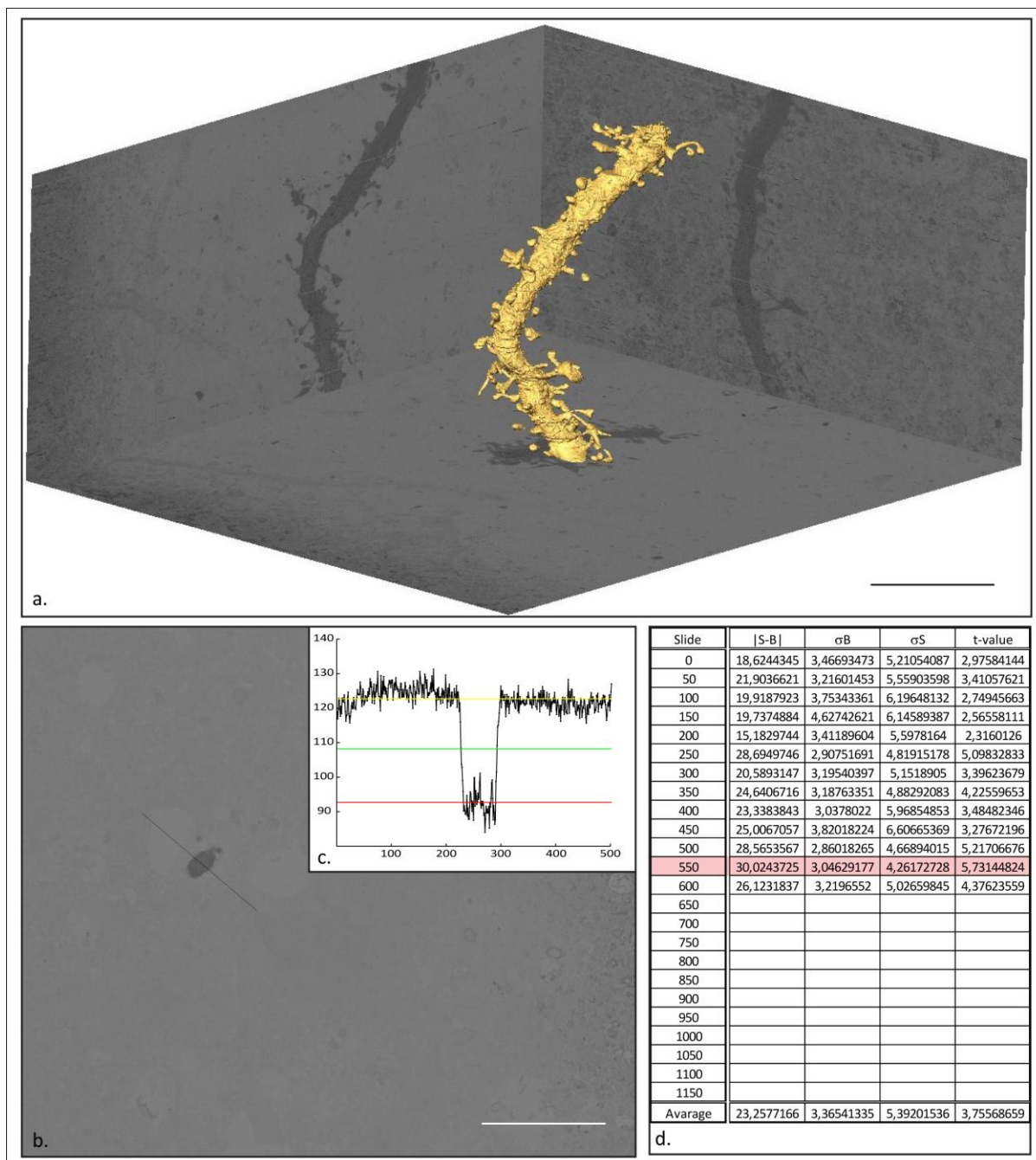


Figure 3.14: Dataset TK020408E_st004_3; (a.): X-Y-Z-projection with reconstruction; the dataset consists of 632 images which corresponds to a physical size of $18.96\mu\text{m}$ in Z, 13 cross sections were analyzed for contrast distribution; (b.): cross section with measure line; (c.): grey value plot of measure line in (b.), signal mean S (red), threshold (green), background mean B (yellow); (d.): $|S-B|$, σ_B , σ_S , and t-values for every single evaluated cross sections of the dataset, values of the cross section shown in (b.) and (c.) are shaded in red; scale bar = $10\mu\text{m}$.

Average values of this data stack were: $|S-B| = 23$, $\sigma_B = 3.4$, $\sigma_S = 5.4$, $t = 3.756$.

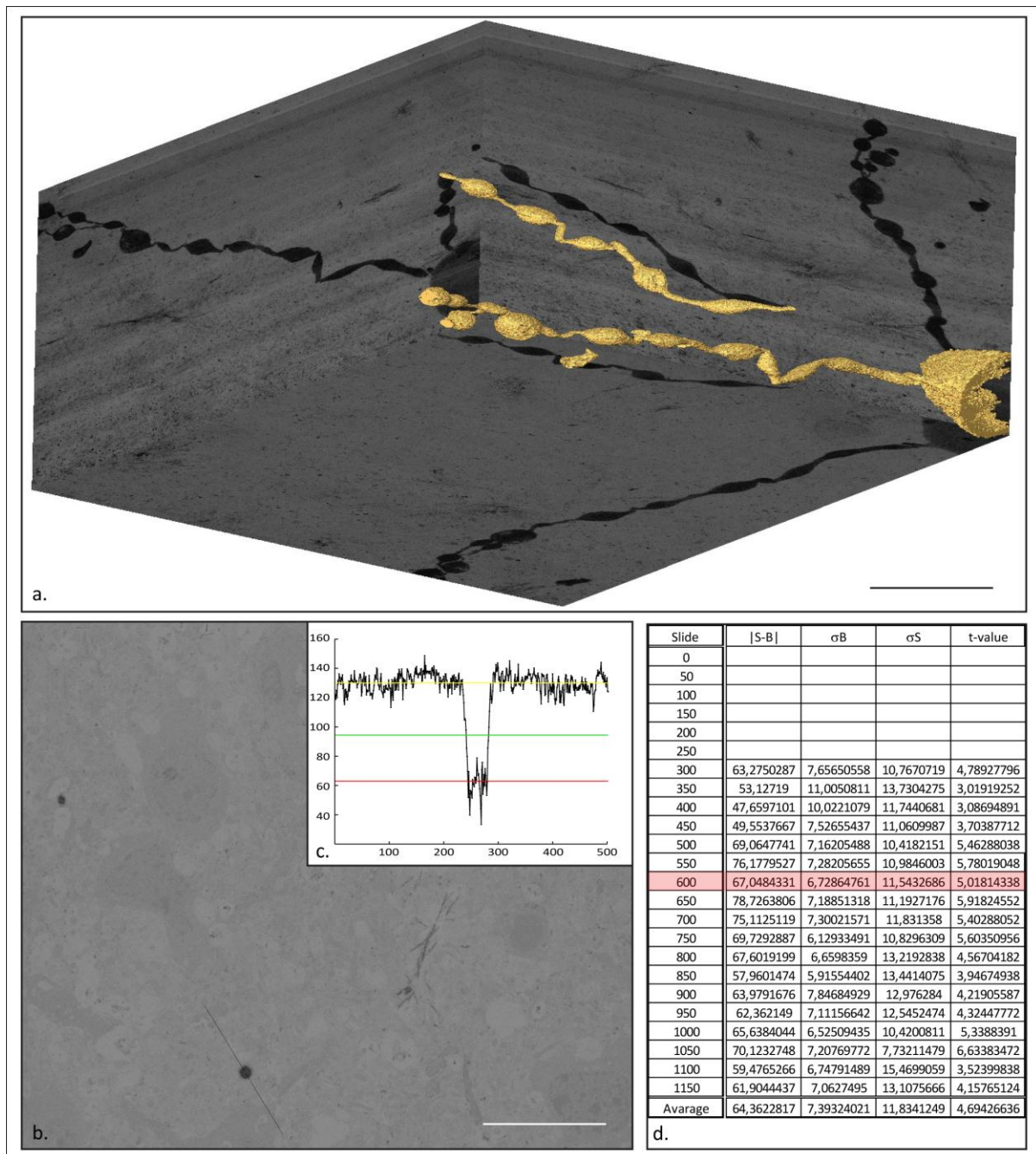


Figure 3.15: Dataset TK120509B_st004_3; (a.): X-Y-Z-projection with reconstruction; the dataset consists of 1199 images which corresponds to a physical size of $35.97\mu\text{m}$ in Z, 18 cross sections were analyzed for contrast distribution; (b.): cross section with measure line; (c.): grey value plot of measure line in (b.), signal mean S (red), threshold (green), background mean B (yellow); (d.): $|S-B|$, σ_B , σ_S , and t-values for every single evaluated cross sections of the dataset, values of the cross section shown in (b.) and (c.) are shaded in red; scale bar = $10\mu\text{m}$.

Average values of this data stack were: $|S-B| = 64$, $\sigma_B = 7.44$, $\sigma_S = 11.8$, $t = 4.694$.

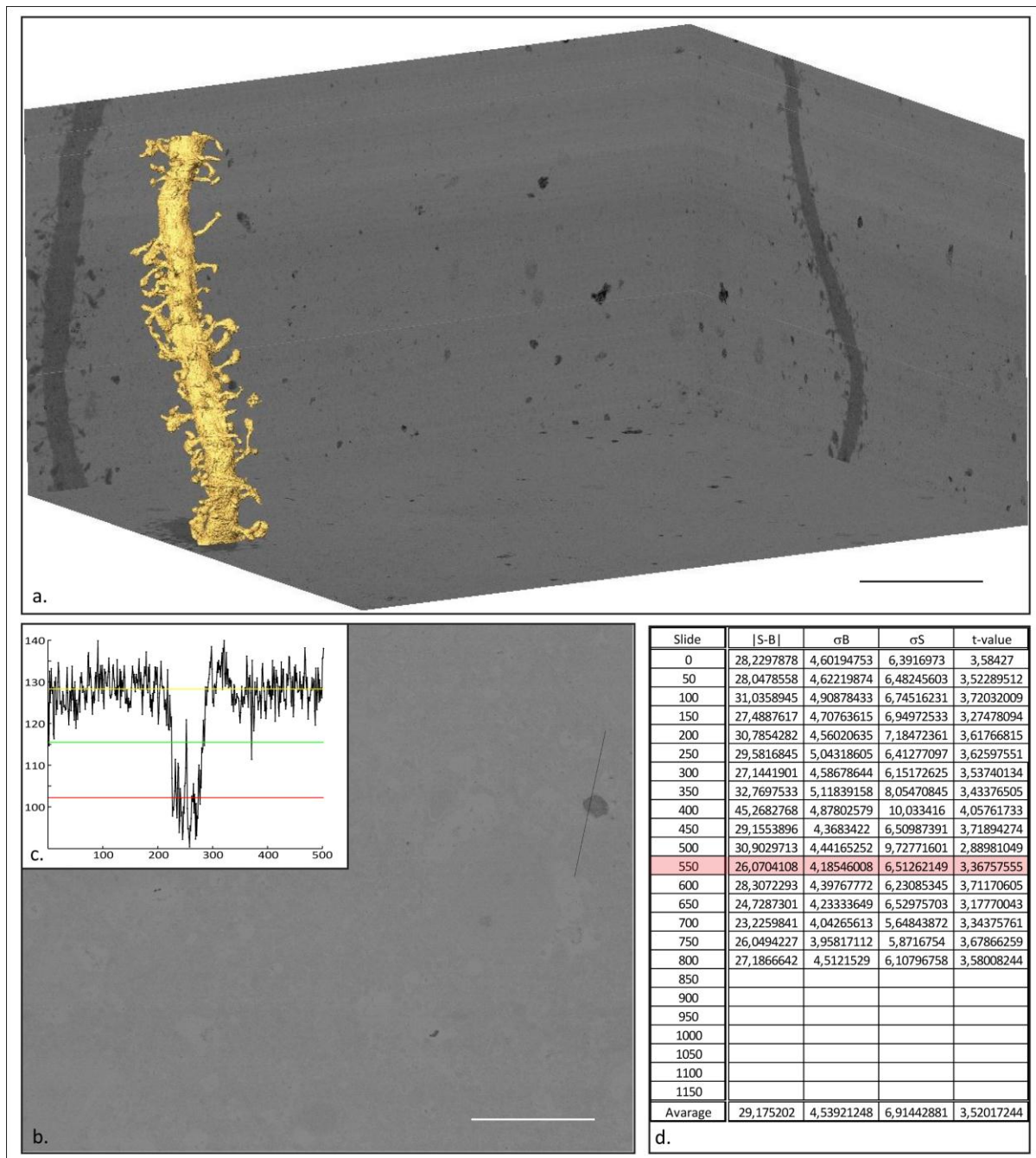


Figure 3.16: Dataset TK100909A1_st011_3; (a.): X-Y-Z-projection with reconstruction; the dataset consists of 846 images which corresponds to a physical size of $25.38\mu\text{m}$ in Z, 17 cross sections were analyzed for contrast distribution; (b.): cross section with measure line; (c.): grey value plot of measure line in (b.), signal mean S (red), threshold (green), background mean B (yellow); (d.): $|S-B|$, σ_B , σ_S , and t-values for every single evaluated cross sections of the dataset, values of the cross section shown in (b.) and (c.) are shaded in red; scale bar = $10\mu\text{m}$.

Average values of this data stack were: $|S-B| = 29$, $\sigma_B = 4.5$, $\sigma_S = 6.9$, $t = 3.52$.

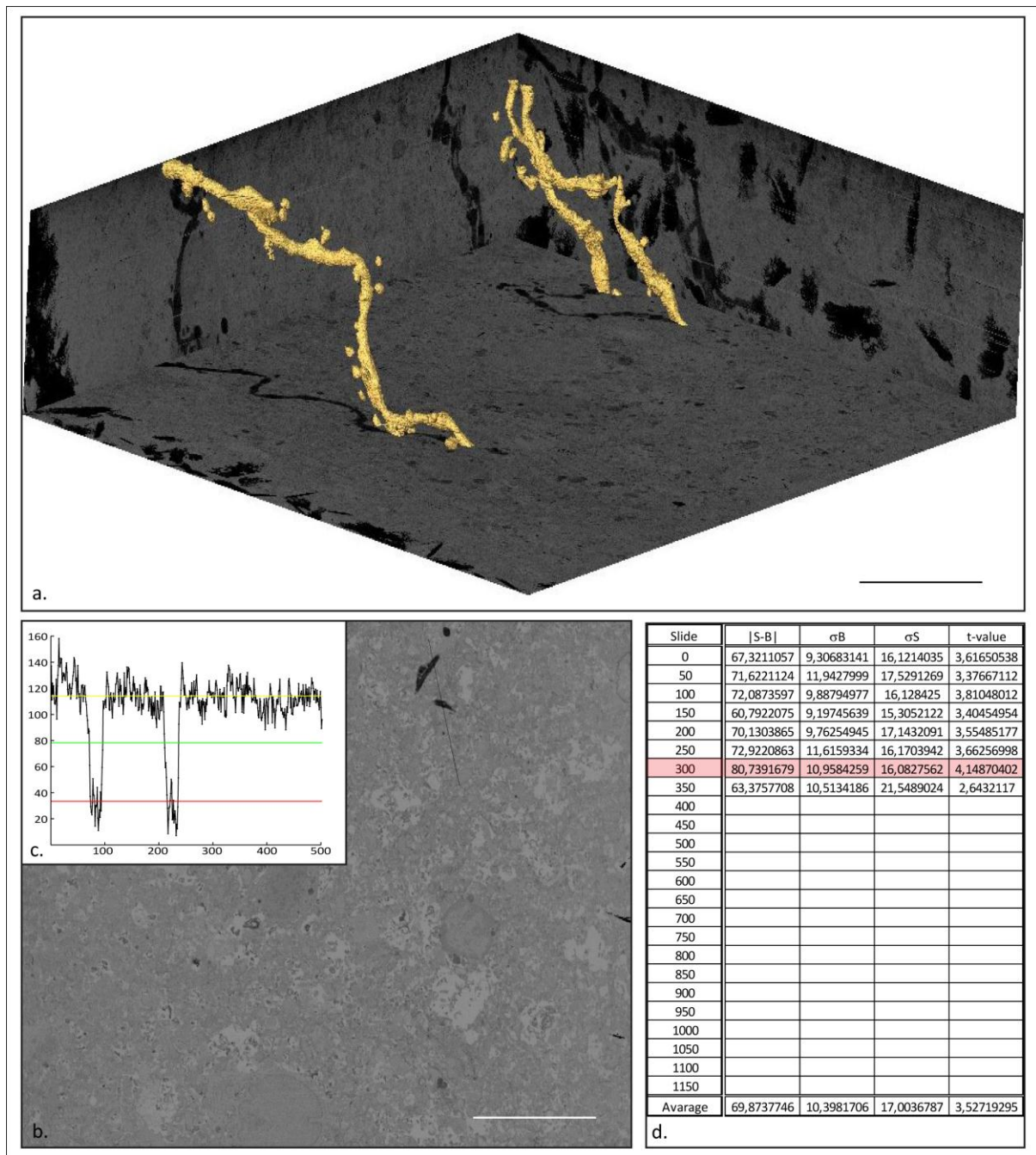


Figure 3.17: Dataset TK190111A_st005_6; (a.): X-Y-Z-projection with reconstruction; the dataset consists of 375 images which corresponds to a physical size of $11.25\mu\text{m}$ in Z, 8 cross sections were analyzed for contrast distribution; (b.): cross section with measure line; (c.): grey value plot of measure line in (b.), signal mean S (red), threshold (green), background mean B (yellow); (d.): $|S-B|$, σ_B , σ_S , and t-values for every single evaluated cross sections of the dataset, values of the cross section shown in (b.) and (c.) are shaded in red; scale bar = $10\mu\text{m}$.

Average values of this data stack were: $|S-B| = 70$, $\sigma_B = 10.4$, $\sigma_S = 17$, $t = 3.527$.

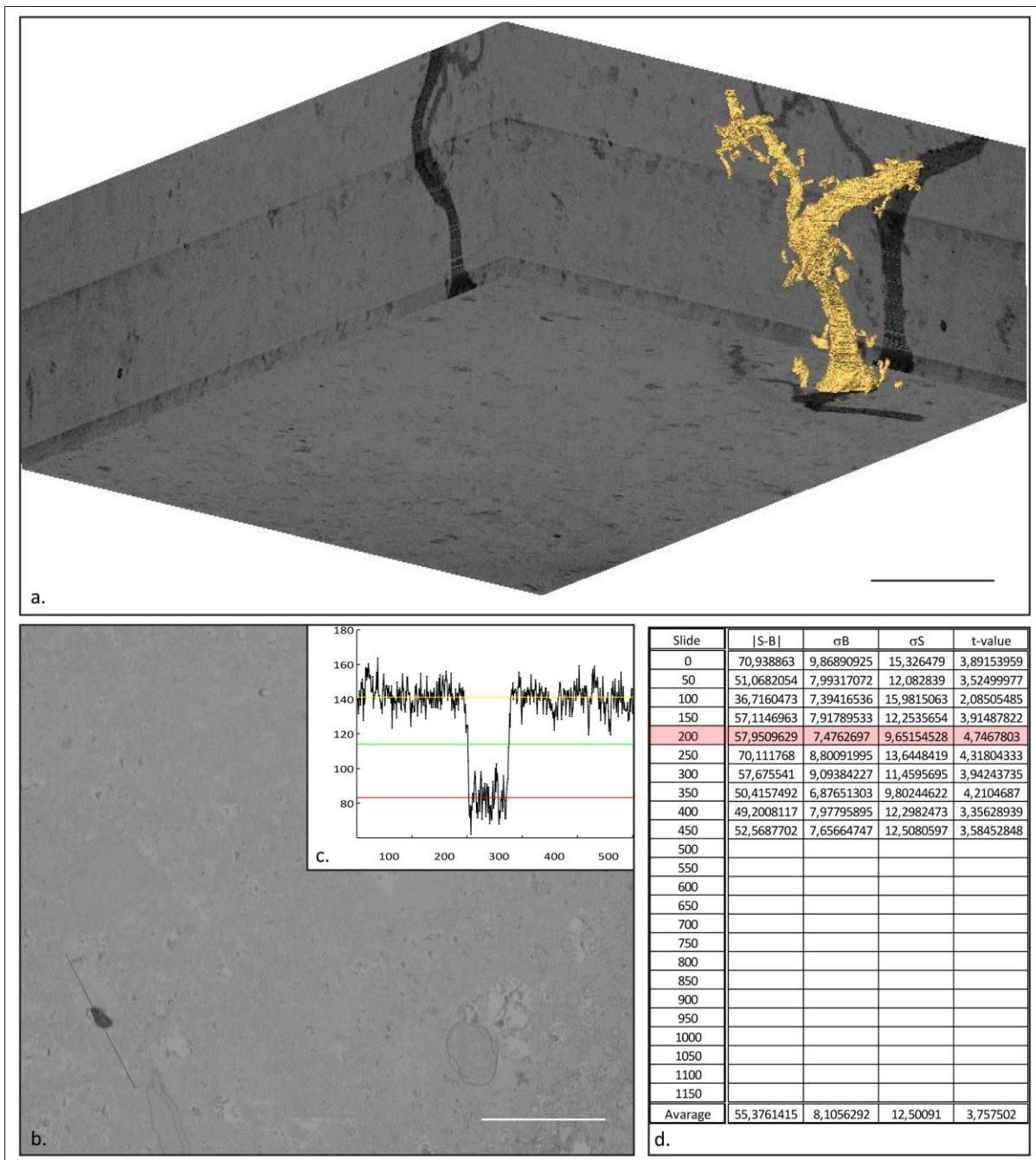


Figure 3.18: Dataset TK190111B_st001_6; (a.): X-Y-Z-projection with reconstruction; the dataset consists of 481 images which corresponds to a physical size of $14.43\mu\text{m}$ in Z, 10 cross sections were analyzed for contrast distribution; (b.): cross section with measure line; (c.): grey value plot of measure line in (b.), signal mean S (red), threshold (green), background mean B (yellow); (d.): |S-B|, σ_B , σ_S , and t-values for every single evaluated cross sections of the dataset, values of the cross section shown in (b.) and (c.) are shaded in red; scale bar = $10\mu\text{m}$.

Average values of this data stack were: $|S-B| = 55$, $\sigma_B = 8,1$, $\sigma_S = 12.5$, $t = 3.756$.

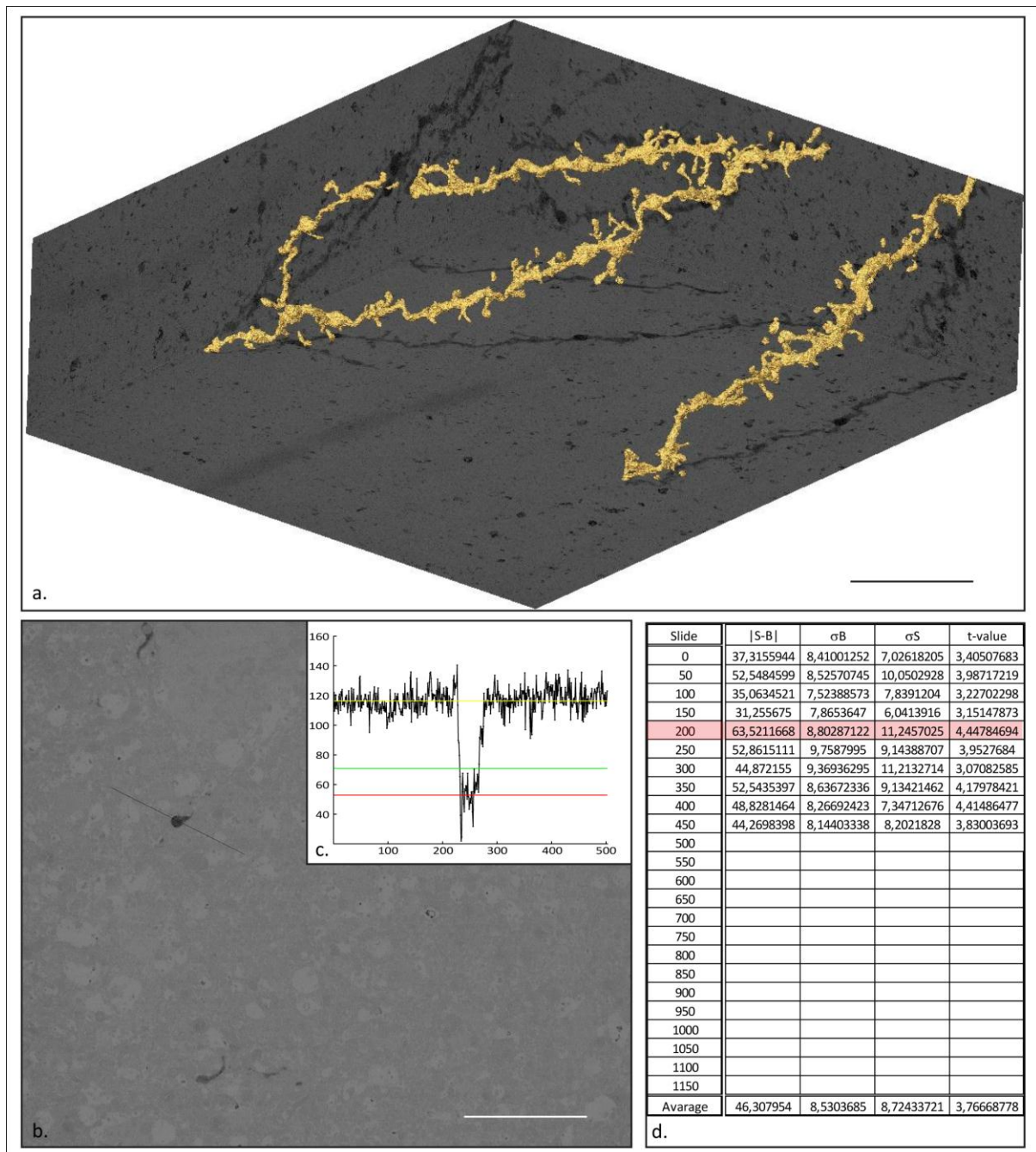


Figure 3.19: Dataset TK120910F_st013_9; (a.): X-Y-Z-projection with reconstruction, the dataset consists of 505 images which corresponds to a physical size of $15.15\mu\text{m}$ in Z, 10 cross sections were analyzed for contrast distribution; (b.): cross section with measure line; (c.): grey value plot of measure line in (b.), signal mean S (red), threshold (green), background mean B (yellow); (d.): $|S-B|$, σ_B , σ_S , and t-values for every single evaluated cross sections of the dataset, values of the cross section shown in (b.) and (c.) are shaded in red; scale bar = $10\mu\text{m}$.

Average values of this data stack were: $|S-B| = 46$, $\sigma_B = 8.5$, $\sigma_S = 8.7$, $t = 3.766$.

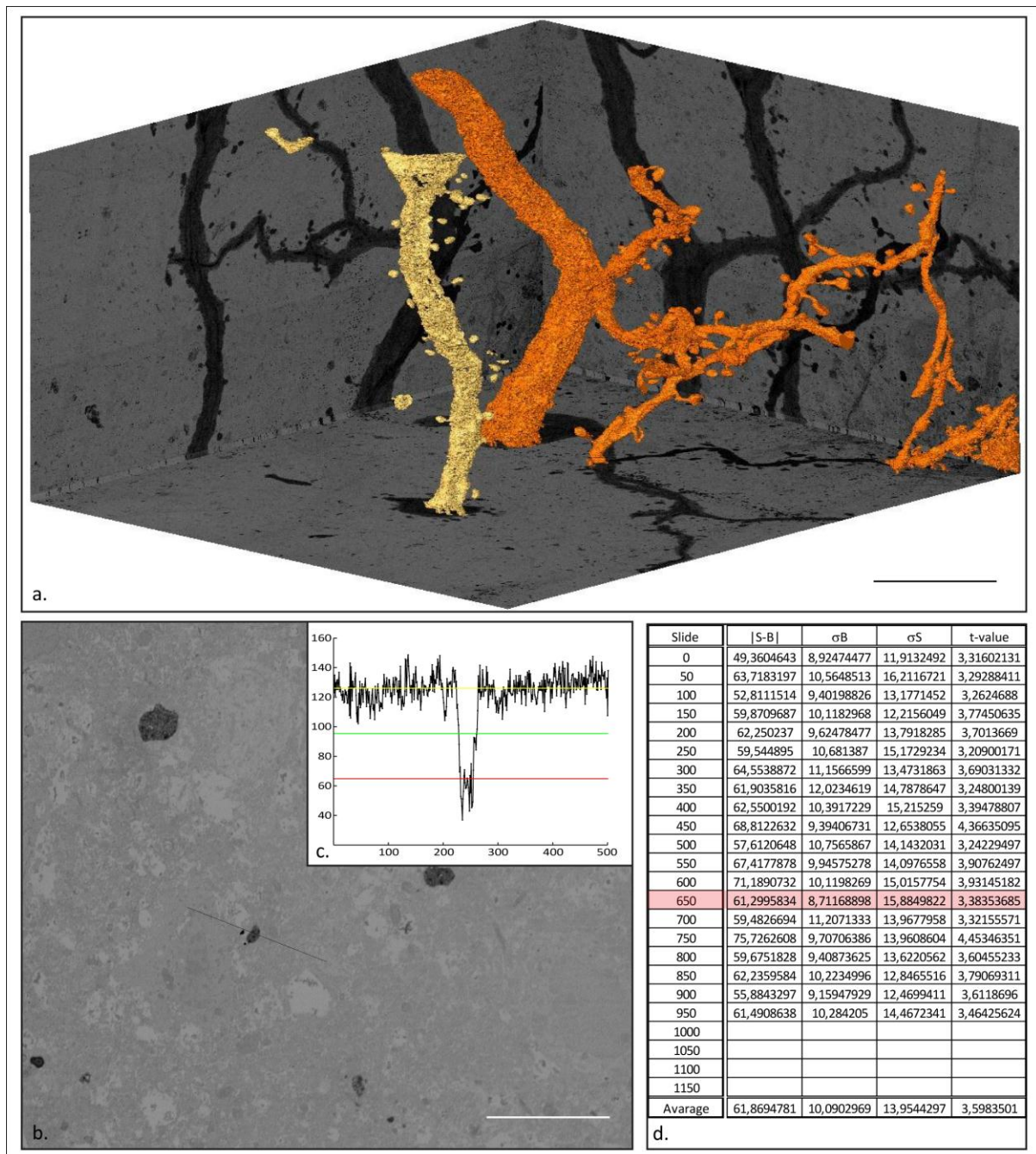


Figure 3.20: Dataset TK091110A_st003_10 (orange); (a.): X-Y-Z-projection with reconstruction, the dataset consists of 1000 images which corresponds to a physical size of $30\mu\text{m}$ in Z, 20 cross sections were analyzed for contrast distribution; (b.): cross section with measure line; (c.): grey value plot of measure line in (b.), signal mean S (red), threshold (green), background mean B (yellow); (d.): $|S-B|$, σ_B , σ_S , and t-values for every single evaluated cross sections of the dataset, values of the cross section shown in (b.) and (c.) are shaded in red; scale bar = $10\mu\text{m}$.

Average values of this data stack were: $|S-B| = 62$, $\sigma_B = 10.1$, $\sigma_S = 13.9$, $t = 3.598$.

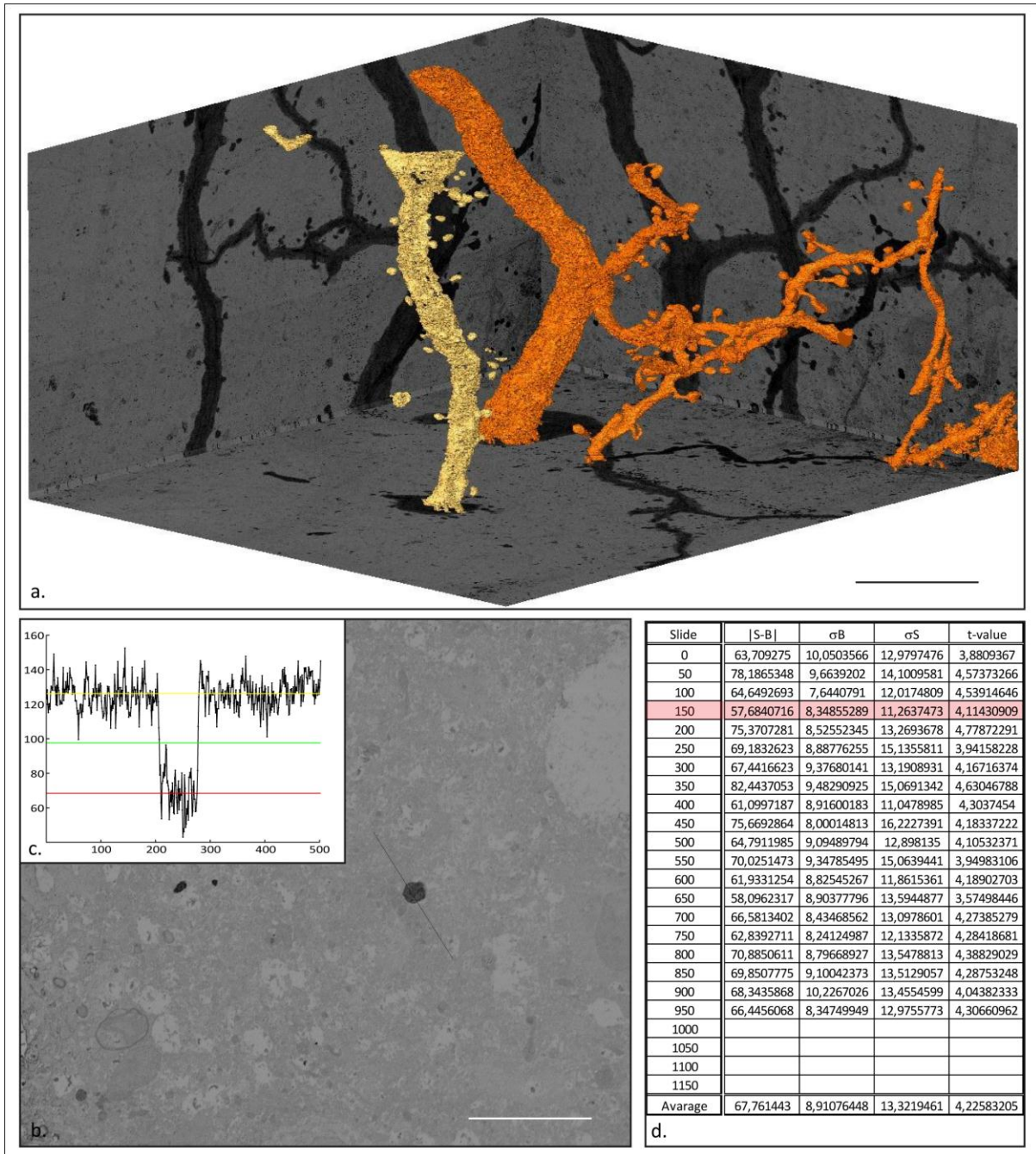


Figure 3.21: Dataset TK091110B_st003_10 (yellow); (a.): X-Y-Z-projection with reconstruction, the dataset consists of 1000 images which corresponds to a physical size of $30\mu\text{m}$ in Z, 20 cross sections were analyzed for contrast distribution; (b.): cross section with measure line; (c.): grey value plot of measure line in (b.), signal mean S (red), threshold (green), background mean B (yellow); (d.): $|S-B|$, σ_B , σ_S , and t-values for every single evaluated cross sections of the dataset, values of the cross section shown in (b.) and (c.) are shaded in red; scale bar = $10\mu\text{m}$.

Average values of this data stack were: $|S-B| = 68$, $\sigma_B = 8.9$, $\sigma_S = 13.3$, $t = 4.226$.

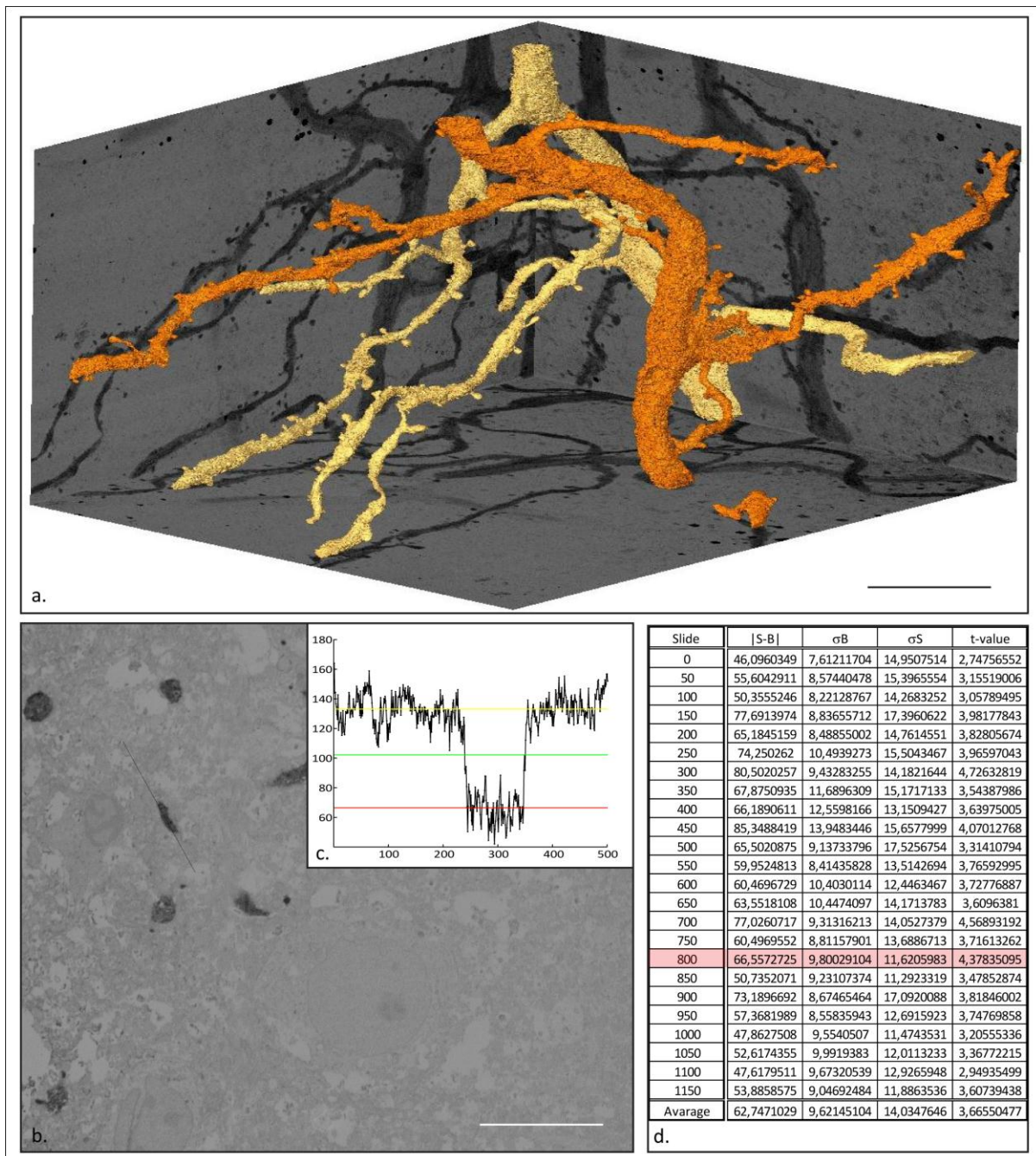


Figure 3.22: Dataset TK091110F_st001_11 (yellow); (a.): X-Y-Z-projection with reconstruction, the dataset consists of 1176 images which corresponds to a physical size of $35.28\mu\text{m}$ in Z, 24 cross sections were analyzed for contrast distribution; (b.): cross section with measure line; (c.): grey value plot of measure line in (b.), signal mean S (red), threshold (green), background mean B (yellow); (d.): $|S-B|$, σ_B , σ_S , and t -values for every single evaluated cross sections of the dataset, values of the cross section shown in (b.) and (c.) are shaded in red; scale bar = $10\mu\text{m}$.

Average values of this data stack were: $|S-B| = 63$, $\sigma_B = 9.6$, $\sigma_S = 14$, $t = 3.666$.

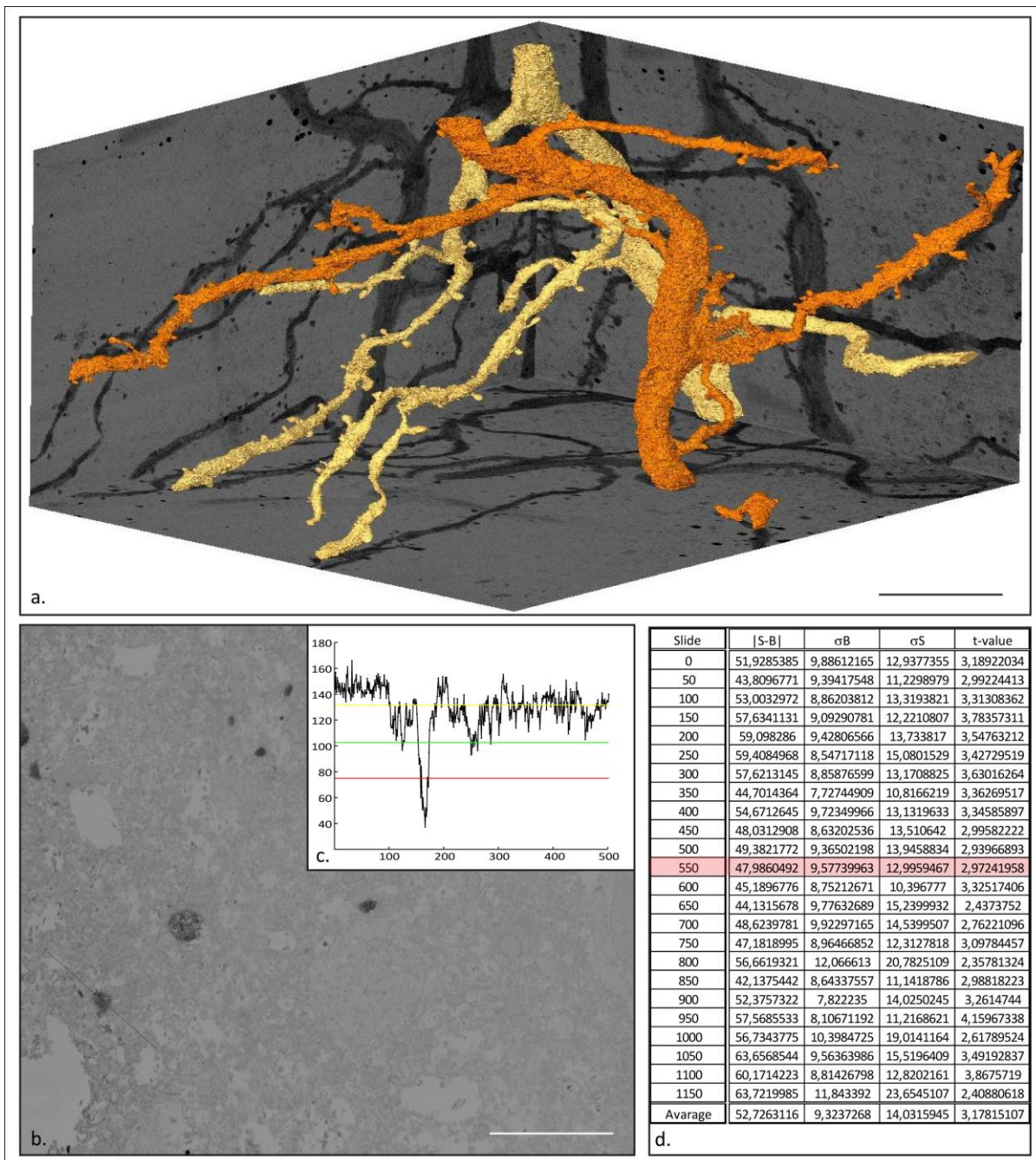


Figure 3.23: Dataset TK091110G_st001_11 (orange); (a.): X-Y-Z-projection with reconstruction, the dataset consists of 1176 images which corresponds to a physical size of $35.28\mu\text{m}$ in Z, 24 cross sections were analyzed for contrast distribution; (b.): cross section with measure line; (c.): grey value plot of measure line in (b.), signal mean S (red), threshold (green), background mean B (yellow); (d.): $|S-B|$, σ_B , σ_S , and t-values for every single evaluated cross sections of the dataset, values of the cross section shown in (b.) and (c.) are shaded in red; scale bar = $10\mu\text{m}$.

Average values of this data stack were: $|S-B| = 53$, $\sigma_B = 9.3$, $\sigma_S = 14$, $t = 3.178$.

However, this method of auto-thresholding is only applicable for data that can be separated by a simple threshold. In comparison, a data stack of a sample stained with an alternative staining protocol (Seligman et al, 1966), was impossible to automatically segment due to

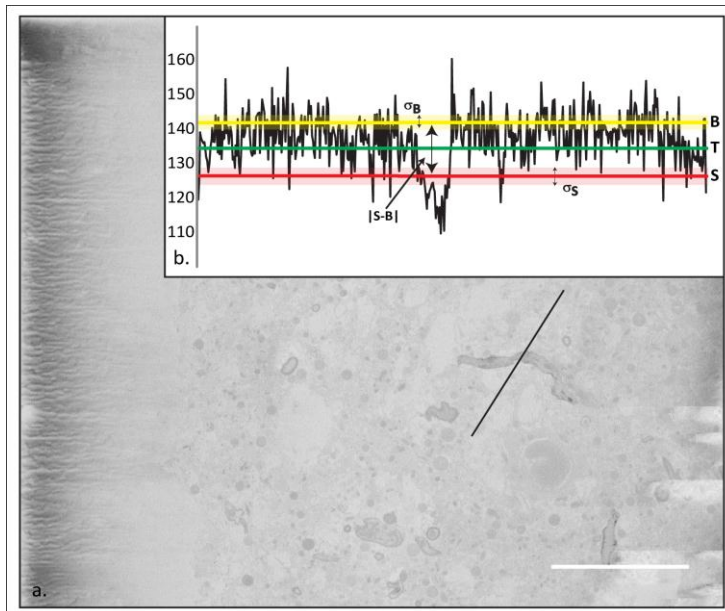


Figure 3.24: (a.): cross section of non-segmentable dataset; (b.): plotted grey value profile of black line in a., Measurements for this section: $|S-B|=12$, $\sigma_S=4$, $\sigma_B=5$, $t=1.8$; scale bar = $10\mu\text{m}$.

weak contrast (average $|S-B|=15$), resulted in $t = 1.93$. Figure 3.24 shows a cross section from this dataset with the automatically calculated T, S, B and their standard deviations. Due to the missing contrast, the background pixels could not be discriminated by a threshold, which therefore renders the calculated values inadequate. Even though the t-values are invalid, they do reflect that a higher t-value is a good indication of the higher quality of

the staining and therefore better segmentation properties. It can further be deduced, that between $t = 2$ and 3 is the cutoff value for a feasible segmentation (see values in Table 3.1).

The analysis of a total of 164 cross sections from 10 individual neurons revealed that the staining protocol is very reproducible (Figure 3.14 – Figure 3.23). Table 3.1 summarizes the evaluation data. The average $|S-B|$ over all datasets is 53 gv. The average standard deviations of signal and background are $\sigma_S = 12$ gv and $\sigma_B = 8$ gv, respectively. The average t-distribution for these datasets is $t = 3.77$. In contrast, the values of the non-segmented dataset are very different ($t = 1.93$). This supports the observed finding that the lower the t-value, the more segmentation refinement is required to determine the necessary variables to sufficiently segment the data stack and vice versa.

3.1.3.2 Contrast Confirmation in other Electron Microscopes

As scanning in the SBFSEM is very time consuming (up to weeks and months of recording stacks), additional samples were screened in different electron microscope systems for comparative purposes. The samples were also stained with the OsO_4 and lead citrate staining protocol described above. For the SEM and SBFSEM only the surface was scanned while ultra-thin sections were cut from the sample block for TEM.

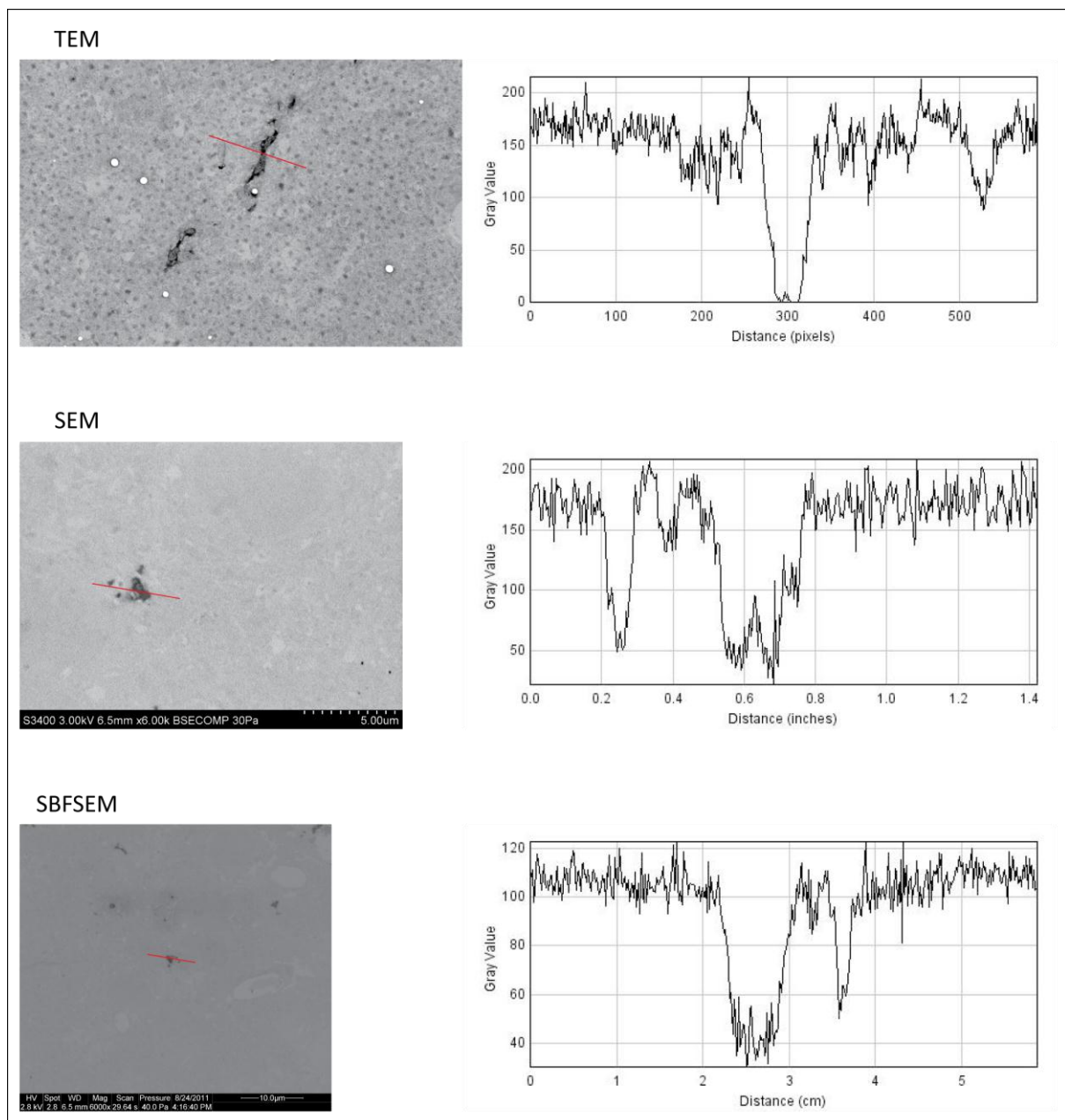


Figure 3.25: Comparison of one and the same sample in TEM, SEM, and SBFSEM. The contrast tendency of being $\text{TEM} \gg \text{SEM} > \text{SBFSEM}$ is clearly visible. The sample is representative of another 17 samples showing the same tendencies.

Neuronal structure could not be clearly identified in all samples in the SEM. This might be a result of three reasons: (i) no structure was stained, (ii) no structure was present on the sample's block-face or (iii) a cut dendrite in 2D might look like a metal precipitate and therefore cannot be distinguished. Neuronal structure could be identified in 18 out of 28 samples. For all 18 samples, the contrast tendencies were similar and as illustrated in Figure 3.25. Naturally, the contrast in TEM was much higher than in any SEM. However, the detector in the SEM gave higher contrast when compared to the SBFSEM. Whilst the contrast in the TEM was almost saturating the 8-bit scale of 256 gray values, the contrast was still very high in the SEM (>100gv). In comparison, with 40-60gv, the SBFSEM's contrast was quite moderate, but comparable to the results of the stack recordings shown in section 3.1.3. Screening samples prepared and stained with this protocol in electron microscope systems other than the SBFSEM resulted in two findings. First, the screen showed that all identified structures displayed adequate and comparable contrast in all systems. The contrast of the filled neuron is extremely high in the TEM, which seems to be necessary to have sufficient contrast in the SBFSEM. Secondly, as dendritic structure could only be identified in 18 out of 28 samples, this kind of screening method, albeit fast, is not suitable for determining if the staining worked or not. The probability of not finding stained dendrite structures at the initial observation is quite common for this type of staining in the SBFSEM. In many cases, only acquiring image stacks and analyzing the course of the contours and distinctly dark structures, reveals the stained dendrites. Another possibility for scans lacking structures of the desired neuron is that the scanning face is still in the "empty tissue buffer" (tissue below the dendrites of the stained neuron). As all stained samples from which image stacks were recorded in the SBFSEM and two-thirds of the surface scans discussed in this chapter, showed suitable staining of the filled neuron, it is unlikely that a failed staining procedure can account for samples in which only the surface was scanned and no structure could be identified. In the end, only the acquisition of image stacks in the SBFSEM can lead to the clear identification of a dendrite of the filled neuron and therefore to the conclusion that the staining has worked or not.

In summary, the OsO₄ and lead citrate staining protocol provides reproducible, specific and intense contrast to the biocytin-filled and DAB stained neurons without significantly increasing the contrast of the neuropil.

3.2 Validation of NeuroStruct

The segmentation toolbox used in this study from which all reconstructions were created is NeuroStruct. The algorithms were developed by Stefan Lang and colleagues (Lang et al, 2011b), but the toolbox was further improved and validated in this study. All data shown in this section was created, evaluated and analyzed in cooperation with Dr. Panos Drouvelis (Drouvelis et al, 2012). This chapter describes new and extended tracing filters within NeuroStruct and validates the preciseness of the toolbox by focusing on fine and important neuronal structures such as spines and their necks. The computational pipeline is evaluated on a segment of an apical dendrite from a single biocytin-filled L5B pyramidal neuron of the mouse's barrel cortex and the traced neuronal structure is validated with reference tracings generated by human tracers in both the image (binary images of the tracings) and object space (3D reconstructions). Here, we quantify the degree of human ambiguity in the completeness of the manual tracings, and show the reliability of Neurostruct's automated reconstruction down to the smallest morphological details.

3.2.1 Datasets used for the Validation

Different datasets were created from one original SBFSEM dataset (label: TK100909A1_st011_3). This chapter describes briefly how they were created. A schematic overview on the inheritance of the data stacks discussed here is outlined in Figure 3.26.

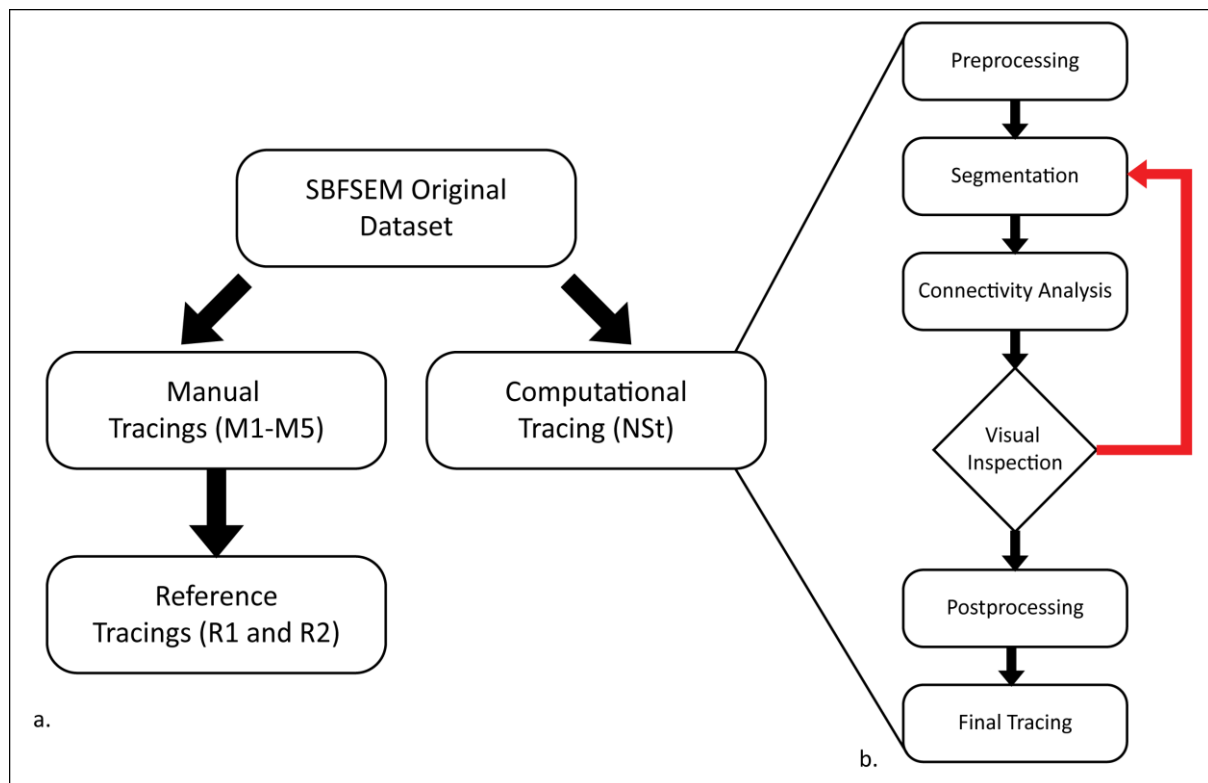


Figure 3.26: (a.): Flow chart of the relation of the tracings used in this study; (b.): workflow of the NeuroStruct pipeline: preprocessing, segmentation, and connectivity analysis, of the neuronal structure. After iterative application of the pipeline for various parameters, the best result is selected manually via spine completeness and surface structure.

3.2.1.1 SBFSEM Original Dataset

The original SBFSEM dataset, from which all other datasets that were used for validation are derived, was a sub-stack of image stack TK100909A1_st011_3 that was already shown in Figure 3.16. For handling reasons, only regions containing structural information were cropped, leaving an image stack of 502x704 pixels and 846 images (Table 3.2). The data stack was chosen because it represents several challenging issues for both manual and automatic segmentation: (i) the dendritic backbone bore over 100 dendritic spines in a large

HV	2.8
Spotsize	2.8
Image pixel X	502
Image pixel Y	704
Images/Stack Z	846
Voxel Volume [Megavoxel]	298.98
Pixel resolution X [nm]	24.4
Pixel resolution Y [nm]	24.4
cutting size Z [nm]	30
Image size X [μm]	12.25
Image size Y [μm]	17.18
Stack thickness Z [μm]	25.38
Stack Volume [μm^3]	5340.08

Table 3.2: Properties of the data stack TK100909A1_st011_3 used for validation of NeuroStruct.

morphological variety, with and without connections to the dendritic backbone, (ii) the data stack consisted of 846 images which is a sizeable piece of serial electron microscopic data and (iii) due to the dendritic length and the number of spines the density of spines/ μm was remarkably high (~ 4 spines/ μm). This high density resulted in artificial loops in the later segmentation due to two reasons. Firstly, if two (or more) spine heads were in too close a proximity to each other for the SBFSEM to resolve the different structures, these structures created loops in 3D. Secondly, 3D loop structures were created by segmentation errors. Those loops occurred in automatic and manual reconstructions alike.

3.2.1.2 Manual Tracings

The basis for the validation of the computational method were five manual tracings (MTs) generated by five individuals, independent of each other using OpenCar (<http://opencar.ulster.ac.uk/>; (Rollenhagen et al, 2007; Saetzler et al, 2002)). Each individual was given the entire SBFSEM image dataset. The individual subjectively drew contours, surrounding what they thought to be part of the stained neuron in every image. After completing the whole image stack, the contour files were anonymized by assigning a random number (M1-M5) to each tracing. The contours of each image were exported into binary images also by using OpenCar. These contours were analyzed and compared with the computational tracing to quantify the degree of variability and objectivity of the human segmentations (see Figure 3.27(a.), (c.), and (e.))

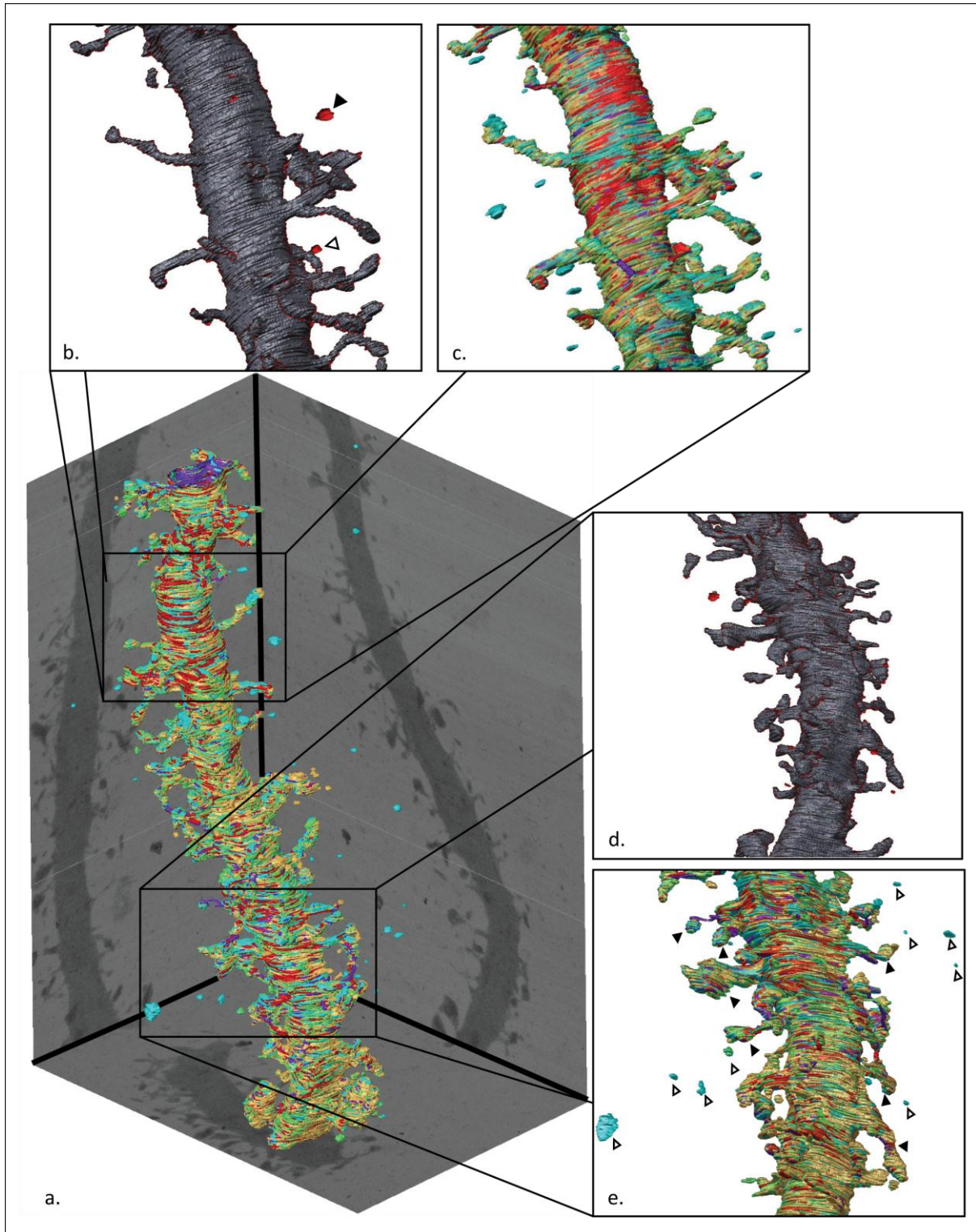


Figure 3.27: Comparison of the manual (M1-M5) and reference reconstructions (R1 and R2). (a.): Overlay of all 5 MTs (each with a different color), surrounded by the 3D minimum intensity projections of the original SBFSEM image stack; magnified reconstruction overlays from two different domains: (b.) and (d.): R1 (dark gray) and R2 (transparent red) (c.) and (e.): all 5 MTs (each a different color). Filled and hollow arrowheads provide examples of respective true and false objects.

3.2.1.3 Reference Tracings

From these five MTs, two reference tracings, R1 and R2, were extracted. R1 uses a weak majority pixel selection, declaring a pixel as foreground, if three out of five MTs defined this pixel as foreground. This selection allows for a stronger variability of the final tracing, since more features from the MTs are allowed to be present. R2 represents a strong majority as a pixel is declared as foreground if four out of five manual tracers defined this pixel as foreground. This reference is more stringent with respect to the feature variability inherited from the MTs (see Figure 3.27(b.) and (d.)).

3.2.1.4 NeuroStruct Reconstruction (Nst)

The computational dataset was filtered as described in chapter 2 (Materials and Methods). The final reconstruction that was validated against the reference datasets is referred to as NSt. To check for the completeness of true objects in this tracing ($\eta_s = 24$), two further reconstructions are discussed later: one being more stringent (NSt^+ ; $\eta_s = 26$) and the other, more promiscuous (NSt^- ; $\eta_s = 22$). The reconstruction of the dendritic stem as well as the parameters for the connectivity filter remain unchanged ($\eta_d = 31$; $R = 60$; $V = 600$). Figure 3.28(a.) shows the tracing NSt, which is used for validation with the manual tracings, embedded in the minimum intensity projections of the gray-scale image space. The enlargements (b.-e.) show magnified overlays of tracings computed with the different parameters.

Dataset	True objects	False Objects			Loops		
		Positive	Negative	Total	Positive	Negative	Total
NSt^- (R1)	107	0	9	9	13	9	22
NSt^- (R2)	107	0	9	9	9	13	22
NSt^- (NSt)	107	5	4	9	16	6	22
NSt^+ (R1)	100	0	0	0	11	2	13
NSt^+ (R2)	100	0	0	0	8	5	13
NSt^+ (NSt)	100	0	0	0	13	0	13

Table 3.3: Robustness results at the object space regarding the selection of the parameter $\eta_s = 22$ (dataset NSt^-) and $\eta_s = 26$ (dataset NSt^+). In brackets are the datasets R1, R2 or NSt, which are serving as reference.

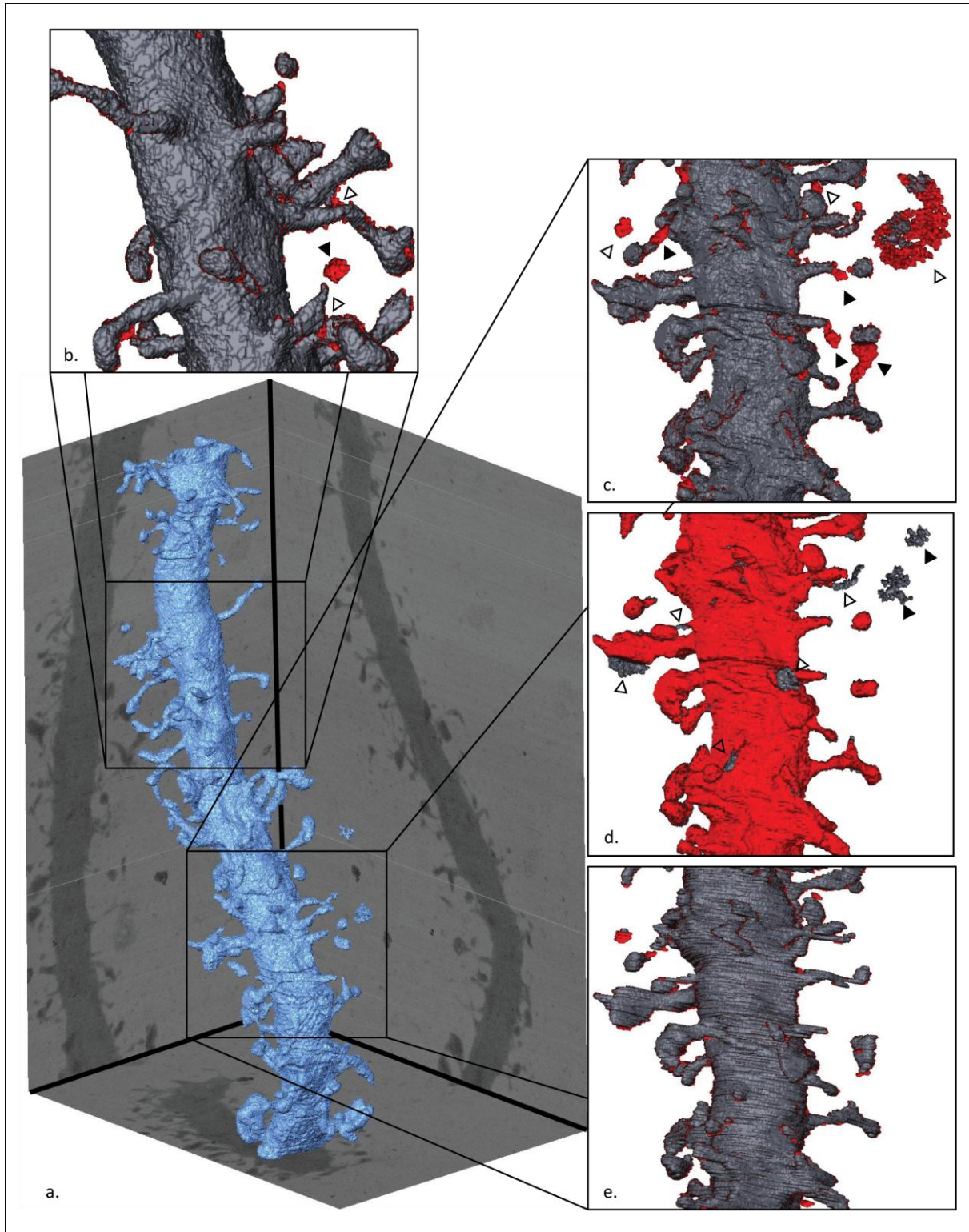


Figure 3.28: Comparison of the computational reconstructions NSt vs. NSt^+ and NSt^- . (a.): NSt reconstruction surrounded by the 3D minimum intensity projections of the original SBFSEM image stack; magnified reconstruction overlays; (b.) and (c.): NSt (dark) and NSt^+ (transparent red); (d.): NSt (transparent dark) and NSt^+ (red); (e.): $R1$ (dark) and $R2$ (transparent red); (c.), (d.), and (e.): are the same perspective; filled and hollow arrowheads indicate true and false objects, respectively.

3.2.2 Validation Results

3.2.2.1 Reference Tracings

R1 contains one dendrite and 106 spines, either attached or in close proximity of the dendritic stem, which resembles the reference number of true objects. In addition to these referential true objects, six false objects and 20 loops were also generated. In comparison, the stricter reference dataset R2 provides one dendrite, 105 spines, one false object and 15 loops. Comparing the volumes of both datasets, R1 (4,994,244 voxels/ 93.64 μm^3) is 5.2% larger than R2 (4,734,906 voxels / 88.78 μm^3). Data and findings are summarized in Table 3.4.

Dataset	True objects	False objects	Loops	Volume (voxels)	Volume (μm^3)
R1	106 spines	6	20	4,994,244	93.64
R2	105 spines	1	15	4,734,906	88.78

Table 3.4: Quantitative findings for R1 and R2 datasets at the object and image space.

3.2.2.2 Comparison of the Computational Tracing (NSt) and the Manual Tracings (MTs) to Reference Tracings R1 and R2

3.2.2.2.1 3D Object Space Analysis

Table 3.5 summarizes the results of the quantitative analysis for both the manual and NSt 3D reconstructions using R1 as a reference: NSt, M1, M3 and M4 found all true objects - M2 and M5 missed one and three spines, respectively. Large deviations are observed in the number of false objects discovered by the MTs. The NSt traced zero R1 positive and five R1 negative false objects. One of these false R1 negative objects is M1 positive. All tracings present a number between 12 and 18 loops. Remarkably, M3 did not trace any R1 negative loops. Table 3.6 summarizes the results in the object space using R2 as a reference. R2 missed one

true object due to the stricter foreground pixel selection rule. The statistical weight of tracings M2 and M5, which are missing one and three true objects respectively, dominates this dataset.

Dataset	True objects	False Objects			Loops		
		Positive	Negative	Total	Positive	Negative	Total
M1	106	6	41	47	11	7	18
M2	105	1	0	1	7	5	12
M3	106	6	96	102	12	0	12
M4	106	4	16	20	14	3	17
M5	103	0	0	0	14	1	15
$\bar{M} \pm \delta M$	105.2 ± 0.6	3.4 ± 1.2	31 ± 18	34 ± 19	11.6 ± 1.3	3.2 ± 1.3	14.8 ± 1.2
NSt	106	0	5	5	12	4	16
R1	106	6	0	6	20	0	20

Table 3.5: Quantitative validation results of NSt in comparison to the MTs with respect to R1 (weak majority) regarding the object space.

Dataset	True objects	False Objects			Loops		
		Positive	Negative	Total	Positive	Negative	Total
M1	106	1	46	47	6	12	18
M2	105	1	0	1	6	6	12
M3	106	1	101	102	9	3	12
M4	106	1	19	20	11	6	17
M5	103	0	0	0	9	6	15
$\bar{M} \pm \delta M$	105.2 ± 0.6	0.8 ± 0.2	33 ± 19	34 ± 19	8.2 ± 1.0	6.6 ± 1.5	14.8 ± 1.2
NSt	106	0	5	5	9	7	16
R2	105	1	0	0	15	0	15

Table 3.6: Quantitative validation results of NSt in comparison to the MTs with respect to R2 (strong majority) regarding the object space.

3.2.2.2.2 Image Space Analysis

At the image (voxel) space, the manual tracings calculate the R1 false positive volume (1.1% V(R1) as 7.4% V(R1)), and the R1 false negative volume (1.3% V(R1) as 7.9% V(R1)) to the same extent. The NSt's volumes are comparable to these values (2.3% V(R1) R1 positive voxels and 7.9% V(R1) R1 negative) (Table 3.7). MTs show a mean value of false R1 positive voxel deficit (3.6 ± 1.0)% V(R1), that is balanced by a (4.1 ± 1.1)% V(R1) false R1 negative surplus. The voxel volumes of the computed tracing (NSt) show a minimal deviation from the

predicted statistical error of the $\bar{M}(R1)$ positive volume ($\bar{M}+(R1)$) of just 0.3% $V(R1)$ and 2.7% $V(R1)$ as predicted by the statistical error of the $\bar{M}(R1)$ negative volume ($\bar{M}-(R1)$). Furthermore, we estimate the volume deviations of the false objects of the datasets M1, M3 and M4 on the total volume of the segmented structure by rejecting all objects that are not within a certain distance R from the dendritic stem and that possess a volume larger than V . For $R = 60$ and $V = 600$ the volume differences between reference data and filtered manual data are very small (0.2%) (Table 3.7, last column). This result supports the observation that the voxel volume variability is contributed mainly by the dendritic stem, as has already been shown from the embracing voxel surplus in Figure 3.28(b.) and (d.). Table 3.8 shows the quantitative analysis of the image space using $R2$. The mean false positive volume ($\bar{M}+(R2)$) of all manual tracings converges to a difference of $(1.5 \pm 0.5)\% V(R1)$, which is half ($\bar{M}+(R1)$). This results from the stricter selection criteria, which led to less variation in the shape of the foreground structure. As a consequence, the deviation of the volume $\bar{M}-(R2)$ is with $(7.2 \pm 1.6)\% V(R1)$ almost twice the value of $\bar{M}-(R1)$. The volume deviations for each tracing, however, do not significantly differ from the analysis of $R1$.

Dataset	False Volumes			
	Positive	Negative	Balanced ($V(\text{Pos})-V(\text{Neg})$)	False Objects ($R=60; V=600$)
M1	1.1	7.9	-6.8	0.3
M2	7.4	1.3	6.1	0
M3	3.5	3.3	0.2	0.7
M4	2.9	4.7	-1.8	0.2
M5	3.1	3.2	-0.1	0
$\bar{M} \pm \delta M$	3.6 ± 1.0	4.1 ± 1.1	-0.5 ± 2.1	0.24 ± 0.13
NSt	2.3	7.9	-5.6	0.2
R1	0	0	0	≈ 0.01

Table 3.7: Quantitative validation results of NSt in comparison to the MTs with respect to $R1$ (weak majority) at the image space. All values are given as $\%V(R1)$.

Dataset	False Volumes			False Objects (R=60; V=600)
	Positive	Negative	Balanced (V(Pos)-V(Neg))	
M1	0.3	12.33	-12.03	0.3
M2	3.53	2.69	0.84	0
M3	1.28	6.32	-5.04	0.8
M4	1.3	8.36	-7.06	0.2
M5	1.03	6.36	-5.33	0
$\bar{M} \pm \delta M$	1.5 ± 0.5	7.2 ± 1.6	-5.7 ± 2.1	0.26 ± 0.15
NSt	1.01	11.82	-10.81	0.2
R2	0	0	0	≈ 0.0

Table 3.8: Quantitative validation results of NSt in comparison to the MTs with respect to R2 (strong majority) at the image space. All values are given as %V(R2).

3.2.2.3 Quantification of the Tracing's Accuracy

To obtain a clearer perspective of the quality of the tracings, we quantified the results of all tracings in both the object and the image space and validated them against both R1 and R2. For this purpose, the relative error of each tracing's finding (manual and computed) was calculated in regards to the reference. In the object space we used five categories: true objects, false positive, false negative, loops positive and loops negative. Especially for the categories of the negative artifacts (false objects and loops), which by definition was zero items for RT, we defined the relative error with respect to M3 (MT with the most negative objects) and M1 (MT with the most loops). At the image space, the false positive and false negative volume deviations were used as a metric. Taking all seven categories (total object and image space categories) into account resulted in a ranking for all tracings, shown in Figure 3.29(a.) and (b.) for R1 and R2 as a reference, respectively. In all three spaces (object, image and combination of both) the relative errors of all tracings cluster and no large deviations are observed. We conclude that our computational approach (NSt) provides a reliable and high quality reconstruction, which matches and in some parameters even outperforms the quality of the manual reconstructions.

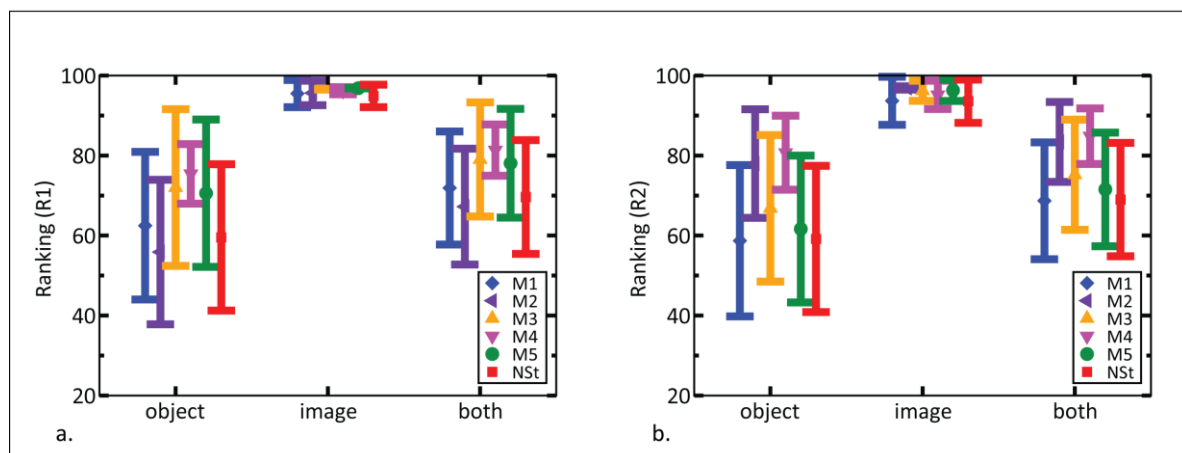


Figure 3.29: Ranking of the M1-M5 and NSt tracings with respect to R1 (a.) and R2 (b.) tracings in the object, image and combined (both) image and object space. The bars are slightly shifted in order to be visually distinguished.

3.3 Application of the Staining Protocol and NeuroStruct

Commonly used techniques to quantitatively investigate neuronal morphologies such as dendritic spines are usually performed with light microscopy. If EM is applied, only small data stacks (of some 10s of μm in z) are acquired and analyzed in standard EM (such as serial transmission or scanning electron microscopy (ssTEM and sSEM)) as this is very labor-intensive and error-prone. As shown in the previous chapters a specific staining protocol that only stains single – biocytin filled neurons was developed, established and reproduced for numerous samples. Together with the SBFSEM and the extendable toolbox NeuroStruct, it was possible to obtain quantitative data from single neurons and extract their morphological information at nanoscale resolution.

3.3.1 Reconstruction of an entire L5B Neuron

To demonstrate the power of these tools, an almost complete L5B neuron from the mouse barrel cortex (S2) was recorded in the SBFSEM and reconstructed with NeuroStruct. The neuron was filled in a specific genetically modified mouse line that expresses GFP under the cell specific promoter *GLT25b 2* (GLT) (Groh et al, 2010). As Groh et al. describe, GLT is only expressed in the soma of a specific subset of L5B neurons, which allows for targeting of these cells in the patch setup (Figure 3.30(a.) and (b.)).

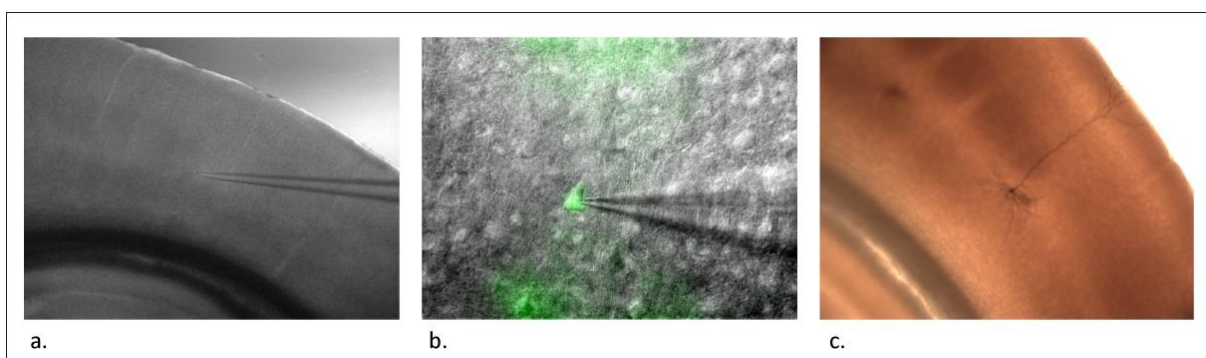


Figure 3.30: GLT-L5B Neuron TK100909A1: (a.): Slice overview with patch pipette; (b.): overlay of DIC- and GFP-Channel identifying the patched neuron as GLT; (c.) DAB stained neuron.

3.3.1.1 Staining and EM preparation

The neuron was filled with biocytin and stained with DAB (Figure 3.30(c.)). After cutting out the stained structure in a trapezoid block, the tissue was contrasted with OsO₄ and lead citrate. The resulting pitch-black block was mounted on a steel pin with the basal dendrites facing upwards; hence the cell was cut and scanned towards the pia mater following the apical dendrite. Details can be found in chapter 2 (Materials and Methods).

3.3.1.2 Scanning Results

The steel pin bearing the contrasted neuron was put into the SBFSEM and oriented parallel to the back-scattering electron (BSE) detector. The microscope was set to low vacuum and the pressure was set manually to 30 mbar by a needle valve. When the pressure stabilized in the chamber (>12 hours), focus, lens alignment and astigmatism were optimized and images were acquired using a spot size of 2.8 and an electron beam energy of 2.8 keV. The surface was scanned in mosaic tiles to cover the area where stained structures were visible. The mosaic was manually adjusted over time to prevent the structure from leaving the scanning range. This resulted in mosaic scans from 2x2 up to 13x5 tiles. The tiling was optimized to be as small as possible due to time constraints with every image and every cut of the sample (30nm) taking approximately 1 min. In practice, this means that 30 nm in depth take between 6 min. and 66 min. for the mentioned mosaics, respectively. The lateral magnification was 6000x for all images (resolution: ~24x24nm pixel size) and the physical coverage of one field of view was ~49.2x42.4µm (2048x1768pixel). The mosaic tiles were recorded with an overlap of ~2%, so that the resulting segmented structure could be properly aligned. The following Figure 3.31 - Figure 3.35 show minimum z- projections for every usable image stack recorded from this sample. 9 out of 41 stacks were not used for segmentation either because they did not contain any data or technical problems like too much electrical noise or too much debris rendered them unusable. These 9 image stacks contain 237 images (7.11µm) in total, which corresponds to only 1.2% of the total longitudinal length (615.42µm).

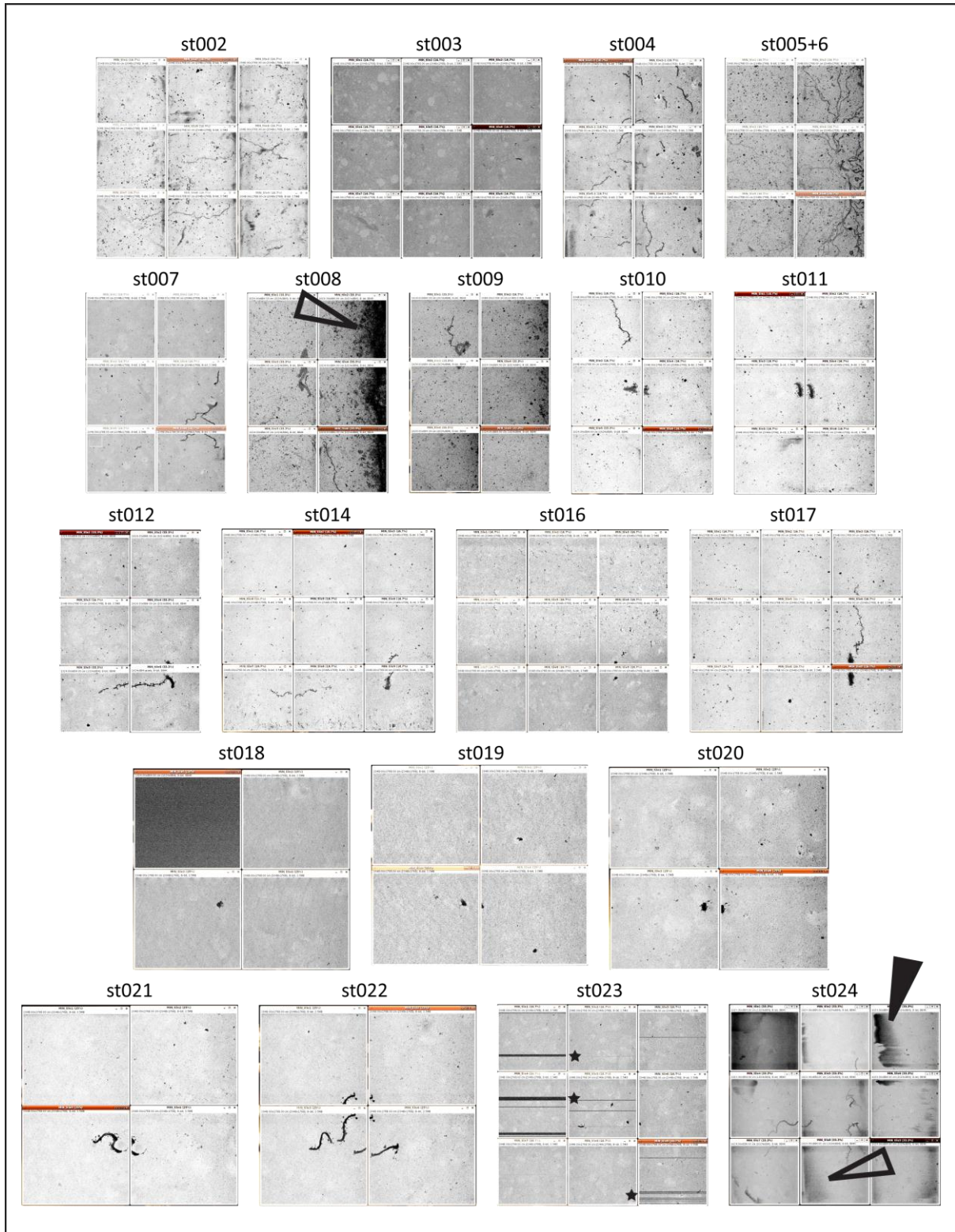


Figure 3.31: Minimum Z-Projections of TK100909A1_st001-st024: note that st008 and st009 show high charging of the right border (hollow arrowheads). This charging is typical for the sample's border as there is no conductive material there. Charged areas could usually be cropped away. Also note st023; black bars in the Z-projections due to electrical noise in sporadic images (stars). In st024 large black areas and smear are visible due to charging (hollow arrowhead) and debris (filled arrowhead), respectively; scale: 1 tile = 49.2x42.4 μ m.

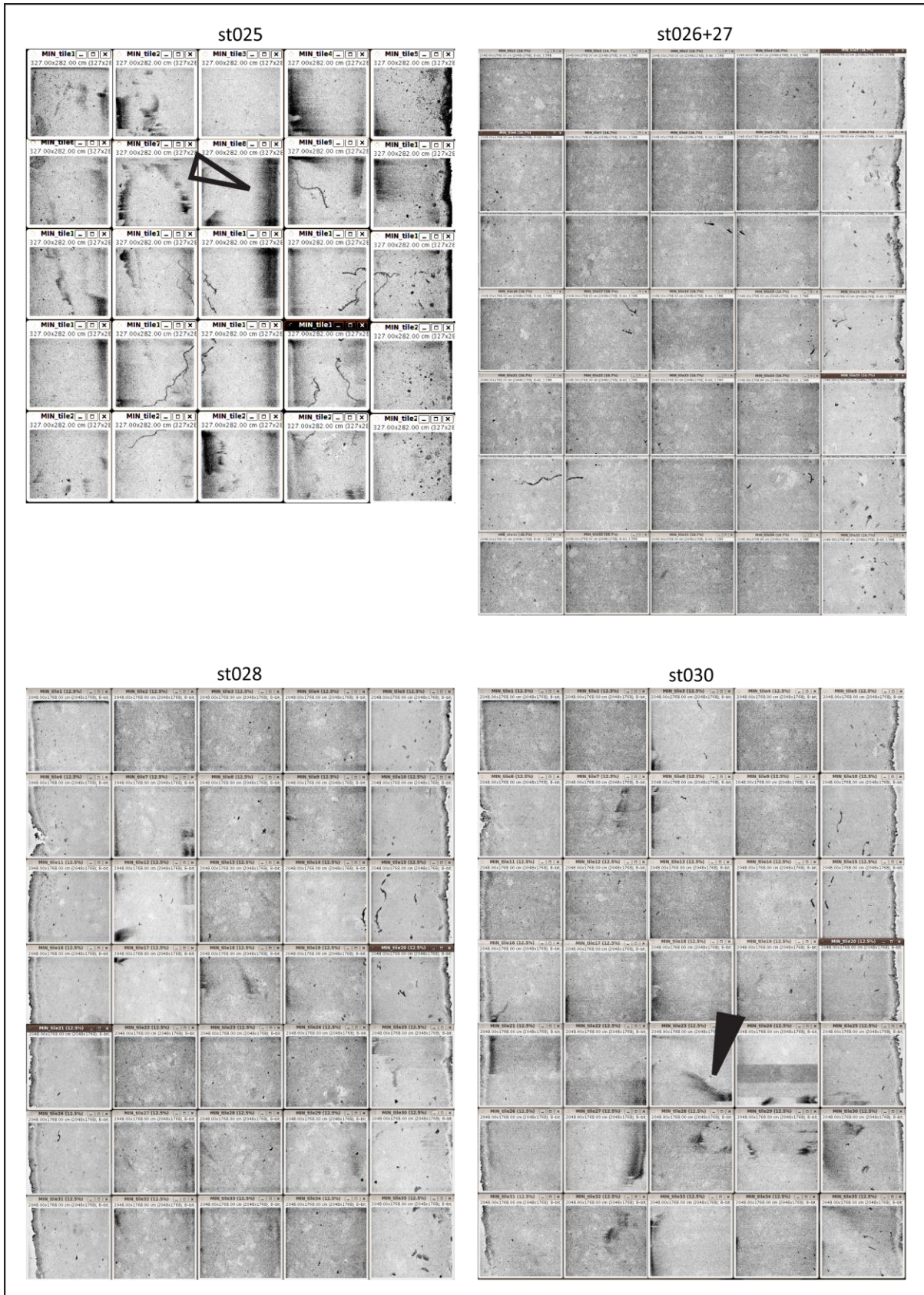


Figure 3.32: Minimum Z-Projections of TK100909A1_st025-st030. Black borders in some tiles are a result of charging (st025_8, hollow arrowhead), black smear (e.g. st030_23; filled arrowhead) due to debris; scale: 1 tile = 49.2x42.4 μ m.

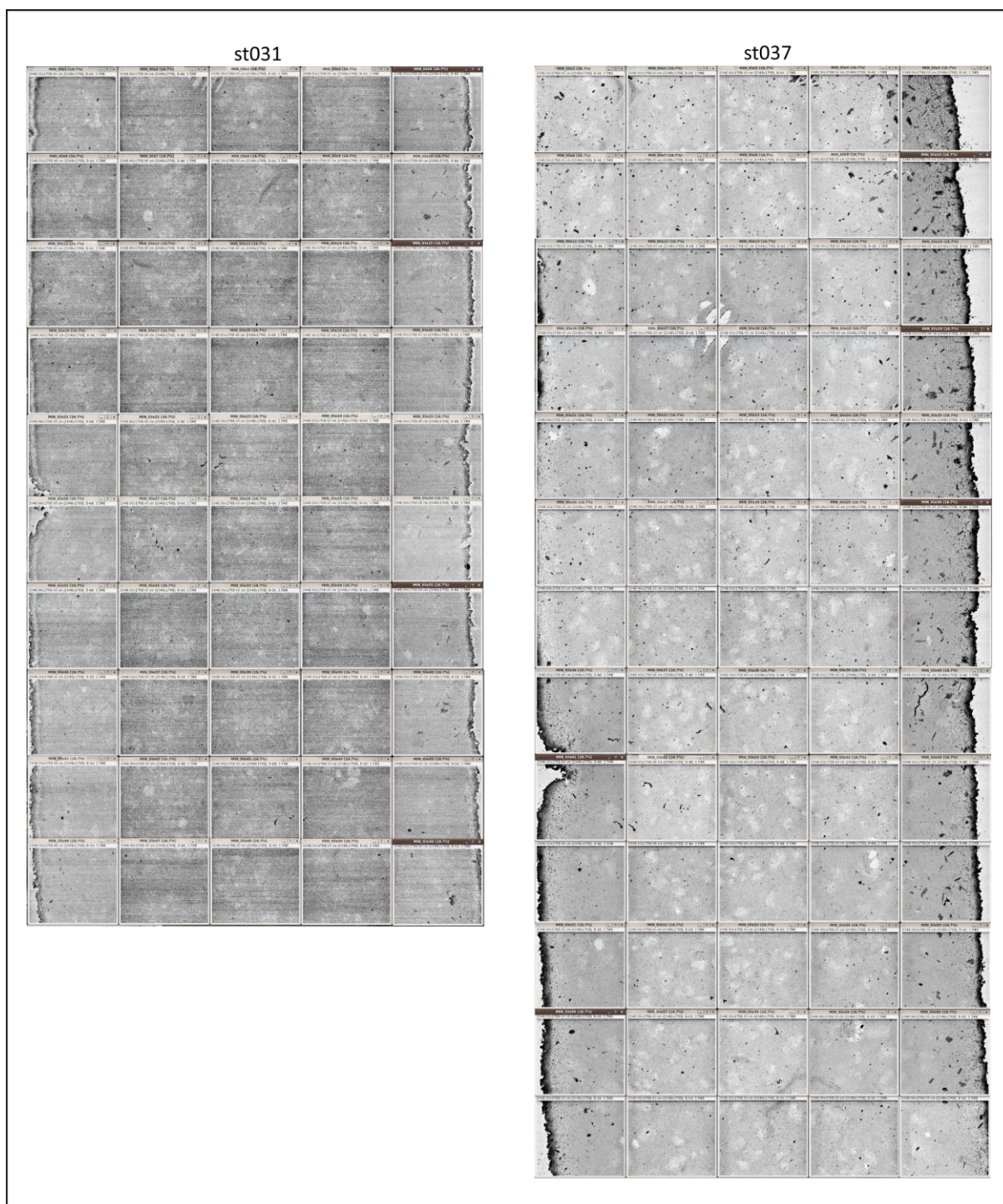


Figure 3.33: Minimum Z-Projections of TK100909A1_st031 and st037; scale: 1 tile = 49.2x42.4 μ m.

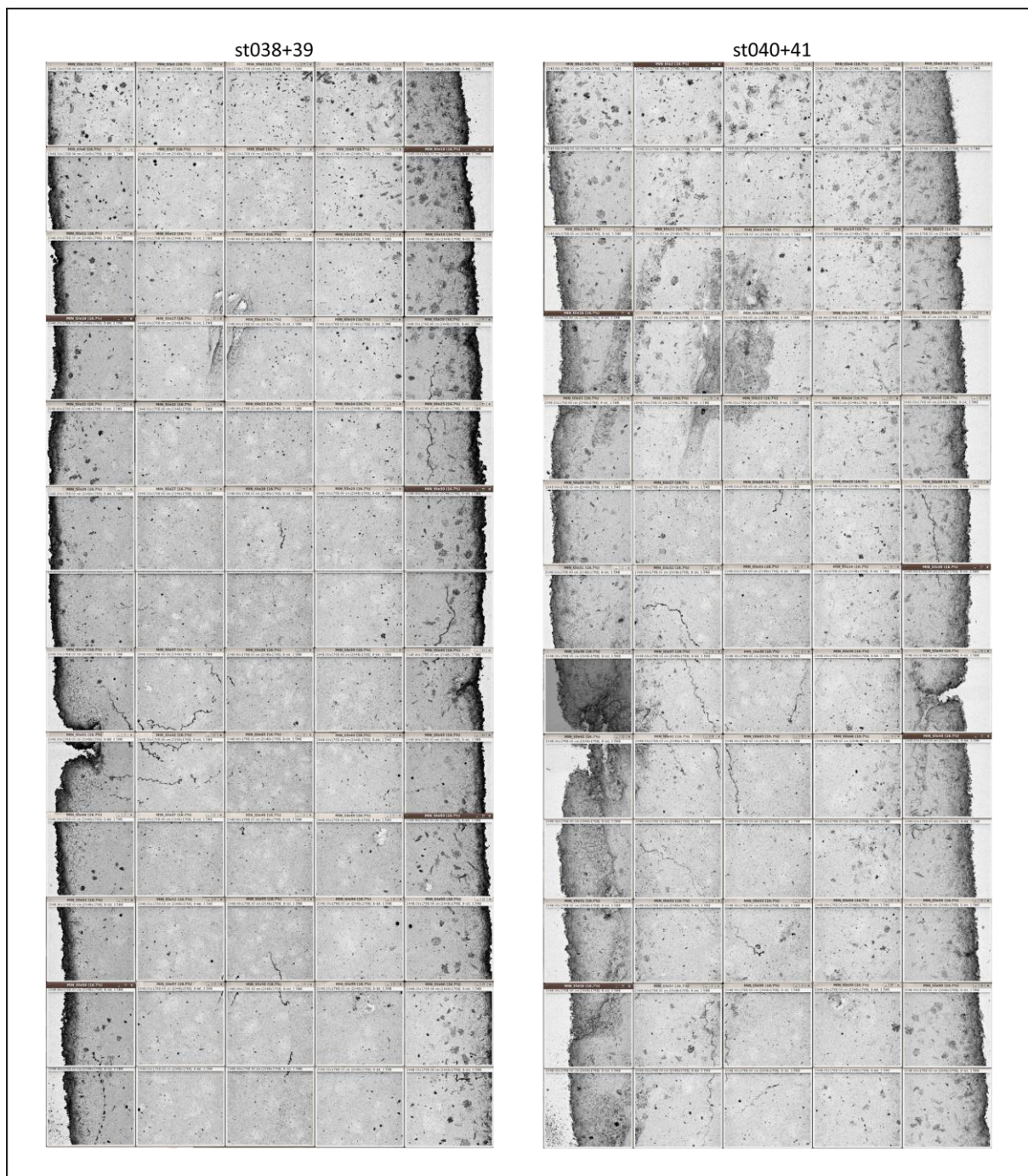


Figure 3.34: Minimum Z-Projections of TK100909A1_st038+39 and st040+41; scale: 1 tile = 49.2x42.4 μ m.

Stackname	Slices [images]	Physical Size [μm]
st002	947	28.41
st003	7	0.21
st004	281	8.43
st005+6	2327	69.81
st007	230	6.9
st008	3009	90.27
st009	1741	52.23
st010	859	25.77
st011	846	25.38
st012	674	20.22
st014	747	22.41
st016	64	1.92
st017	2332	69.96
st018	393	11.79
st019	271	8.13
st020	369	11.07
st021	367	11.01
st022	389	11.67
st023	115	3.45
st024	1268	38.04
st025	772	23.16
st0026+27	722	21.66
st028	50	1.5
st030	205	6.15
st031	74	2.22
st037	81	2.43
st038+39	495	14.85
st040+41	642	19.26
total	20277	608.31

Table 3.9: Summary of the amount of images and corresponding physical size (μm) in Z for every stack used for segmentation. Naturally, the number of images and therefore the physical height was recorded for every tile in the corresponding stack.

A total of 608 μm (longitudinal length) of one single biocytin-filled neuron was scanned and segmented with NeuroStruct. Table 3.9 summarizes the number of slices and the physical size for each stack. A stack was halted and a new stack was initiated for one of three reasons: (i) the SBFSEM malfunctioned due to technical reasons such as software crash or hardware issues, (ii) the structure was moving towards the tiling grid's border and therefore the mosaic had to be increased or (iii) by cutting down the trapezoid-shaped probe, the surface became too large for the knife to adequately cut. For point (i) it was generally sufficient to restart the computers, re-adjust scanning position, focus, lens settings etc. and initiate a new stack. For (ii) a new tiling was defined and the scanning position was verified for coverage of the desired area. For the third case (iii), the microscope chamber had to be vented, the sample removed from the holder, and the trapezoid was re-trimmed in an external microtome. After trimming, the sample was placed back in the holder and the microscope, vacuum was created and the orientation of the sample was checked for the correct angle (x/y) on the basis of the last

images taken. If the sample was incorrectly oriented, the chamber was vented again and the position was fixed with respect to the detector.

The pure calculated scan time of this dataset took approximately 240 days (24/7). Due to technical problems, however, the total duration was 282 days.

3.3.1.3 Segmentation and Reconstruction

Dendritic structure was present in 184 tile image stacks. Every tile stack was segmented individually. Debris on some single images sometimes resulted in a black smear on the z-projections, but usually did not interfere with the segmentation if restricted to a few images within the stack only. If necessary a sub-stack was cropped before segmentation. This was, for example, necessary for some stacks in the apical regions of the neurons (>st038) as the outer border of the brain (pia mater), was interfering with the segmentation. For visual inspection an isosurface was created in Amira and the best segmentation parameters were determined. The favored reconstructions were hence aligned and assembled in a 3D reconstruction of the neuron. Due to the rendering requirements for such a vast surface (amount of triangles), voxel-clouds of the outer face of the binary segmented .tiff files were used for assembly and representation. Figure 3.36 shows a bright field microscopy image of the DAB stained cell (see Figure 3.30(c.) for comparison), overlaid with the segmented reconstructions of all 184 voxel-clouds (white). Small yellow dots indicate landmarks of every spine. Five image stacks from different layers (L) are shown in enlargements as isosurface reconstructions: (i) a basal dendrite in L5B, (ii) the apical dendrite with a side branch in L4, (iii) the apical dendrite in lower L3, (iv) part of the apical tuft in upper L3 or lower L2, and, (v) part of the apical tuft in L1. Note the varying diameters and spine densities within the different types of dendrites. The dendritic tree of the L5B neuron has been more or less completely scanned and reconstructed, except for some basal dendritic branches in L5B. This is because the scanning grid chosen at the start was too small to cover the whole area

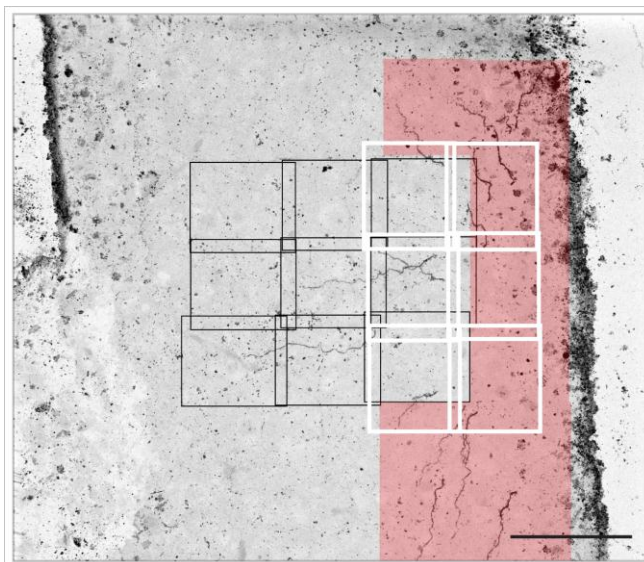


Figure 3.35: Minimum Z-projection after st003 showing missed branches in L5B: black scanning grid of st002 and st003; white scanning grid of st004; red area was missed because scanning area of st002 and 3 was too small; scale bar = 60µm

Figure 3.35). Note the varying diameters and spine densities within the different types of dendrites. The dendritic tree of the L5B neuron has been more or less completely scanned and reconstructed, except for some basal dendritic branches in L5B. This is because the scanning grid chosen at the start was too small to cover the whole area

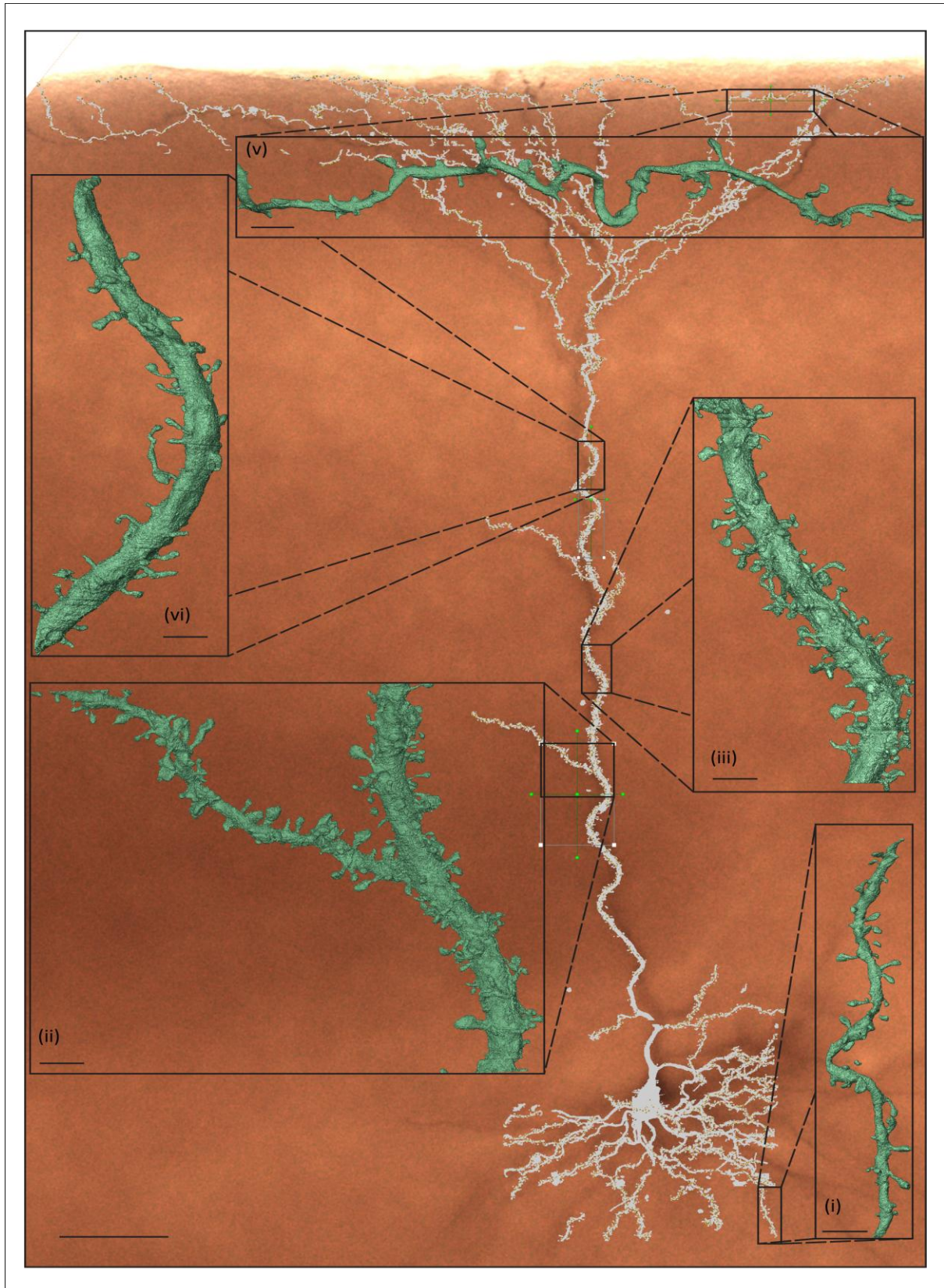


Figure 3.36: Reconstruction of TK100909A1: Assembly of 184 single reconstructions (white) overlay the DAB stained image; marked spines are slightly visible as yellow dots. Magnifications: (i) basal L5B dendrite; (ii) apical dendrite in L4, (iii) Apical dendrite in L3, (iv) Apical tuft in L1; (scale bars = $50\mu\text{m}$ in overview and $2.5\mu\text{m}$ in magnifications).

3.3.1.4 Spine Distribution of TK100909A1

Every spine was labeled as a landmark in the individual tile reconstructions in Amira. After assembly of the whole neuron, the local tile coordinates of these landmarks were transformed into global coordinates for the whole neuron. Thus, every spine had its own xyz coordinates within the neuronal reconstruction. Due to the overlapping of the scanning mosaic, some spines had been labeled twice and were subsequently removed. In the end, a total of 6672 spines remained. The global coordinates were imported into Matlab and the spine depth distribution was plotted according to the depth information. Figure 3.37 demonstrates this analysis. In (a.) the reconstructed cell and the underlying bright field image are shown. The DAB staining was used to assign the depth of the layers by contrast changes at the position of this specific cell (L1-L5B). The lower layer borders were defined as being 85, 185, 345, 465, 520 μm from the top for L1 to L5A, respectively. The deepest spine was marked at 614 μm . Subfigure (b.) shows the projection of the 6672 spine landmarks onto both the xz- and yz-plane. These landmarks were plotted according to their z-value (depth) and binned into both 5 μm bins (blue) and the layers (red) (c.). The quantification resulted in the following numbers of spines for the designated layers: L1: 1781 (27%), L2: 646 (10%), L3: 1060 (16%), L4 509 (8%), L5A 448 (7%) and L5B: 2228 (33%).

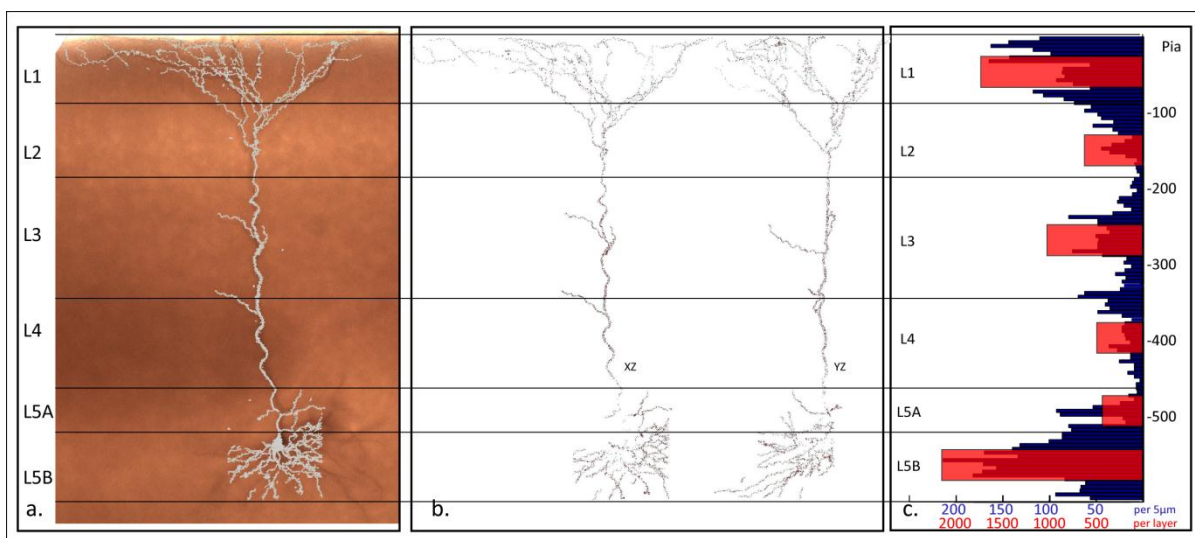


Figure 3.37: Spine distribution of the L5B (GLT) Neuron TK100909A1: (a.): bright field image with DAB-staining and overlaid reconstructed voxel clouds; the contrast of the image was the basis for the layer identification of the cell; (b.): landmarks of labeled spines as xz and yz projections; (c.): quantification of spines in 5 μm bins (blue) and layers (red).

3.3.2 Spinomics

After being able to specifically stain and extract the morphological information of a specific neuron, the next task was to automatically obtain single spine morphologies for characterization. Therefore, the NeuroStruct toolbox was further extended by Dr. Panos Drouvelis with a filter that serially walks through an image stack, detects spines and shaves them off the dendritic backbone (spine pruning). The filter was incorporated into the NeuroStruct workflow and is an extension, based on the submitted validation pipeline discussed in section 3.2. Briefly, the reconstruction of the largest components, that is dendrites with connected and proximally non-connected spine heads, are saved separately. From this dataset, the spines are shaved off iteratively leaving the pruned dendritic backbone. This backbone is then subtracted from the earlier RV-Connectivity filtered structure from which the spines were originally cut off. Without the backbone only the

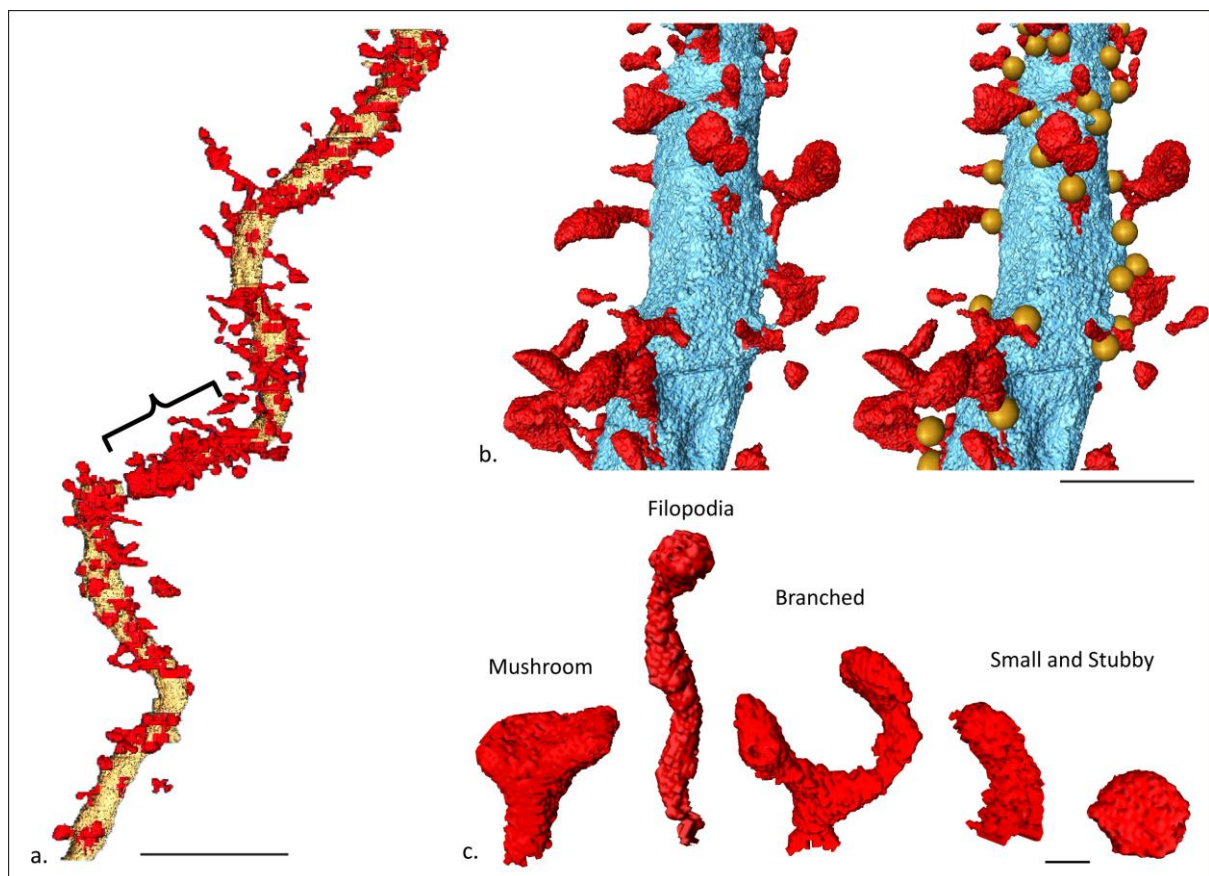


Figure 3.38: (a.): apical dendrite with isolated spines, in some region, the spines could not be cut off (bracket); (b.):(i) isolated spines are well recognized on upright dendrites, (ii) overlay of (i) and independently manually marked spine positions; (c.) exemplary single spines from (b.); scale bars = 10 μ m in (a.), 2.5 μ m in (b.), 0.5 μ m in (c.).

separated individual spines and the disconnected spine heads remain in the imagestacks in addition to some binary noise from the subtraction step of the backbone. In the following two steps, the binary noise is filtered and the remaining single components are cropped and saved separately as small binary .tif stacks according to their individual bounding box. As of now, this pipeline is still in its initial development phases and currently undergoing construction. It contains significant software “bugs” such as not being able to detect spines on dendrites that have an acute angle or branch (Figure 3.38(a.), bracket). In vertical upright dendrites the results are pretty reliable as demonstrated in Figure 3.38(b.), where the cut off spines (red) are overlaid with the manually selected landmarks, quantified in section 3.3.1.4. In (c.) some examples of single isolated spines from (b.) are shown. These resemble the common classification of spine morphologies. The eventual aim is to be able to isolate tens of thousands of single spines and build up a dendritic spine database from which spines can be clustered and biophysically characterized according to their morphological features. This is what is termed “Spinomics”.

Studying tens of thousands of single spines at this resolution (25x25x30nm), will have a huge impact on spine morphologies. The novelty of this study is apparent since previous studies of a similar nature have generally been performed using light microscopy and thus result in a very poor resolution (Brusco et al, 2010; Konur et al, 2003). Alternatively, if performed with EM only few spine morphologies have been extracted (Arellano et al, 2007; Harris & Stevens, 1989). This study can bring together the quantitative light and high resolution electron microscopy approach. Thereby, intermediates and spine morphologies that, due to either a poor resolution or a inappropriately small selection of high resolution morphologies, might be able to be observed.

Chapter 4 Discussion

Summary

The SBFSEM technique allows obtaining quantitative data from large volumes (mm^3) at nanoscopic resolution. So far this method has only been applied in a handful of laboratories and is mostly used to identify the connection properties of certain brain areas (connectomics). The work presented in this thesis, however, describes the design and establishment of a workflow to use the SBFSEM technique for visually determined single neurons. For this purpose, a novel staining protocol was developed which only stains the desired and previously identified neuron. To obtain useful information of the raw data recorded from SBFSEM, the custom segmentation toolbox NeuroStruct was expanded and validated against manual reconstructions, which are commonly seen as the “ultimate validation” and which are usually the only possibility to gain information from EM data. In conclusion, nanoscopic morphological information of an entire L5B neuron (and datasets of 9 additional neurons) could be obtained for further analysis.

4.1 Development of a Specific Staining Protocol for Biocytin-filled Neurons

4.1.1 Imaging issues

The SBFSEM technique was used to investigate large volumes at a nanoscopic lateral resolution. A pixel resolution of about 25 nm and a comparable longitudinal resolution of 30 nm were chosen to be able to obtain all spines and the majority of spine necks. To increase the resolution in z (cutting step) by 40% in comparison to the originally published 50 nm, the energy of the electron beam had to be decreased to below 3.0 keV. Table 4.1 briefly summarizes the effect of different scan parameters to the sample and the image recorded,

Parameter Effect on	Water Vapor	High Voltage	Spot Size
Resolution	↓	↑(↓)	↓
Contrast	↓	↑	↑
Charging	↓	↑	↑
Sample Integrity	/	↓	↓

Table 4.1: Effect of the major scanning parameters on resolution, contrast, sample charging and -integrity; increase. Increasing the influx of water vapor (decreasing the vacuum), resolution and contrast go down and charging is reduced; increasing HV results in a, up to a certain value (see text), higher resolution and better contrast, charging of the sample is enhanced and the structural integrity of the probe can be affected; increasing the spot size results in a worse resolution, better contrast, more intense charging and can lead to disruption of the probe.

respectively. Thus, by decreasing the high voltage (HV) the water influx and spot size must also be adjusted in order to obtain a sharp, non-charged image. Another motive, aside from charging, to decrease the HV from the values proposed by Denk and Horstmann (Denk & Horstmann, 2004) is that the electron beam interacts with a certain tissue volume, dependent on the electron beam energy (scaling $E^{1.67}$) (Joy & Joy, 1996; Kanaya & Okayama, 1972). If too high scan energy is applied in SBFSEM, tissue information deeper than the cutting step is gathered and therefore

the images are distorted ((Denk & Horstmann, 2004) values published: HV: 4 keV and 7 keV, spot 2.5 and 3.3).

4.1.2 Staining issues

Staining protocols for EM are based on the contrast introduced by heavy metal salts that react with certain chemical groups within the tissue. Usually the EM experimenter is interested in a specific protein or a protein complex such as postsynaptic densities (PSD) and high membrane integrity to enable the location of the desired structures such as synapses. Thus, common EM protocols generally tend to stain everything. In the case of this study, one or more identified single neurons were filled in a patch-chamber under a light microscope and the tracking molecule biocytin was loaded into the neuron. Staining of the membranes was not desired, as the tracer of interest was located in the cytosol. Furthermore, each additionally stained structure could interfere with the later automated segmentation. For this reason, a staining protocol was developed that almost exclusively contrasts the location of the introduced tracer and therefore the cytosol of this specific cell. In this way, the subcellular morphologies of the neuron could easily be extracted. The shortcoming of this type of staining is that no direct functional elements, such as pre-synaptic sites or PSDs, can be observed. However, as discussed later, by obtaining post-synaptic spines at an almost isotropic voxel resolution of 25x25x30nm, spine morphologies can be characterized in detail and PSD size and biophysical properties can be deduced.

After assessment of different combinations of uranyl acetate (UAc), osmium tetroxide (OsO₄) and lead (Pb) citrate, a staining protocol was found that depicts a very intensely labeled structure and faint unspecific staining of the overall neuropil.

UAc binds to many biological molecules such as nucleic acids, proteins and membranous structures (Hayat, 2000). Furthermore, uranium is the heaviest (and therefore most electron dense) heavy metal commonly used for contrasting biological tissue. These two properties make it the agent of choice for electron microscopy in thin slices as well as in *en bloc* stainings. Since the affinity of UAc appears to be higher for certain membranous structures (see epithelial or pericytes in Figure 3.7) compared to others, this specificity makes a regulation for a uniform and low overall contrast unattainable. Therefore, an attempt was made to contrast the tissue block with OsO₄ only. The outcome of the staining was double-edged: on the one hand the staining eliminated the interfering stained neuropil, but on the

other hand the neuronal structure had even lower contrast with fewer conductive components (metals) being present in the tissue (Figure 3.9). Since SEM and, for its low voltage use, especially SBFSEM, has inherently lower contrast than TEM, an autofocus routine in the take-up of the images was inoperable and, logically, the contrast was even lower. This 'low intensity' staining was another undesirable aspect that, at least to this extent, does not occur in conventionally stained tissue. Due to the insulating capability of the embedding resin there are only two possibilities to avoid charging of the sample: (i) water vapor is vented into the sample chamber and reabsorbs the charge before being deposited onto the surface of the block to avoid an overly intense charging of the sample or (ii) conductive metals in the tissue absorb the charging electrons and lead them away from the resin. Due to the fact that the neuropil would not be contrasted entirely, the amount of overall distributed metals in the tissue was reduced. The effect of the high voltage (HV) electron beam was therefore even stronger and resulted in a black shadow on the image. Since larger areas are scanned in overlapping mosaic tiles, the borders of the images are scanned twice or up to four times. Thus, the charging effect in these regions is considerably increased (stars in Figure 3.9). The compensatory effect of conductive components is particularly evident in the right charged border of Figure 3.8(a.), where a non-charged bright halo is surrounding the OsO₄ stained neuronal structure. To improve the staining protocol, the OsO₄ staining was optimized and the specific contrast was supported with an *en bloc* Pb-acetate stain. The result was a staining that showed a very intense structure and a very faint nonspecific staining of the overall neuropil (Figure 3.10(a.) and (b.)). After succeeding with a proper staining protocol, the protocol was reproduced and quantified. The staining analysis in section 3.1.3 resulted in an average grey value difference of neuron to neuropil of 53 grey values. As this calculation did not reflect the variability in the contrast values of either the neuronal structure or the surrounding tissue, the standard deviations for both signals were taken into account with a two-tailed t-distribution. This t-distribution gives an indication of how well the values can be allocated into signal and background. The average $t = 3.77$ was highly significant ($p = < 0.0002$, (Soper, 2012)) but as the threshold values were taken as the basis for this distribution, this is not unexpected. For comparison, an image stack of a sample that was not segmentable was analyzed in the same manner (Figure 3.24). For this sample, the values could not be separated by a threshold and so the measured values contained both putative signal and background values alike. The t-value of this stack was

only half the average t-value ($t = 1.93$) of the evaluated staining protocol which indicates that, despite the fact that separated values were taken, this analysis gives an objective and computable indication of whether a staining is suitable.

The disadvantage to this kind of staining is that no direct functional elements like pre-synaptic sides or PSDs can be observed. However, as discussed later, by obtaining post-synaptic spines at an almost isotropic voxel resolution of $25 \times 25 \times 30 \text{ nm}$, spine morphologies can be characterized in close detail and PSD size and biophysical properties can be deduced. This staining protocol was the basis for improving our segmentation toolbox NeuroStruct and obtaining quantitative morphological data of specific neurons.

4.2 Expansion and Validation of NeuroStruct

4.2.1 The RV-Connectivity-Filter

Segmentation of spines with thin necks suffers from different problems. Very thin necks may possess an internal diameter, which is not always resolved by our voxel resolution of $25 \times 25 \times 30 \text{ nm}$. Moreover, staining artifacts, sometimes with neuronal-like shapes, increase the object noise and complicate the recognition and reconstruction of dendrites and their spines. To tackle this problem in the automated segmentation, a radius and volume dependent connectivity filter was implemented into NeuroStruct.

As mentioned, owing to the small diameter of dendritic spine's necks, some connections could not be resolved. However, since only single neurons are stained in the sample, a disconnected but clearly stained spine head in close proximity of the neuron must belong to the designated neuron in the closest proximity. To prevent generation of segment artifacts, the maximal radius and the minimum volume of the respective structure are parameters which are manually set in the filter. A radius of 60 pixels and a minimum volume of 600 pixels, have been found to be sufficient parameters to retrieve disconnected spine heads with minimal generation of artifacts. In rare cases, large artifacts can occur in close

proximity of the dendritic backbone. These artifacts are segmented as well, as the filter does not discriminate the shape of the structure. Nevertheless, incorporating the RV-Connectivity-Filter into NeuroStruct provides a significant benefit to the complete spine tracking of the dendrite in comparison to a segmentation of the structure without it. For the validation in the object space, Table 3.5 and Table 3.6 summarize the number of false objects being detected by NeuroStruct and the MTs with respect to the Reference Tracings (R1 and R2, respectively). The result of only 5 false objects for NeuroStruct in comparison to 34 +/- 19 for the MT reflects, that the toolbox, including the RV-Connectivity-Filter, gives excellent results.

4.2.2 Original SBFSEM Dataset

The reference dataset was recorded with a voxel resolution of 25x25x30nm. Besides the aforementioned thin necks that may possess an internal diameter that is unresolvable, spines located in close proximity to each other (at a distance approaching our SBFSEM resolution) appear spatially degenerate and, depending on whether their corresponding necks are segmented, may form loops and appear incomplete or disconnected from the dendritic stem in the 3D space. One way to overcome this obstacle would be to increase of the scanning resolution. Regarding the actual hardware setup of the SBFSEM used in this study, this would be a pyrrhic victory as it would be at the expense of longer acquisition time, higher charging, higher electron dose, and larger digital storage space. Since most of the spines are obtained as complete structures and the voxels are almost isotropic, the chosen resolution is entirely satisfactory.

4.2.3 Manual Tracings

A visual inspection of the 3D reconstruction in the object space shows two basic patterns regarding the followed segmentation strategies of the individual tracers: (i) the individual that generated M3 appears to have segmented every high contrast region as foreground

objects, without judging between stained artifacts or true objects, (ii) tracers M1, M2, M4 and M5 orientated the segmentation should be oriented towards true objects. From these tracings, M1 and M4 traced true objects even if they were disconnected from the dendritic stem. M2 and M5 attached every structure to the main dendrite, even if the traces of the connections on the images were vaguely defined. All manual reconstructions are displayed as an overlay in Figure 3.27. The insets zoom in at two specific domains of the image stack and display the overlays of the MTs paired with the RTs in Figure 3.27(b. and c.) and (d. and e.), respectively. The RT insets show overlays of R1 (dark) and R2 (transparent red). We observe a complex surface and morphological topology of the underlying neuronal structure. The filled arrowhead indicates the location of the spine head that is present in R2 but not in R1 as it is shown in Figure 3.27(b.). The voxel surplus of R2 envelopes the entire surface of the neuron, which is why the structure shows a red covering, implying a variability of the MTs distributed along the dendritic stem and spines as also shown in the corresponding insets of the MTs.

4.2.4 True Objects: How “true” are the Computational and the Manual Reconstructions?

We observed that the number of recognized 3D objects is highly user-dependent. Thus, how can one be sure that all true objects (e.g. spines) have been traced? Quantification of the variability of the computational approach depends on the comparison to manual reconstructions that suffer from subjective errors. However, we found that the NeuroStruct reconstruction represented the reference tracings with a high level of accuracy. In the computational reconstruction, the sensitivity is determined by the parameters used for the segmentation and connectivity analysis.

To check for the completeness of true objects in our validated computational tracing ($\eta_s=24$), we compared our results to reconstructions created by a more stringent (NSt^+ ; $\eta_s = 26$) and a more promiscuous (NSt^- ; $\eta_s = 22$) parameter, respectively. The absolute voxel volume differences with respect to NSt are: $|\delta V(NSt^-)| = 2.2 \%V(R1)$ and $|\delta V(NSt^+)| = 1.1 \%V(R1)$. Figure 3.28(b.) and (c.) show the overlays of two different regions of the

reconstructions of NSt^- (transparent red) and NSt (dark). Remarkably, NSt^- contains one additional spine head, which completes one existing true object: only a segment of the spine neck attached to the dendritic stem was identified beforehand (Figure 3.28(b.); filled arrowhead). Moreover, existing parts of few spines are completed (Figure 3.28(c.); filled arrowheads). On the other hand, more false objects were traced: five NSt positive and four NSt negative (Figure 3.28(c.); hollow arrowheads). The lower threshold parameter also leads to the formation of very small loops owing to higher surface pixel noise; a total of 22 loops which is six more than in NSt (Figure 3.28(b.); hollow arrowheads). Figure 3.28(d.) displays the overlays of the reconstruction of NSt^+ (red) and NSt (transparent dark). Regarding the NSt^+ reconstruction, no false objects existing in the NSt reconstruction (filled arrowheads) were traced and three fewer loops (13 loops) were created in comparison to NSt . On the other hand, many spines appear incomplete (hollow arrowheads). The findings are summarized in Table 3.3. The NSt^- segmentation has led to a complete picture of all true objects at the expense of more artifacts and higher disorder (in terms of binary noise) on the neuronal surface terrain, an effect, which could be significantly reduced by slightly smoothing the surface. On the other hand, the NSt^+ segmentation has led to a smoother 3D surface terrain for the underlying neuronal structure, but an incomplete picture of the traced spines. Even in this case, the error introduced by the number of incomplete spines was small, $\sim 6.5\%$. The extra spine head detail that was traced by the NSt^- was also found in M4 and M5. A relaxation in the rule for the selection of the foreground pixels of the reference tracing to two out of five would declare this spine as a true object. This “reference”, however, would most likely result in more false objects, which is also true for NSt^- .

4.2.5 Conclusions

We evaluate a computational workflow, NeuroStruct, as a solution for the complete tracing of dendritic spines from images derived from a single biocytin-filled cell using SBFSEM imaging. The evaluation is based on two reference tracings generated from five independent manual segmentations in which the degree of ambiguity and errors introduced by human

investigators has been quantified. NeuroStruct has delivered a result that is as complete and precise as human tracings and moreover, it does not suffer from the ill-defined conditions that are present in the human tracings: humans are subjective, biased, can change criteria and criteria also differ between individual tracers. In addition, if the final tracing is the result of several hand drawn contours, artifacts such as loops and inadequate reconstructions of neuronal structures derived from spatial dislocations can be introduced. In comparison to other computational methods, NeuroStruct does not use any user-based selection of regions of interest, thereby making the results reproducible and applicable to multiple datasets of comparable image stack quality, as shown in this thesis. Therefore, processing single biocytin-filled SBFSEM data with our toolbox is a reliable way for fast and robust incremental reconstruction of terabyte datasets and retrieval of large-scale spine populations.

4.2.6 Comparison to other Segmentation Approaches

As previously mentioned in section 1.4, other segmentation approaches have been developed for large scale segmentation of data obtained from SBFSEM. These tools are mostly developed to obtain circuit information of complex wirings. Therefore the tracings are built to either volume reconstruct fine axonal structures (Jurrus et al, 2009; Macke et al, 2008) or skeletonize the entire neuropil (Helmstaedter et al, 2011). Jakob Macke's (Macke et al, 2008) and Elisabeth Jurrus' (Jurrus et al, 2009) segmentation approaches were designed to trace axonal volumes from SBFSEM image stacks using a combination of an edge-detection and contour propagation. These topologically simple and tube-like structures are not comparable with the heterogeneity of dendritic spine morphologies and thus these methods are most likely not applicable to reconstruct these by far more complex structures. Another recently published segmentation toolbox is Moritz Helmstaedter's KNOSSOS (Helmstaedter et al, 2011), is a manual but computer-assisted tracing tool which allows the user to trace skeleton representations of neuron morphologies. From a seeding point, a user is clicking the center point of a neuronal structure every 7-10th image and mark branching points. According to the authors, this approach decreases the tracing time of neurite path length by ~50fold compared to pure manual tracing of volume labeling with, for example

Reconstruct (Fiala, 2005). To obtain a reliable reconstruction (reducing the manual error rate to 1) ~20 redundant reconstructions are necessary, which is why an armada of over 100 undergraduate students are reconstructing tissue blocks simultaneously (Moritz Helmstaedter, personal communication). Due to its nature of tracing only the center point of a neuronal structure, this technique is also not suitable to detect spines or even reconstruct their morphologies.

Kurt Saetzler's region growing algorithm "BayTrac" (Saetzler et al, 2009) is able to trace connected volumes, which makes it the only really approach to compare with NeuroStruct. The reasons for NeuroStruct and not BayTrac became our tracing toolbox of choice are numerous: firstly, every region is manually drawn in a cross section of an image stack and no defined parameters can be set to reproduce the tracing result. Secondly, the segmentation works strictly sequentially, which makes it rather slow in comparison to the highly parallelized (using up to 1000 CUDA cores on the graphics adapter) NeuroStruct. Thirdly, due to the principle of region growing, disconnected spine heads cannot be segmented, and fourthly, the reconstructions were constantly over- or under- segmented. Since the method is not based on parameters settings but on manual selection of pixels, an appropriate method of segmentation optimization is not possible.

With NeuroStruct it is possible to receive volume information of single biocytin-filled neurons in a fully automated manner. As it has high parallelization on CUDA, NeuroStruct is very fast. Since typically only one parameter (η) has to be adjusted at any one time, the toolbox is easy-to-use and reproducible in its result. The expansion with the RV-Filter allows NeuroStruct to retrieve even disconnected spine heads and exclude potential artifacts. The very detailed validation of NeuroStruct proves the correct reconstruction of topologically challenging morphologies like dendritic spines. None of the above mentioned segmentation approaches is able to fulfill these demands.

4.3 Large Scale Reconstruction and Spinomics

4.3.1 Acquisition of SBFSEM Data

As shown in section 3.1 and 3.3, large image stacks were acquired with SBFSEM. Acquisition of the neuron TK100909A1 shown in section 3.3 was rather problematic due to several unforeseeable problems occurring during the scanning procedure. This can be illustrated by a comparison of calculated versus actual scan times. The calculated scan time for the scanned 300212 single tile images (6000x), 21225 overviews (1000x) and cuts was roughly 240 days. In total, however, the acquisition from st001 to st041 took 282 days. This discrepancy is explained by the numerous interventions that had to be overcome.

The SBFSEM system used in this thesis is the first system built by Winfried Denk and was previously utilized in the original publication in 2004 (Denk & Horstmann, 2004). This system is custom-built and is therefore still experiencing some initial problems. These issues are mostly software malfunctions of one of the three computers steering the acquisition of the data: (i) control of the microtome (cutting and moving the sample, via a spike script), (ii) taking images and operating the EM (EM software, FEI) and (iii) one master computer coordinating the two other computers via an ImageJ script. Most of the software malfunctions were interface error or sampling restart problems of the master computer or data overflow of the spike script running on the microtome computer. In addition to these custom software crashes, the EM software also malfunctioned. Furthermore, as the hardware of the FEI Quanta FEG 200 was not built for 24/7 scanning, several hardware components of the microscope as well as custom integrated hardware components had to be repaired, serviced, or replaced. The custom detector and two motors of the microtome and the electron emitter and one vacuum pump had to be replaced, the EM itself was serviced two times during the acquisition of the GLT-neuron. Finally, at times electric interferences (white noise) interfered with the scans and in some cases had such a strong overlay on the images, that the images were rendered unusable (eg. st032-36). Nevertheless, scans of an entire L5B neuron could be obtained with only 1.2% loss; with the

exception of the basal dendrites, which were not scanned due to the undersized scanning area.

The actual state-of-the-art SBFSEM, that was used by Kevin Briggman to obtain data of the retina in mouse, was improved in many ways to decrease the acquisition time (Briggman et al, 2011). While the data for this thesis was acquired with a pixel dwell time of $8\mu\text{s}$, the data from Briggman et al. was acquired with only $1.9\mu\text{s}$. This decrease in the acquisition time by a factor of 4 could be achieved by a more sensitive detector system and an improved staining protocol which incorporated sufficient metal into the tissue, to enable the probe to become intrinsically conductive. A conductive sample enables scanning in high vacuum mode without charging of the sample. As a consequence, the contrast is higher and the image is sharper due to the lack of water vapor in the scanning chamber. Since the protocol stains all kinds of structures, it is not applicable for the purpose discussed in this thesis. If, however, the pixel dwell time could be shortened to $2\mu\text{s}$ (e.g. by using a more sensitive detector system), this would result in only a 4 second acquisition time for a single 1768×2048 pixel image. Therefore, the calculated scan time for the scanned dataset TK100909A1 would be shortened from 240 days to only 141 days; since moving in x/y and the cutting steps are not accelerated, the total acquisition would theoretically be shortened by ~40%.

4.3.2 The Reconstruction of GLT-L5B Neuron: TK100909A1

For the entirely scanned and reconstructed GLT positive L5B Neuron TK100909A1, 184 individual segmentations were conducted. But how reliable is the morphological data obtained by the SBFSEM? Data gathered from conventional sSEM or ssTEM has to be corrected for shrinkage and distortion introduced by preparation and/or cutting of the slices (Hoffpauir et al, 2007; Peachey, 1958). The data in this study was not corrected for any physical deformations but as shown in Figure 3.36, the total reconstruction can be accurately superimposed with the light microscopy image of the DAB stained neuron. If shrinkage or distortion of the sample occurred, a small error would magnify itself throughout the 184 reconstructions, and the final reconstruction would result in severe misalignment. This suggests that the reconstructions are very accurate and that no severe

shrinkage occurred during the preparation for EM and the gathering of data in the SBFSEM. Regarding the validation of NeuroStruct, one can also deduce that all 184 reconstructions are as complete as a comparable manual reconstruction.

4.3.3 Spine Density Analysis of TK100909A1

Unfortunately, the acquired data could not be evaluated and analyzed in extensive detail due to the filters required to initiate detailed spine analysis is still in the test phase. The manual labeling of dendritic spines at their origin neck position at the dendritic backbone, is the first score of spine densities of one defined cell at this high resolution. Two famous spine counting studies of this kind were conducted by Martin Feldman and Alan Peters in 1979 (Feldman & Peters, 1979) and Alan Larkman in 1991 (Larkman, 1991). Both analyses were performed on pyramidal neurons in the visual cortex of the rat and both used bright field microscopy to count dendritic spines. Feldman and Peters used a Golgi-stain and counted the dendritic spines on a 50 μm length of an apical dendrite in L3. In light microscopy they could observe a spine density of approximately 2.2spines/ μm dendritic length. By the application of a correction factor for the obscured spines, they succeeded in a spine density of 6.8spines/ μm . The result was validated using a 6.5 μm ssTEM stretch (86 sections each 75nm thick) of that section, by which they resulted with a spine density of 7.2 spines/ μm . The paper was more of a proof of principle, demonstrating that counting spines with the light microscope was reliable when correcting for the spines that had been obscured due to the longitudinal resolution.

This principle was used by Larkman twelve years later in his famous spine distribution paper from 1991 (Larkman, 1991). He used neurons that were injected with horseradish peroxidase (HRP) and stained them with DAB. Like Feldman and Peters, he also used a correction factor for obscured spines. The factor depended on the diameter of the dendrite and was calculated to be in the range of 1.2 to 2.2 for dendrite diameters of 1.1 μm to 4 μm , respectively. Thereby, maximum spine densities of 5-8 spines/ μm were found. Further Larkman assumed that for a given cell and dendrite type (basal, apical trunk, etc.) segments of similar diameters have similar spine densities. For this, he extrapolated the average total

amount of spines for different cell types and for different dendritic stretches and ended up with 14932 (+/- 3371) spines for thick tufted L5B cells (averaged for 113 segments from 11 cells). Moreover, he quantified the amount and percentage of spines per layer (means). The results taken together are summarized with the findings in this thesis in Table 4.2.

	L1:		L2:		L3:		L4		L5 (pooled):	
Larkman	1482	9.2%	880	5.7%	1089	7.0%	1384	8.9%	10654	68.8%
TK100909A1	1781	27%	646	10%	1060	16%	509	8%	2676	40%

Table 4.2: Spine distributions in layers, results are a comparison between Larkman 1991 and this thesis. L5A&B were pooled for comparison.

Remarkably, the spine numbers counted in this thesis are almost identical to the results averaged by Larkman for the first three layers, thus validating both separate methodologies. The discrepancy in L5 can easily be explained by the fact that in the beginning of the scan of TK100909A1 the scanning grid was set too small and thus many basal dendrites were not recorded. The variation in L4, however, cannot be explained by missing dendritic structures. It is conceivable that, as this particular GLT neuron is located in an outer barrel (compare Figure 3.30(c.)), fewer spines may have developed in L4 due to less synaptic input. If so, why would the number of spines in the upper layers be so compatible? Another hypothesis for the number of spines being only 37% compared to Larkman's average in L4 is that only 12.3% of all present L5B neurons are GLT (Groh et al, 2010). Therefore, it might be that GLT neurons by themselves bear fewer spines in L4 than other thick tufted L5 neurons and build another distinct L5B sub-class. The most probable explanation, however, might be that Larkman investigated thick tufted L5B cells in the visual cortex (VC) of the rat, while the SBFSEM scanned neuron was located in the somatosensory barrel cortex (BC) of the mouse. As mentioned above, Larkman reported maximum spine densities of up to 8 spines/ μm . The validation dataset discussed in section 3.2 revealed 106 spines on roughly 25 μm dendritic length (-4spines/ μm) and was one of the densest stretches along the apical dendrite. In 2010, Briner et al. quantified spine densities in L5B neurons in the BC using confocal microscopy for whisker-input deprived and non-deprived animals at different ages (Briner et al, 2010). They quantified the spine densities with 0.7 spines/ μm (L1), 0.86 spines/ μm (L2/3), and 1.3 spines/ μm (L4) for 30 days old animals with whiskers. As they did not use a

correction factor for obscured spines, the actual densities might be up to 2.2 times higher than those reported (see above). This supports the assumption that the varying spine calculations in L4 are derived from different cortices in different species.

Since the data presented on spine density in this thesis is based on only one single neuron, the numbers need to be validated through repetition. The only way of verifying the quantification is to scan additional GLT neurons in SBFSEM. Due to time constraints, this was not achievable during this thesis.

4.3.4 Spinomics and Outlook

A further planned project on the data derived from single biocytin-filled neurons is to investigate single spine morphologies. Because the entire cytosol is contrasted, it is not possible to detect inner cellular compartments, whereas the structural morphologies of single spines are quantitatively recovered at almost isotropic resolution. The initial characterization would be to cluster spines by their anatomy. As this would not be completed for one hundred spines, as is usually the case for EM (see section 1.3.2), but for thousands, this would generate a very detailed analysis. This kind of quantitative analysis on morphologies is currently performed with light microscopic approaches (see section 1.2.2). Figure 3.38(c.) displays examples of the morphologies obtained.

In section 1.1.2 the relation of morphology to function was described: The volume of the head is directly proportional to the size of the PSD, to the number of postsynaptic receptors and the size of the presynaptic terminal, to the number of docked synaptic vesicles and to the readily releasable pool of neurotransmitters. The size of the spine head directly correlates with the number of AMPA receptors in the PSD. The spine neck acts as a barrier to compartmentalize and chemically isolate the spine itself. Obtaining thousands of spine morphologies at nanoscale resolution will display the variety in morphologies that exist. Deducing biochemical properties will provide computational models to biophysically classify dendritic spines.

Since all spines derive from single and identified neurons, analysis of specific cell types can be conducted and combined with electrophysiological experiments. At this isotropic resolution we are able to resolve even thin spine necks, allowing us to characterize every single spine of a specific neuron in great detail. This provides highly detailed information such as the specific spine distribution, density changes, characteristic diameters and membrane gain on certain areas of the neuron. Generating new tools to improve the evaluation of this data will provide a better understanding of the cell's input sites and biophysical properties and thus, will provide profound and accurate data to improve simulations.

Chapter 5 References

Abbe E (1873) Beiträge zur Theorie des Mikroskops und der mikroskopischen Wahrnehmung. *Arch Mikrosk Anat* **9**: 413-418

Adams I, Jones DG (1982) Quantitative Ultrastructural-Changes in Rat Cortical Synapses during Early-Adulthood and Late-Adulthood. *Brain Research* **239**: 349-363

Agmon A, Connors BW (1991) Thalamocortical responses of mouse somatosensory (barrel) cortex in vitro. *Neuroscience* **41**: 365-379

Alvarez VA, Sabatini BL (2007) Anatomical and physiological plasticity of dendritic spines. *Annual review of neuroscience* **30**: 79-97

Arellano JI, Benavides-Piccione R, Defelipe J, Yuste R (2007) Ultrastructure of dendritic spines: correlation between synaptic and spine morphologies. *Front Neurosci* **1**: 131-143

Azevedo FA, Carvalho LR, Grinberg LT, Farfel JM, Ferretti RE, Leite RE, Jacob Filho W, Lent R, Herculano-Houzel S (2009) Equal numbers of neuronal and nonneuronal cells make the human brain an isometrically scaled-up primate brain. *J Comp Neurol* **513**: 532-541

Banker G, Churchill L, Cotman CW (1974) Proteins of the postsynaptic density. *J Cell Biol* **63**: 456-465

Berkley HJ (1895) Studies on the lesions produced by the action of certain poisons on the nerve-cell. *Med News* **67**: 225-231

Bertalmio M, Sapiro G, Randall G (1998) Morphing active contours: A geometric approach to topology-independent image segmentation and tracking. *1998 International Conference on Image Processing - Proceedings, Vol 3*: 318-322

Briggman KL, Denk W (2006) Towards neural circuit reconstruction with volume electron microscopy techniques. *Curr Opin Neurobiol* **16**: 562-570

Briggman KL, Helmstaedter M, Denk W (2011) Wiring specificity in the direction-selectivity circuit of the retina. *Nature* **471**: 183-188

Briner A, De Roo M, Dayer A, Muller D, Kiss JZ, Vutskits L (2010) Bilateral whisker trimming during early postnatal life impairs dendritic spine development in the mouse somatosensory barrel cortex. *J Comp Neurol* **518**: 1711-1723

Brusco J, Dall'Oglio A, Rocha LB, Rossi MA, Moreira JE, Rasia-Filho AA (2010) Descriptive findings on the morphology of dendritic spines in the rat medial amygdala. *Neurosci Lett* **483**: 152-156

- Cajal SR (1888) Estructura de los centros nerviosos de las aves. *Rev Trim Histol Norm Pat* **1**: 1-10
- Cajal SR (1894) La fine structure des centres nerveaux. *Proc Roy Soc Lond* **55**: 443-468
- Cajal SR (1896a) El azul de metileno en los centros nerviosos. *Rev Trimest Micrográf Madrid* **1**: 151-203
- Cajal SR (1896b) Las espinas colaterales de las células del cerebro tenidas por el azul de metileno. *Rev Trimest Micrográf Madrid* **1**: 123-136
- Carlsson I, Terzopoulos D, Harris KM (1994) Computer-assisted registration, segmentation, and 3D reconstruction from images of neuronal tissue sections. *IEEE Trans Med Imaging* **13**: 351-362
- Celikel T, Sakmann B (2007) Sensory integration across space and in time for decision making in the somatosensory system of rodents. *Proc Natl Acad Sci U S A* **104**: 1395-1400
- Chang HT (1952) Cortical neurons with particular reference to the apical dendrites. *Cold Spring Harbor symposia on quantitative biology* **17**: 189-202
- Chicurel ME, Harris KM (1992) Three-dimensional analysis of the structure and composition of CA3 branched dendritic spines and their synaptic relationships with mossy fiber boutons in the rat hippocampus. *J Comp Neurol* **325**: 169-182
- Cohen RS, Blomberg F, Berzins K, Siekevitz P (1977) The structure of postsynaptic densities isolated from dog cerebral cortex. I. Overall morphology and protein composition. *J Cell Biol* **74**: 181-203
- Conn M, Colowick SP, Kaplan NO, Abelson JN, Simon MI (1999) *Methods in enzymology: Confocal microscopy*, San Diego, USA: Academic Press.
- Cooney JR, Hurlburt JL, Selig DK, Harris KM, Fiala JC (2002) Endosomal compartments serve multiple hippocampal dendritic spines from a widespread rather than a local store of recycling membrane. *Journal of Neuroscience* **22**: 2215-2224
- Crang RFE, Klomparens KL (1988) *Artifacts in Biological Electron Microscopy*, first edition edn. New York, USA: Plenum Press.
- Crick F (1982) Do Dendritic Spines Twitch. *Trends Neurosci* **5**: 44-46
- de Kock CP, Bruno RM, Spors H, Sakmann B (2007) Layer- and cell-type-specific suprathreshold stimulus representation in rat primary somatosensory cortex. *The Journal of physiology* **581**: 139-154

- De Simoni A, Edwards FA (2006) Pathway specificity of dendritic spine morphology in identified synapses onto rat hippocampal CA1 neurons in organotypic slices. *Hippocampus* **16**: 1111-1124
- Deller T, Korte M, Chabanis S, Drakew A, Schwegler H, Stefani GG, Zuniga A, Schwarz K, Bonhoeffer T, Zeller R, Frotscher M, Mundel P (2003) Synaptopodin-deficient mice lack a spine apparatus and show deficits in synaptic plasticity. *Proc Natl Acad Sci U S A* **100**: 10494-10499
- Denk W, Horstmann H (2004) Serial block-face scanning electron microscopy to reconstruct three-dimensional tissue nanostructure. *Plos Biol* **2**: e329
- Denk W, Strickler JH, Webb WW (1990) Two-photon laser scanning fluorescence microscopy. *Science* **248**: 73-76
- Diaspro A, Bianchini P, Vicidomini G, Faretta M, Ramoino P, Usai C (2006) Multi-photon excitation microscopy. *Biomedical engineering online* **5**: 36
- Ding JB, Takasaki KT, Sabatini BL (2009) Supraresolution Imaging in Brain Slices using Stimulated-Emission Depletion Two-Photon Laser Scanning Microscopy. *Neuron* **63**: 429-437
- Dogiel AS (1896) Die Nervelemente in Kleinhirne der Vögel und Säugethiere. *Arch mikrosk Anat* **47**: 707-718
- Donald AM (2003) The use of environmental scanning electron microscopy for imaging wet and insulating materials. *Nature materials* **2**: 511-516
- Drouvelis P, Kurz TA, Lang S (2012) NeuroStruct: A Toolkit for the Precise and Reliable Large-Scale Reconstruction of Dendritic Spines from Biocytin-filled Neurons from SBFSEM (submitted). *Med Image Anal*
- Druckmann S, Berger TK, Schurmann F, Hill S, Markram H, Segev I (2011) Effective stimuli for constructing reliable neuron models. *PLoS computational biology* **7**: e1002133
- Edinger L (1893) Vergleichend-entwicklungsgeschichtliche und anatomische Studien im Bereiche der Hirnanatomie. *Anat Anz* **8**: 511-525
- Ehlers MD (2003) Activity level controls postsynaptic composition and signaling via the ubiquitin-proteasome system. *Nat Neurosci* **6**: 231-242
- Ethell IM, Pasquale EB (2005) Molecular mechanisms of dendritic spine development and remodeling. *Progress in neurobiology* **75**: 161-205
- Everhart TE, Hayes TL (1972) The scanning electron microscope. *Scientific American* **226**: 55-69

Everhart TE, Thornley RFM (1960) Wide-band detector for micro-microampere low-energy electron currents. *Journal of Scientific Instruments* **37**: 246

Feldman ML, Peters A (1979) A technique for estimating total spine numbers on Golgi-impregnated dendrites. *J Comp Neurol* **188**: 527-542

Fiala JC (2005) Reconstruct: a free editor for serial section microscopy. *J Microsc* **218**: 52-61

Fiala JC, Harris KM (2001) Cylindrical diameters method for calibrating section thickness in serial electron microscopy. *J Microsc* **202**: 468-472

Fiala JC, Spacek J, Harris KM (2002) Dendritic spine pathology: cause or consequence of neurological disorders? *Brain research Brain research reviews* **39**: 29-54

Fifkova E, Delay RJ (1982) Cytoplasmic Actin in Neuronal Processes as a Possible Mediator of Synaptic Plasticity. *J Cell Biol* **95**: 345-350

Fine A, Amos WB, Durbin RM, Mcnaughton PA (1988) Confocal Microscopy - Applications in Neurobiology. *Trends Neurosci* **11**: 346-351

Fox K (2008) *Barrel Cortex*, Vol. 1, Cambridge, UK: Cambridge University Press.

Freire M (1978) Effects of dark rearing on dendritic spines in layer IV of the mouse visual cortex. A quantitative electron microscopical study. *J Anat* **126**: 193-201

Gay H, Anderson TF (1954) Serial sections for electron microscopy. *Science* **120**: 1071-1073

Gerlach Jv (1872) *Von dem Rückenmark*, Leipzig: Wilhelm Engelmann Verlag.

Goldstein J, Newbury DE, Joy DC, Lyman CE, Echlin P, Lifshin E, Sawyer L, Michael JR (2003) *Scanning Electron Microscopy and X-ray Microanalysis*, 3rd edn.: Springer Science and Media.

Golgi C (1873) Sulla sostanza grigia del cervello. *GAZZETTA MEDICA ITALIANA Opera Omnia*: 90-98

Golgi C (1906) *Camillo Golgi - Nobel Lecture: The Neuron Doctrine – Theory and Facts*, Physiology or Medicine 1901-1921 edn. Amsterdam, The Netherlands: Elsevier Publishing Company.

Gray EG (1959a) Axo-somatic and axo-dendritic synapses of the cerebral cortex: an electron microscope study. *J Anat* **93**: 420-433

Gray EG (1959b) Electron Microscopy of Dendrites and Axons of the Cerebral Cortex. *J Physiol-London* **145**: P25-P26

- Groh A, Meyer HS, Schmidt EF, Heintz N, Sakmann B, Krieger P (2010) Cell-type specific properties of pyramidal neurons in neocortex underlying a layout that is modifiable depending on the cortical area. *Cereb Cortex* **20**: 826-836
- Grutzendler J, Kasthuri N, Gan WB (2002) Long-term dendritic spine stability in the adult cortex. *Nature* **420**: 812-816
- Harris KM, Jensen FE, Tsao B (1992) Three-dimensional structure of dendritic spines and synapses in rat hippocampus (CA1) at postnatal day 15 and adult ages: implications for the maturation of synaptic physiology and long-term potentiation. *J Neurosci* **12**: 2685-2705
- Harris KM, Perry E, Bourne J, Feinberg M, Ostroff L, Hurlburt J (2006) Uniform serial sectioning for transmission electron microscopy. *J Neurosci* **26**: 12101-12103
- Harris KM, Stevens JK (1988) *Intrinsic determinants of neuronal form and function*, Vol. Study of dendritic spines by serial electron microscopy and three-dimensional reconstruction, New York: A.R.Liss.
- Harris KM, Stevens JK (1989) Dendritic spines of CA 1 pyramidal cells in the rat hippocampus: serial electron microscopy with reference to their biophysical characteristics. *J Neurosci* **9**: 2982-2997
- Hayashi Y, Majewska AK (2005) Dendritic spine geometry: functional implication and regulation. *Neuron* **46**: 529-532
- Hayat MA (2000) *Principles and techniques of electron microscopy*, fourth edition edn. Cambridge, UK: Cambridge University Press.
- Hell SW, Wichmann J (1994) Breaking the diffraction resolution limit by stimulated emission: stimulated-emission-depletion fluorescence microscopy. *Opt Lett* **19**: 780-782
- Helmchen F, Denk W (2005) Deep tissue two-photon microscopy. *Nature methods* **2**: 932-940
- Helmstaedter M, Briggman KL, Denk W (2011) High-accuracy neurite reconstruction for high-throughput neuroanatomy. *Nat Neurosci* **14**: 1081-1088
- Helmstaedter M, de Kock CP, Feldmeyer D, Bruno RM, Sakmann B (2007) Reconstruction of an average cortical column in silico. *Brain Res Rev* **55**: 193-203
- Helmstaedter M, Sakmann B, Feldmeyer D (2009) The relation between dendritic geometry, electrical excitability, and axonal projections of L2/3 Interneurons in rat barrel cortex. *Cereb Cortex* **19**: 938-950
- Herculano-Houzel S (2009) The human brain in numbers: a linearly scaled-up primate brain. *Front Hum Neurosci* **3**: 31

- Hoffpauir BK, Pope BA, Spirou GA (2007) Serial sectioning and electron microscopy of large tissue volumes for 3D analysis and reconstruction: a case study of the calyx of Held. *Nat Protoc* **2**: 9-22
- Holmes WR (1990) Is the function of dendritic spines to concentrate calcium? *Brain Res* **519**: 338-342
- Holtmaat AJ, Trachtenberg JT, Wilbrecht L, Shepherd GM, Zhang X, Knott GW, Svoboda K (2005) Transient and persistent dendritic spines in the neocortex in vivo. *Neuron* **45**: 279-291
- Horikawa K, Armstrong WE (1988) A versatile means of intracellular labeling: injection of biocytin and its detection with avidin conjugates. *J Neurosci Methods* **25**: 1-11
- Hugel S, Abegg M, de Paola V, Caroni P, Gahwiler BH, McKinney RA (2009) Dendritic spine morphology determines membrane-associated protein exchange between dendritic shafts and spine heads. *Cereb Cortex* **19**: 697-702
- Jain V, Murray JF, Roth F, Turaga S, Zhitulin V, Briggman KL, Helmstaedter MN, Denk W, Seung HS (2007) Supervised learning of image restoration with convolutional networks. *IEEE Conf Comp Vis* **1-6**: 636-643
- Jones EG, Powell TP (1969) Morphological variations in the dendritic spines of the neocortex. *J Cell Sci* **5**: 509-529
- Joshi S, Hawken MJ (2006) Loose-patch-juxtacellular recording in vivo--a method for functional characterization and labeling of neurons in macaque V1. *J Neurosci Methods* **156**: 37-49
- Joy DC, Joy CS (1996) Low voltage scanning electron microscopy. *Micron* **27**: 247-263
- Jurrus E, Hardy M, Tasdizen T, Fletcher PT, Koshevoy P, Chien CB, Denk W, Whitaker R (2009) Axon tracking in serial block-face scanning electron microscopy. *Med Image Anal* **13**: 180-188
- Kanaya K, Okayama S (1972) Penetration and Energy-Loss Theory of Electrons in Solid Targets. *J Phys D Appl Phys* **5**: 43-58
- Kasai H, Matsuzaki M, Noguchi J, Yasumatsu N, Nakahara H (2003) Structure-stability-function relationships of dendritic spines. *Trends Neurosci* **26**: 360-368
- Knott G, Marchman H, Wall D, Lich B (2008) Serial section scanning electron microscopy of adult brain tissue using focused ion beam milling. *J Neurosci* **28**: 2959-2964
- Knott GW, Holtmaat A, Wilbrecht L, Welker E, Svoboda K (2006) Spine growth precedes synapse formation in the adult neocortex in vivo. *Nat Neurosci* **9**: 1117-1124

- Koch C, Zador A (1993) The Function of Dendritic Spines - Devices Subserving Biochemical Rather Than Electrical Compartmentalization. *Journal of Neuroscience* **13**: 413-422
- Koester HJ, Sakmann B (1998) Calcium dynamics in single spines during coincident pre- and postsynaptic activity depend on relative timing of back-propagating action potentials and subthreshold excitatory postsynaptic potentials. *Proc Natl Acad Sci U S A* **95**: 9596-9601
- Kondo S, Okabe S (2011) [Molecular mechanism underlying the formation and maintenance of excitatory synapses]. *Brain and nerve = Shinkei kenkyu no shinpo* **63**: 51-58
- Konur S, Ghosh A (2005) Calcium signaling and the control of dendritic development. *Neuron* **46**: 401-405
- Konur S, Rabinowitz D, Fenstermaker VL, Yuste R (2003) Systematic regulation of spine sizes and densities in pyramidal neurons. *J Neurobiol* **56**: 95-112
- Korkotian E, Segal M (1999) Release of calcium from stores alters the morphology of dendritic spines in cultured hippocampal neurons. *Proc Natl Acad Sci U S A* **96**: 12068-12072
- Kovalchuk Y, Eilers J, Lisman J, Konnerth A (2000) NMDA receptor-mediated subthreshold Ca(2+) signals in spines of hippocampal neurons. *J Neurosci* **20**: 1791-1799
- Lang S, Dercksen VJ, Sakmann B, Oberlaender M (2011a) Simulation of signal flow in 3D reconstructions of an anatomically realistic neural network in rat vibrissal cortex. *Neural networks : the official journal of the International Neural Network Society* **24**: 998-1011
- Lang S, Drouvelis P, Tafaj E, Bastian P, Sakmann B (2011b) Fast extraction of neuron morphologies from large-scale SBFSEM image stacks. *J Comput Neurosci* **31**: 533-545
- Larkman AU (1991) Dendritic morphology of pyramidal neurones of the visual cortex of the rat: III. Spine distributions. *J Comp Neurol* **306**: 332-343
- Lee RE (1992) *Scanning Electron Microscopy and X-Ray Microanalysis*: Prentice Hall.
- Leighton SB (1981) SEM images of block faces, cut by a miniature microtome within the SEM - a technical note. *Scan Electron Microsc* **Pt 2**: 73-76
- Lewis PR, Knight DP (1992) *Cytochemical Staining Methods for Electron Microscopy*, Amsterdam: Elsevier Science Publishers B.V.
- Lichtman J, Heyworth K. (2010) ATLUM Project. <http://cbs.fas.harvard.edu/science/connectome-project/atlum>.
- Lu J, Fiala JC, Lichtman JW (2009) Semi-automated reconstruction of neural processes from large numbers of fluorescence images. *PLoS One* **4**: e5655

- Macke JH, Maack N, Gupta R, Denk W, Scholkopf B, Borst A (2008) Contour-propagation algorithms for semi-automated reconstruction of neural processes. *J Neurosci Methods* **167**: 349-357
- Majewska A, Brown E, Ross J, Yuste R (2000a) Mechanisms of calcium decay kinetics in hippocampal spines: Role of spine calcium pumps and calcium diffusion through the spine neck in biochemical compartmentalization. *Journal of Neuroscience* **20**: 1722-1734
- Majewska A, Tashiro A, Yuste R (2000b) Regulation of spine calcium dynamics by rapid spine motility. *Journal of Neuroscience* **20**: 8262-8268
- Markram H (2006) The blue brain project. *Nat Rev Neurosci* **7**: 153-160
- Matsuzaki M, Honkura N, Ellis-Davies GC, Kasai H (2004) Structural basis of long-term potentiation in single dendritic spines. *Nature* **429**: 761-766
- Meyer S (1895) Die subcutane Methylenblauinjection, ein Mittel zur Darstellung der Elemente des Central-nervensystems Säugethieren. *Arch Mikrosk Anat* **46**: 282-290
- Meyer S (1896) Ueber eine Verbindungsweise der Neurone. Nebst Mitteilungen über die Technik und die Erfolge der Methode der subcutanen Methylenblauinjection. *Arch Mikrosk Anat* **47**: 734-748
- Meyer S (1897) Ueber die Funktion der Protoplasmafortsätze der Nervenzellen. *Bericht Math -Phys Cl Königl Sächs Gessells Wiss Leipzig* **49**: 475-495
- Monti A (1895a) Sur l'anatomie pathologique des éléments nerveux dans les processus provenant d'embolisme cérébral.- Considérations sur la signification physiologique des prolongements protoplasmiques des cellules nerveuses. *Arch ital Biol* **24**: 20-33
- Monti A (1895b) Sur les altérations du système nerveux dans l'inanition. . *Arch ital Biol* **24**: 347-360
- Naegerl UV, Willig KI, Hein B, Hell SW, Bonhoeffer T (2008) Live-cell imaging of dendritic spines by STED microscopy. *Proc Natl Acad Sci U S A* **105**: 18982-18987
- Nimchinsky EA, Sabatini BL, Svoboda K (2002) Structure and function of dendritic spines. *Annu Rev Physiol* **64**: 313-353
- Nusser Z, Lujan R, Laube G, Roberts JDB, Molnar E, Somogyi P (1998) Cell type and pathway dependence of synaptic AMPA receptor number and variability in the hippocampus. *Neuron* **21**: 545-559
- O'Brien J, Unwin N (2006) Organization of spines on the dendrites of Purkinje cells. *Proc Natl Acad Sci U S A* **103**: 1575-1580

- Oberlaender M, Dercksen VJ, Egger R, Gensel M, Sakmann B, Hege HC (2009) Automated three-dimensional detection and counting of neuron somata. *J Neurosci Methods* **180**: 147-160
- Oertner TG, Matus A (2005) Calcium regulation of actin dynamics in dendritic spines. *Cell Calcium* **37**: 477-482
- Ogura K, Yamada M, Hirahara O, Mita M, Erdman N, Nielsen C (2010) Gigantic Montages with a Fully Automated FE-SEM (Serial Sections of a Mouse Brain Tissue). *Microscopy and Microanalysis* **16**: 52-53
- Okabe S (2007) Molecular anatomy of the postsynaptic density. *Mol Cell Neurosci* **34**: 503-518
- Palay SL (1956) Synapses in the central nervous system. *J Biophys Biochem Cytol* **2**: 193-202
- Passingham RE, Stephan KE, Kotter R (2002) The anatomical basis of functional localization in the cortex. *Nat Rev Neurosci* **3**: 606-616
- Peachey LD (1958) Thin sections. I. A study of section thickness and physical distortion produced during microtomy. *J Biophys Biochem Cytol* **4**: 233-242
- Pelvig DP, Pakkenberg H, Stark AK, Pakkenberg B (2008) Neocortical glial cell numbers in human brains. *Neurobiol Aging* **29**: 1754-1762
- Peterfreund N (1998) Robust tracking with spatiovelocity snakes: Kalman filtering approach. *Sixth International Conference on Computer Vision*: 433-439
- Peterfreund N (1999) Robust tracking of position and velocity with Kalman snakes. *IEEE T Pattern Anal* **21**: 564-569
- Peters A (1987) Synaptic specificity in the cerebral cortex. In *Synaptic Function*, pp 373-397. New York: John Wiley
- Peters A, Kaiserman-Abramof IR (1969) The small pyramidal neuron of the rat cerebral cortex. The synapses upon dendritic spines. *Zeitschrift fur Zellforschung und mikroskopische Anatomie* **100**: 487-506
- Petersen CC (2007) The functional organization of the barrel cortex. *Neuron* **56**: 339-355
- Pinault D (1996) A novel single-cell staining procedure performed in vivo under electrophysiological control: morpho-functional features of juxtacellularly labeled thalamic cells and other central neurons with biocytin or Neurobiotin. *J Neurosci Methods* **65**: 113-136
- Rall W (1964) *Theoretical significance of dendritic trees for neuronal input-output relations*, Stanford: Stanford University Press.

Rall W (1974) *Dendritic spines, synaptic potency and neuronal plasticity*, Vol. Brain Inf. Serv. Rpt. no. 3, Los Angeles, CA: UCLA, Los Angeles, CA.

Rall W, Rinzel J (1971a) Dendritic spine function and synaptic attenuation calculations. *Progr Abstr Soc Neurosci First Annu Mtg* **1**

Rall W, Rinzel J (1971b) Dendritic spines and synaptic potency explored theoretically. *Proc IUPS (XXV Int Congr)* **IX**

Retzius G (1891) Ueber den Bau der Oberflächenschicht der Grosshirnrinde beim Menschen und bei den Säugethieren. *Biologiska Föreningens Förhandlingar* **3**: 90–102

Reynolds ES (1963) The use of lead citrate at high pH as an electron-opaque stain in electron microscopy. *J Cell Biol* **17**: 208-212

Rodriguez A, Ehlenberger DB, Dickstein DL, Hof PR, Wearne SL (2008) Automated three-dimensional detection and shape classification of dendritic spines from fluorescence microscopy images. *PLoS One* **3**: e1997

Roelandse M, Welman A, Wagner U, Hagmann J, Matus A (2003) Focal motility determines the geometry of dendritic spines. *Neuroscience* **121**: 39-49

Rollenhagen A, Satzler K, Rodriguez EP, Jonas P, Frotscher M, Lubke JHR (2007) Structural determinants of transmission at large hippocampal mossy fiber Synapses. *Journal of Neuroscience* **27**: 10434-10444

Rostaing P, Real E, Siksou L, Lechaire JP, Boudier T, Boeckers TM, Gertler F, Gundelfinger ED, Triller A, Marty S (2006) Analysis of synaptic ultrastructure without fixative using high-pressure freezing and tomography. *Eur J Neurosci* **24**: 3463-3474

Roth G, Dicke U (2005) Evolution of the brain and intelligence. *Trends Cogn Sci* **9**: 250-257

Rushworth MF, Noonan MP, Boorman ED, Walton ME, Behrens TE (2011) Frontal cortex and reward-guided learning and decision-making. *Neuron* **70**: 1054-1069

Saetzler K, McCanny P, Rodriguez EP, Horstmann H, Bruno RM, Denk W (2009) A fuzzy algorithm to trace stained neurons in serial block-face scanning electron microscopy image series. *Proceedings of the 2009 13th International Machine Vision and Image Processing Conference IMVIP 2009*: 162-167

Saetzler K, Sohl LF, Bollmann JH, Borst JG, Frotscher M, Sakmann B, Lubke JH (2002) Three-dimensional reconstruction of a calyx of Held and its postsynaptic principal neuron in the medial nucleus of the trapezoid body. *J Neurosci* **22**: 10567-10579

Schaffer K (1892) Beitrag zur Histologie der Ammonshornformation. *Arch mikrosk Anat* **39**: 611-632

- Schikorski T, Stevens CF (1999) Quantitative fine-structural analysis of olfactory cortical synapses. *Proc Natl Acad Sci U S A* **96**: 4107-4112
- Schikorski T, Stevens CF (2001) Morphological correlates of functionally defined synaptic vesicle populations. *Nat Neurosci* **4**: 391-395
- Schuz A, Palm G (1989) Density of neurons and synapses in the cerebral cortex of the mouse. *J Comp Neurol* **286**: 442-455
- Segal M (1995) Imaging of calcium variations in living dendritic spines of cultured rat hippocampal neurons. *The Journal of physiology* **486 (Pt 2)**: 283-295
- Segal M (2005) Dendritic spines and long-term plasticity. *Nat Rev Neurosci* **6**: 277-284
- Seligman AM, Karnovsky MJ, Wasserkrug HL, Hanker JS (1968) Nondroplet ultrastructural demonstration of cytochrome oxidase activity with a polymerizing osmiophilic reagent, diaminobenzidine (DAB). *J Cell Biol* **38**: 1-14
- Seligman AM, Wasserkrug HL, Hanker JS (1966) A new staining method (OTO) for enhancing contrast of lipid-containing membranes and droplets in osmium tetroxide-fixed tissue with osmiophilic thiocarbonylhydrazide(TCH). *J Cell Biol* **30**: 424-432
- Sheng M, Hoogenraad CC (2007) The postsynaptic architecture of excitatory synapses: a more quantitative view. *Annual review of biochemistry* **76**: 823-847
- Soille P (1999) *Morphological image analysis : principles and applications*, Berlin: Springer.
- Soper DS. (2012) p-Value Calculator for a Student t-Test (Online Software), <http://www.danielsoper.com/statcalc3/calc.aspx?id=8>.
- Spacek J, Harris KM (1998) Three-dimensional organization of cell adhesion junctions at synapses and dendritic spines in area CA1 of the rat hippocampus. *J Comp Neurol* **393**: 58-68
- Spacek J, Hartmann M (1983) 3-Dimensional Analysis of Dendritic Spines .1. Quantitative Observations Related to Dendritic Spine and Synaptic Morphology in Cerebral and Cerebellar Cortices. *Anat Embryol* **167**: 289-310
- Svoboda K, Denk W, Kleinfeld D, Tank DW (1997) In vivo dendritic calcium dynamics in neocortical pyramidal neurons. *Nature* **385**: 161-165
- Svoboda K, Tank DW, Denk W (1996) Direct measurement of coupling between dendritic spines and shafts. *Science* **272**: 716-719
- Trachtenberg JT, Chen BE, Knott GW, Feng G, Sanes JR, Welker E, Svoboda K (2002) Long-term in vivo imaging of experience-dependent synaptic plasticity in adult cortex. *Nature* **420**: 788-794

Vazquez L, Sapiro G, Randall G (1998) Segmenting neurons in electronic microscopy via geometric tracing. *1998 International Conference on Image Processing - Proceedings* **3**: 814-818

von Kölliker A (1896) *Handbuch der Gewebelehre des Menschen*, Vol. 2, sixth edn. Leipzig: Engelmann.

Weaker FJ, Herbert DC (2009) Netter's Essential Histology by William K. Ovalle and Patrick C. Nahirney. *Clinical Anatomy* **22**: 398-398

Wittke JH. (2008), <http://www4.nau.edu/microanalysis/Microprobe-SEM/Instrumentation.html>.

Woolsey TA, Van der Loos H (1970) The structural organization of layer IV in the somatosensory region (SI) of mouse cerebral cortex. The description of a cortical field composed of discrete cytoarchitectonic units. *Brain Res* **17**: 205-242

Yuste R, Bonhoeffer T (2001) Morphological changes in dendritic spines associated with long-term synaptic plasticity. *Annual review of neuroscience* **24**: 1071-1089

Yuste R, Bonhoeffer T (2004) Genesis of dendritic spines: insights from ultrastructural and imaging studies. *Nat Rev Neurosci* **5**: 24-34

Yuste R, Denk W (1995) Dendritic spines as basic functional units of neuronal integration. *Nature* **375**: 682-684

Yuste R, Majewska A, Cash SS, Denk W (1999) Mechanisms of calcium influx into hippocampal spines: heterogeneity among spines, coincidence detection by NMDA receptors, and optical quantal analysis. *J Neurosci* **19**: 1976-1987

Yuste R, Majewska A, Holthoff K (2000) From form to function: calcium compartmentalization in dendritic spines. *Nat Neurosci* **3**: 653-659

Zankel A, Kraus B, Poelt P, Schaffer M, Ingolic E (2009) Ultramicrotomy in the ESEM, a versatile method for materials and life sciences. *J Microsc* **233**: 140-148

Acknowledgements

First of all I want to thank my supervisors Prof. Bert Sakmann and Prof. Axel Borst: Bert Sakmann, for giving me the opportunity and the financial support to work on an interesting and diversified research project, to which I could apply myself very much. Axel Borst for harboring me in his department and for letting me participate on numerous internal activities. Many thanks go out to the whole department, especially former and actual P5 residents, for providing a great atmosphere. I also thank Mark Huebener for being a member of my thesis committee.

I want to thank my collaborators in Heidelberg: Stefan Lang and especially Panos (Panoulis) Drouvelis with whom I intensively worked to improve and expand the NeuroStruct toolbox and had the longest Skype chats I can remember.

I would particularly like to thank Christoph Kapfer for technical help and discussion on SBFSEM, and on his feedback and criticism on this thesis. Many thanks go to the steady computational help on Linux and Matlab provided by Hubert Eichner, Armin Bahl and Elisabeth Hopp. I further appreciate the help of Sigrid Richter for her support with buffers and DAB stainings, and the Histolab crew Marianne Braun, Romina Kutlesa and Ursula Weber for their help and discussion on stainings. Big thanks go out to everyone in the MPI for Neurobiology, especially to all my dear PhD colleagues, for creating a great atmosphere and making the institute a very nice place to work at!

Apart from the institute, I want to thank Christiaan deKock for always finding a sympathetic ear for my questions and Lauren Corona and Jonathan Mackinnon for pimping my English.

Last but not least I want to thank my parents Ulrike and Rudi for supporting me in everything I ever wanted to do and, of course, my wife Verena Schilling-Kurz for her constant support, love and encouragement.... I could not have done this without you!
Hatebreed!

Curriculum vitae

Thorben Andreas Kurz

Date of Birth: December 4th, 1977
Place of Birth: Bonn-Bad Godesberg (Germany)

Employment History

1/2008 – 9/2012 Max-Planck Institute for Neurobiology (Martinsried),
PhD Student
(Focus: Neurobiology in Mouse and Rat, Electron Microscopy,
Image processing, Histology, Immunohistochemistry, Patch-
Clamp)

05/2005 – 12/2007 Max-Planck Institute for Medical Research (Heidelberg)
Research Assistant
(Focus: Reconstruction of neurons in light microscopy (Rat))

07/2002 – 04/2005 Zentrum für Molekulare Biologie Heidelberg (ZMBH)
Undergraduate Research Assistant
(Focus: Chaperones in *E.coli*, Genetics and Protein
Biochemistry)

Education

01/2008 – 9/2012 PhD Thesis with Prof. Dr. Bert Sakmann at the Ludwig
Maximilian University in Munich

Thesis: „Development of Techniques for Single Dendritic Spine
Analysis: Spinomics“

10/1999 – 11/2006 Studies of Biology (Major: Molecular Biology, Minors: Cell
Biology and Biochemistry/Biophysics) at the Ruprecht Karls
University Heidelberg (Degree: Diplom Biologe)

Diploma thesis in the Junior Research Group of Dr. Elke
Deuerling: „Characterization of the Metacaspase MCA1, a
potential new Prion in Yeast“

1998 Ottheinrich Gymnasium Wiesloch (Abitur)

Supervision / Honorary Position

10/2009 – 12/2010	Elected for PhD Representative
01/2009 – 11/2009	Supervision of diploma student
02/2005	Supervision of practical course “Protein, Lipid and Signal Molecules”
WS 2000/1 + WS 2001/2	Supervision of practical course “Morphologisch-anatomisches Grundpraktikum A – Teil Zoologie”

Advanced training

04/2012	„Intercultural Communication: Key Problem-solving and Leadership Skills for the International Workplace” with Alexia Petersen
01/2010	Soft skill course “Scientific Writing” with Ruth Willmott.
08/2009	Soft skill course „Presenting Professionally” with Andrea Roos.
12/2007	“Versuchstierkundliche Grundlagen und Tierexperimentelle Methoden” after GV-SOLAS & FELASA.

Publications

Kurz TA*, Drouvelis P*, Lang S, Sakmann B (2012) **Spinomics: quantitative characterization of single dendritic spine morphologies obtained from SBFSEM** (*in Preparation*)

Kurz TA, Sakmann B (2012) **Development of a staining protocol for the extraction of multiple dendritic spine morphologies at nanoscopic resolution from biocytin-filled neurons using SBFSEM** (*in Preparation*)

Drouvelis P*, Kurz TA*, Lang S (2012) **NeuroStruct: A toolkit for the precise and reliable large-scale reconstruction of dendritic spines from biocytin-filled neurons from SBFSEM** (Under Review). *Med Imag Anal*

Vorderwulbecke S, Kramer G, Merz F, Kurz TA, Rauch T, Zachmann-Brand B, Bukau B, Deuerling E (2005) **Low temperature of GroEL/ES overproduction permits growth of Escherichia coli cells lacking trigger factor DnaK**. *FEBS letters* 579: 181-187

Kramer G, Rutkowska A, Wegrzyn RD, Patzelt H, Kurz TA, Merz F, Rauch T, Vorderwulbecke S, Deuerling E, Bukau B (2004b) **Functional dissection of Escherichia coli trigger factor: unraveling the function of individual domains**. *J Bacteriol* 186: 3777-3784

Kramer G, Patzelt H, Rauch T, Kurz TA, Vorderwulbecke S, Bukau B, Deuerling E (2004a) **Trigger factor peptidyl-prolyl cis/trans isomerase activity is not essential for the folding of cytosolic proteins in Escherichia coli**. *J Biol Chem* 279: 14165-14170

Versicherung

Ehrenwörtliche Versicherung

Ich versichere hiermit ehrenwörtlich, dass die vorgelegte Dissertation von mir selbständig und ohne unerlaubte Hilfe angefertigt ist.

München, den _____

Thorben Kurz

Erklärung

Hiermit erkläre ich, dass die Dissertation nicht ganz oder in wesentlichen Teilen einer anderen Prüfungskommission vorgelegt worden ist und dass ich mich anderweitig einer Doktorprüfung ohne Erfolg nicht unterzogen habe.

München, den _____

Thorben Kurz